Title
Investigating Silicon-Based Photoresists with Coherent Anti-Stokes Raman Scattering and X-ray Micro-spectroscopy

Author
Caster, Allison G.

Publication Date
2010

Peer reviewed|Thesis/dissertation

Investigating Silicon-Based Photoresists with Coherent Anti-Stokes Raman Scattering and X-ray Micro-spectroscopy

by

Allison G. Caster

A dissertation submitted in partial satisfaction of the requirements for the degree of

Doctor of Philosophy

in

Chemistry

in the

Graduate Division

of the

University of California, Berkeley

Committee in charge:

Professor Stephen R. Leone, Chair

Professor Richard Mathies

Professor Luke P. Lee

Spring 2010

Abstract

Investigating Silicon-Based Photoresists with
Coherent Anti-Stokes Raman Scattering and X-ray Micro-spectroscopy

by

Allison G. Caster

Doctor of Philosophy in Chemistry

University of California, Berkeley

Professor Stephen R. Leone, Chair

Photoresist lithography is a critical step in producing components for high-density data storage and high-speed information processing, as well as in the fabrication of many novel micro and nanoscale devices. With potential applications in next generation nanolithography, the chemistry of a high resolution photoresist material, hydrogen silsesquioxane (HSQ), is studied with two different state-of-the-art, chemically selective microscope systems. Broadband coherent anti-Stokes Raman scattering (CARS) micro-spectroscopy and scanning transmission X-ray microscopy (STXM) reveal the rate of the photoinduced HSQ cross-linking, providing insight into the reaction order, possible mechanisms and species involved in the reactions.

Near infrared (NIR) multiphoton absorption polymerization (MAP) is a relatively new technique for producing sub-diffraction limited structures in photoresists, and in this work it is utilized in HSQ for the first time. By monitoring changes in the characteristic Raman active modes over time with ~500 ms time resolution, broadband CARS micro-spectroscopy provides real-time, *in situ* measurements of the reaction rate as the HSQ thin films transform to a glass-like network (cross-linked) structure under the focused, pulsed NIR irradiation. The effect of laser power and temporal dispersion (chirp) on the cross-linking rate are studied in detail, revealing that the process is highly non-linear in the peak power of the laser pulses, requiring ~6 photons (on average) to induce each cross-linking event at high laser power, which opens the possibility for high resolution MAP lithography of HSQ. Reducing the peak power of the laser pulses, by reducing average laser power or increasing the chirp, allows fine control of the HSQ cross-linking rate and effective halting of the cross-linking reaction when desired, such that broadband CARS spectra can also be obtained without altering the material.

Direct-write X-ray lithography of HSQ and subsequent high resolution STXM imaging of line patterns reveals a dose and thickness dependent spread in the cross-linking reaction of greater than 70 nm from the exposed regions for 300 nm to 500 nm thick HSQ films. This spread leads to proximity effects such as area dependent exposure sensitivity. Possible mechanisms responsible for the reaction spread are presented in the context of previously reported results. X-ray lithography and imaging is also used to assess the X-ray induced cross-linking rate, and similarities are observed between NIR MAP and X-ray induced network formation of HSQ.

This dissertation is dedicated to my parents –
who always encouraged me to ask "Why?"

Contents

List of Figures

List of Tables

Acknowledgments

The journey to this point in my academic career has been both challenging and fulfilling, but I never could have made it without the amazing level of support and inspiration from many wise and experienced people along the way. Although there are too many to mention here, I want to specifically thank those who, without a doubt, directly and profoundly impacted my academic and personal success.

I came into Berkeley with a passion for science but no real grasp of how to harness that passion for productive purposes. The work in this dissertation was made possible by the consistent advice, constructive criticism, moral and financial support of my advisor, Steve Leone. His thorough and thoughtful attention to detail, drive for excellence and deep concern for the success of those under his guidance never ceases to amaze me, and I am sincerely grateful for the privilege of working with him and learning from him over these past 6 years.

I have been honored to work with so many amazing and talented people that Steve has brought into his research group. Sang-Hyun Lim designed the CARS microscope, invented and developed the DQSI and FTSI CARS, and also taught me an immense amount about physics, chemistry, mathematics, dedication and how to strive for perfection in an experiment, and I definitely grew as a scientist by working with him. I was also privileged to work in the CARS lab with Olivier Nicolet, who first sparked my interest in photoresists. For many of the ideas for the CARS and STXM experiments presented in this work, as well as help with data acquisition and interpretation, I owe a huge thanks to Adam Schwartzberg and Stefan Kowarik, both of whom provided so much support and guidance, enlightening discussions and friendship. Thanks also to Daniel Strasser for spending so many hours tweaking LabView programs and brainstorming new physics to try, Ben Doughty for his patience teaching me how to use Matlab and LabView for modeling and analysis, and my lab-mate Andy Caughey for his insight about data interpretation and cool experiments to try, even if we didn't get time to do most of the ideas he proposed! For enlightening discussions, friendship and help with experiments, thanks also to Mark Abel and Amy Cordones. In addition to those listed above, thanks to all the Leone group members who helped move our labs from LBNL to campus and reconstruct everything once we got there, including Christine Koh, Willem Boutu, Lynelle Takahashi, and Jia Zhou. Terefe Habteyes, Yohannes Abate, and Thomas Pfeiffer also provided vital experimental support and ideas along the way.

Mary Gilles taught me much of what I know about photoresists and HSQ, and also provided some of the X-ray beam time and sample substrates that made the STXM work possible, so I am very grateful for her expertise and support. Alexei Tivanski worked with Mary on the initial HSQ STXM experiments, gave helpful ideas about the experimental design, and provided crucial insight for interpreting the STXM results. Also, thanks to A.L. David Kilcoyne of beamline 5.3.2 at the Advanced Light Source for many hours of support in designing the STXM experiments and working out many details of the experiment with me. Thanks for discussion of HSQ lithography and mechanisms to Deirdre L. Olynick, Monika Fleischer, Adam Leontowich, Adam P. Hitchcock, and T. Don Tilley. Thanks to Stefan Pastine of the Frechet group for discussion of mechanisms and chemicals for inhibitor experiments, and to Chris J. Hahn for SEM measurements. For additional Raman measurements, thanks to P. Jim Schuck, and thanks to Farhad Salmassi for thin film profilometry measurements.

For first sparking my interest in research, encouraging me to pursue physical chemistry, and opening my eyes to so many academic and scientific opportunities, I must thank my

undergraduate research advisor Mary T. Berry; she also spent a great deal of thoughtful time in one-on-one discussions with me, editing my very first scientific posters, graduate school and fellowship applications, and undergraduate honors thesis. I will always feel a special gratitude to all my undergraduate science professors at the University of South Dakota, especially P. Stanley May, who taught me so much about critical thinking and what a physical chemistry lab report ought to look like, Tina Keller, for introducing me to the awe-inspiring fields of modern physics and special relativity, Miles Koppang and Andy Sykes for their time and energy in teaching me the fundamentals of chemistry. Susan Hackemer of the Honors Program at USD was an invaluable resource in my academic success, especially in preparing for graduate school and applying for the National Science Foundation Graduate Research Fellowship.

From the time I was very young, I had a penchant for questioning everything and wanting to know how everything worked at the very most basic level, so I must thank my parents, Joy and Harold Parry, for encouraging and supporting this (sometimes frustrating) behavior. I have only been able to achieve any of this because of their love, patience, and insistence that I could do anything I set my mind to, and so it is to them that I dedicate this thesis. I especially want to thank them for letting me follow whatever dreams I was inspired by in the moment, to form my own beliefs and ideas independent of their own, and their willingness to debate every topic with me (even if it did occasionally get me sent to my room). I must also give credit to my sister and brother for putting up with my constant debating and ranting on whatever subject had infatuated me at the moment, and all the sciencey explanations I filled their heads with all these years, and for being an inspiration to me in trying to be the best person I can.

Also, for inspiring me to apply myself and always strive to live up to my maximum potential, I want to give a special thanks to Margaret and Bill Tretheway, who taught me so much about music – and life – from elementary through high school and beyond, and I am honored to call them my friends. Thank you to my long-time friend Mason Blake, for all the great discussions and encouragement, helping take care of my son (and husband) during these busy past few years, and for continuing to be such a great friend. For his love and support during the past 10 years, I want to thank my biological father Gary Tschetter, especially for his help with our challenging first years away from home in Vermillion, then with our move to California, and now on the next leg of our journey to Colorado. I am thankful to Erika (Foley) Cobar for the uplifting friendship, scientific discussions over sushi, and impromptu baby-sitting. Although we were often too busy to spend time together, she is a truly wonderful friend, and I will miss her after I leave California. I wish her much success in graduate school and beyond.

Most importantly, I want to thank my wonderful husband Jeff, who supported me through the often challenging years of undergraduate and graduate school. From the bottom of my heart I appreciate his strength and dedication, especially in being a "single parent" for these past few months as I worked on my dissertation. Without his ideas, suggestions, patience, encouragement, perspective, and willingness to shift all his plans to fit my often-changing work schedule, this dissertation would never have happened. To my dearest son: thank you for giving up so much of your time with mommy so that I could work on my "science project," and for giving me the great joy of your presence at each break. Your face becomes even sweeter to me when I have to go so many hours without seeing it! I am sure they will both be glad to have more of my time again now that this dissertation is complete. They continue to be my greatest source of inspiration and joy, and I hope they will be proud of the work they helped me to accomplish!

1 Introduction

The powerful handheld computers and medical devices that we rely on every day are based on integrated circuits with nanoscale features, made possible by the lithography of polymer photoresists. What's more, photoresists are now used to fabricate micro- and nanoscale components for a whole host of novel optical, electronic and mechanical devices, developed to address a vast variety of needs in materials, chemistry, physics and biomedical research and diagnostics. As the demand grows for smaller structures and faster, smaller, more reliable devices, so must the photoresist technology advance, requiring constant research into state-of-the-art resist materials, their photochemistry, exposure sources and photolithography techniques. For the next generation of components with sub-20 nm lithographic features, a promising class of silicon-based resists are based on the "building block" molecule hydrogen silsesquioxane (HSQ). Some of the smallest lithographic structures in any resist to date, down to 4.5 nm in width, have been produced in HSQ.[1-2]

The standard photoresist measurement tools, AFM and SEM, require additional processing steps after exposure prior to imaging of the photoresist patterns. Commonly used spectroscopic tools such as FTIR provide chemical selectivity without additional processing, but have insufficient temporal and spatial resolution to answer some of the pervasive questions about HSQ thin films, and so the conversion mechanisms applicable to micro and nano-patterning of HSQ are still not well understood. Therefore, broadband coherent anti-Stokes Raman scattering (CARS) microscopy and scanning transmission X-ray microscopy (STXM) are used here to provide a balance of high spatial resolution (~400 nm and 30 nm, respectively) and the necessary chemical selectivity to differentiate between the exposed versus unexposed HSQ structures, along with the sub-second temporal resolution to follow the chemistry in real-time. These techniques enable both chemically selective imaging of patterned resists and microspectroscopy of the photochemical conversion process, including a multiphoton exposure technique never before applied to HSQ. It is hoped that these results will provide direction for optimizing HSQ photolithography and designing new silicon-based photoresist materials with enhanced resolution and reliability.

1.1 The important role of photoresists

Photoresists are photosensitive materials that undergo a change in chemistry and solubility when exposed to light. The exposed or unexposed material is subsequently removed by a developer, and the patterns that remain on the underlying substrate undergo additional processing steps to fabricate functional structures and devices.[3] The typical resist processing steps are shown schematically in Figure 1.1. In positive tone resists, bond breaking and increased solubility occur in exposed regions, which are removed by a developer; conversely, in negative tone resists, the exposed regions become less soluble in the developer and instead the unexposed region is removed. After exposure, but prior to the development, the pattern is known as a latent pattern. Based on their chemistry, different resists are sensitive to different energy photons and/or particles, including electrons, protons and helium ions, and photons ranging from the X-ray and EUV to the visible.[3] Current chip manufacturing relies primarily on mask-based EUV lithography,[4] while direct-write electron beam (e-beam) resist technology typically

provides the state-of-the-art in small linewidth features in research and small-scale production environments for novel types of nanostructures.[2]

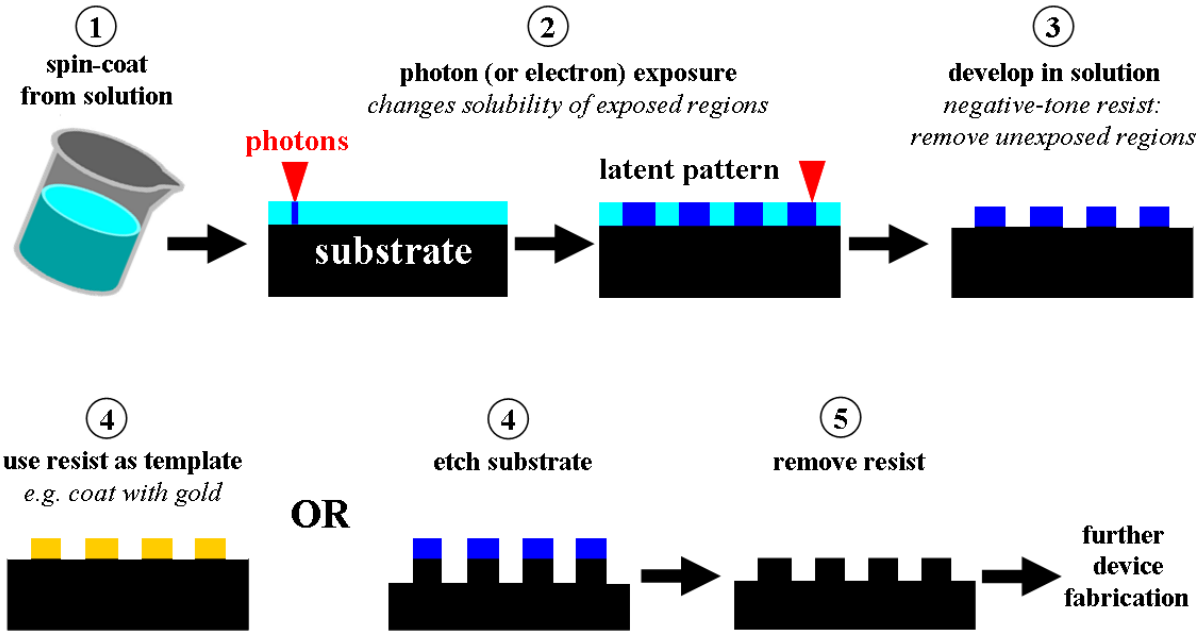

Figure 1.1 Side-view schematic of select resist processing steps for a negative-tone resist.

Discovered in 1826, photoresists were first developed for photography and printing,[3] but the lithography of modern photoresists has enabled the patterning of hundreds of millions of transistors on a single microchip, or integrated circuit.[4] Computers began as room-sized devices based on large vacuum tubes, then progressed to smaller machines based on transistors, and the advent of chip-based transistors on tiny integrated circuits was a crucial factor in making previously huge, expensive computers into the widespread, miniature devices we know today.[5] Growth in the semiconductor industry is driven by Moore's law, which initially projected that every 18 months, feature sizes in integrated circuits would decrease by a factor of $\sqrt{2}$, allowing twice the number of transistors or memory devices per unit area. Moore himself noted that, below ~180 nm feature sizes, this rate of growth could not continue indefinitely because of physical constraints.[4] However, line features in high-volume processing are now approaching ~22 nm in width (half-pitch).[4, 6-7] To improve device performance and reliability and expand the possibilities for the next generation of computing, even smaller sized features are required in the now multilayer integrated circuits, and this depends on improving the nanoscale lithography, primarily through the design of new photoresist materials and their exposure sources.[2, 7]

The chemistry of resists has become even more important as new applications are developed that require complex micro and nanoscale structures, such as optics for EUV[8-9] and X-rays,[10-14] nano-antennas for optical field enhancement,[15] UV waveguides[16], photonic crystal fibers,[17-18] microfluidics,[19-25] deep UV photodiodes,[26] organic solar cells,[27-28] and more. This rising demand for high performance electronics components and novel optical devices requires rapid, reliable fabrication of the structures contained within them. Polymer photoresists are desirable for their ease of application and use and for the variety of different materials and exposure techniques available.[3-4, 29] One silicon-based polymer resist that has been drawing a lot of recent interest is hydrogen silsesquioxane.

1.2 Hydrogen silsesquioxane (HSQ) resists

Hydrogen silsesquioxane (HSQ) is a cage-like molecule with the formula $H_8Si_8O_{12}$ (often written $HSiO_{3/2}$), a member of a class of compounds known collectively as polyhedral oligomeric silsesquioxanes (POSS),[30] shown in Figure 1.2(a). Also known as "spin-on glass", it was developed as an interlayer dielectric (ILD) film for multilevel integrated circuits,[31-33] where extremely thin HSQ films are applied from a volatile solution via spin coating, then cross-linked to an insoluble, glass-like SiO_2 network structure via heating,[34-36] as shown schematically in Figure 1.2(b). In 1998 it was discovered that HSQ is also a sensitive electron beam (e-beam) resist,[37] capable of producing nanoscale cross-linked, glass-like features.[38] Since then, the sensitivity of HSQ to a variety of exposure techniques has been demonstrated, including proton beam,[39] helium beam (He^+),[40] EUV, and X-ray exposure.[41-43]

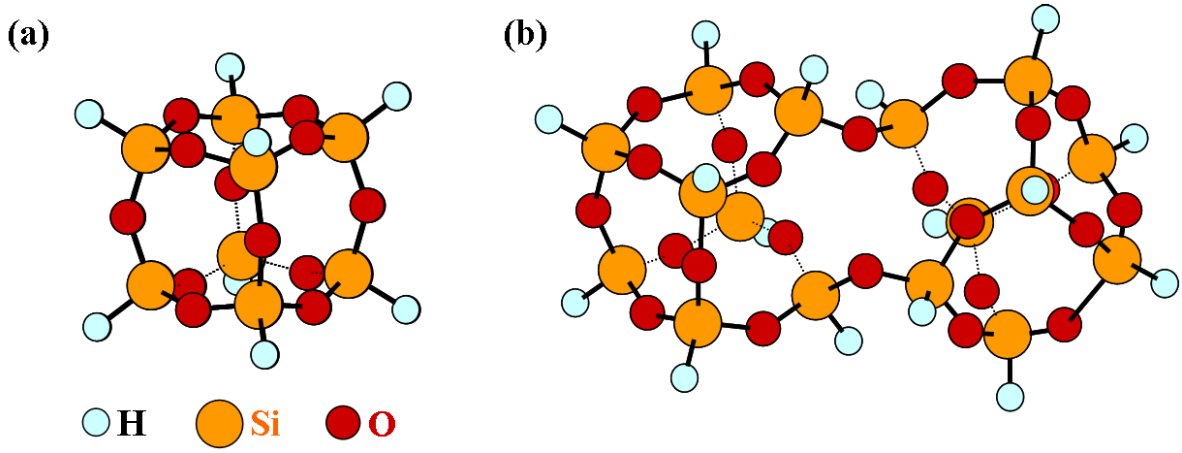

Figure 1.2 Schematic of HSQ (a) cage (monomer) and (b) possible partial network structure (oligomer) formed by cross-linking two monomer cages. In solution, the molecular structure is actually comprised of oligomers of various sizes.[2]

HSQ is a promising negative-tone resist for sub-20 nm electron beam (e-beam) and photolithography because of its small molecular size, low dielectric constant and mechanical stability,[2, 37] but a better understanding of the cross-linking chemistry is necessary to utilize HSQ and HSQ derivatives for commercial nanolithography applications. In research environments, e-beam lithography of HSQ is being used to produce high aspect-ratio, nanoscale features as small as 4.5 nm,[1] which are used for optical devices such as EUV diffraction gratings,[8-9] X-ray zone plates,[10-14] and nano-antennas,[15] as well as high-density line patterns for the next generation of integrated circuits and computer memory.[44-45] However, it is often necessary to vary the exposure dose and developer conditions in unpredictable ways to achieve precisely the desired feature size and contrast,[2, 46-47] and irreproducibility is caused by delay effects[48-49] and area dependent sensitivity.[8, 50-51] Therefore, much work has recently been done to determine the optimum parameters for achieving the smallest features in e-beam lithography of HSQ,[1, 46, 51-52] but unanswered questions remain.[2]

While e-beam lithography is an important patterning modality for HSQ, commercial integrated circuit manufacturing typically requires high-throughput optical lithography. Toward this goal, EUV interference lithography has been used in HSQ for dense line patterns down to 20 nm half-pitch,[53] and X-ray exposure behind a mask can create isolated features in HSQ down

to 11 nm wide in a 50 nm thick film.[54-55] Thus HSQ line widths surpass the resolution possible with conventional chemically amplified polymer photoresists,[44] but with insufficient sensitivity and reproducibility for high-throughput commercial applications. Therefore, new and improved HSQ derived and HSQ-like materials are currently being developed,[56] but progress could be hastened by understanding the fundamental chemistry that causes the current challenges with HSQ. There have been a variety of studies that aim to determine the thermally induced reaction mechanism of HSQ, mostly with FTIR spectroscopy,[34, 57-58] but more study is needed to fully characterize the photo-induced cross-linking mechanism applicable to the micro and nano-patterning of HSQ. A better understanding of the solid-state, nanoscale cross-linking chemistry is necessary to unlock the full potential of this material and its derivatives for the next generation of commercial applications, and this is where microspectroscopy techniques such as broadband coherent anti-stokes Raman scattering (CARS) and scanning transmission X-ray microscopy (STXM) can play a key role.

1.3 Multiphoton absorption polymerization

Multiphoton absorption polymerization (MAP) is another relatively new technique for producing fine patterns in polymer photoresists. Feature resolution in traditional photo-lithography is intrinsically diffraction limited (~λ/2), but relatively inexpensive pulsed visible and near IR lasers can be used to produce sub-diffraction limited sized features in materials that otherwise absorb only in the UV or EUV, as the probability for simultaneous multiphoton absorption is highest only within the very center of the focused beam profile. As with other non-linear optical processes, such as two-photon fluorescence or CARS, the probability for inducing the cross-linking reaction is greatly increased when the power density, or number of photons per unit time, is very high, as occurs during the very short pulses of ultrafast lasers. The power density during the "on" time of an ultrafast pulse is referred to as the peak power. The resolution enhancement in multiphoton processes is greater when more photons are required to initiate the process of interest (cross-linking, bond-breaking, ablation, signal generation, *etc.*), because the necessary peak power can only be found at smaller and smaller regions within the focal volume.[59] Through other creative manipulations of multiple laser beams, features down to λ/20 resolution have been produced with 800 nm exposure (i.e. 40 nm features).[60]

Another advantage of MAP is the capability to produce complex or layered three-dimensional structures in thicker films (>1 μm), because the nonlinear photoactivation process does not occur all along the beam path, but only in the region of highest power density within the focus. Thus, the beam can be scanned not only laterally but also throughout the depth of the sample to initiate cross-linking in very precise domains in x, y and z. Fascinating 3D structures have been produced by MAP in photoresists that would not be possible with single-photon excitation methods, from micromachines[61-62] to photonic crystal fiber arrays[17] to novel microfluidics[63-64] and other layered microstructures[65]. As the resolution of MAP is increased, it is conceivable that functional 3D nanostructures will also be fabricated in this way. In the experiments presented here, near-IR MAP of HSQ is demonstrated for the first time, along with an analysis of the cross-linking kinetics and the non-linear power dependence of the process under various conditions, studied in real time with broadband coherent anti-Stokes Raman scattering (CARS) spectroscopy.

1.4 Microspectroscopy of photoresists

High resolution, chemically selective imaging is a sought after tool in many fields, from biology to materials science, including mapping of latent (undeveloped) patterns in polymer photoresists for design and quality control purposes. In most studies of HSQ lithography, exposure is followed by development in solution and subsequent imaging with scanning electron microscopy (SEM), scanning tunneling microscopy (STM) or atomic force microscopy (AFM). These techniques can provide down to atomic spatial resolution, but little to no chemical information, and are only surface sensitive. For understanding the exposure-induced cross-linking process, one drawback to analyzing resists after development is that the chemical effects of exposure are coupled with the development chemistry, and the features produced are extremely sensitive to small changes in the development process.[47, 51, 66-67] In contrast, FTIR spectroscopy has been utilized to study chemical changes in undeveloped HSQ due to thermal curing or e-beam exposure,[34, 58] and FTIR microspectroscopy is used to image the spatial distribution of the cross-linking reaction and functional groups in latent e-beam patterns,[68] but is limited to ~10 μm spatial resolution at best. By comparison, broadband coherent anti-Stokes Raman scattering (CARS) microscopy and scanning transmission X-ray microscopy (STXM) provide higher spatial resolution (~400 nm and 30 nm, respectively), fast acquisition time (from tens of milliseconds to seconds) and very high chemical selectivity for microspectroscopy and imaging of latent resist patterns.

1.4.1 Coherent anti-Stokes Raman scattering microscopy

Raman scattering spectroscopy and microscopy is widely used in biological and physical sciences for sample identification and imaging, as it provides a "fingerprint" spectrum of the molecules in a sample based only on their intrinsic vibrational modes, without the need for any labeling or staining. Despite the low cross-section for Raman scattering of ~10^{-25} cm^2, it offers a powerful way to peer into many samples and organisms, and so many variations of Raman scattering have emerged over the years. One method for enhancing the signal strength, and hence the sensitivity, of Raman scattering is a nonlinear process called coherent anti-Stokes Raman scattering (CARS). Since its discovery in 1964,[69] CARS has been used to study a wide variety of samples and systems, from measurement of combustion temperatures[70] to tissues *in vivo*.[71-72] The first CARS microscope was demonstrated in 1982,[73] and in 1999 a focus on biological imaging using CARS microscopy began a new wave of discovery and innovation in CARS microscope development.[74]

The first CARS microscopes, and most in use today, utilize narrowband lasers to probe one single Raman-active vibrational mode at a time. Very sensitive and rapid images have been measured with narrowband CARS microscopy, including images of latent patterns in polymer photoresists.[75] However, a broader vibrational spectrum is needed to simultaneously quantify multiple materials within each region of the resist, especially for chemicals with very similar spectral features, such as cage versus cross-linked HSQ. To this end, it is possible to incorporate a broadband laser to acquire multiplex or broadband CARS spectra, explained in detail in section 2.1. The fast spectral acquisition of broadband CARS allows monitoring of changes in the spectrum as the rapid HSQ cross-linking reaction occurs. While the kinetics of solution phase reactions can be studied at a slower rate by dilution, such dilution is not possible for most solid-

state samples, such as polymer photoresist thin films, without totally altering the composition and chemistry of the films. Previous FTIR measurements of thermally cross-linked HSQ films were limited to 1-2 minute time resolution by sample heating and cooling times, but it was shown that most of the cross-linking occurs within the first minutes of heating.[58] On the other hand, real-time FTIR measurements of solid state kinetics in other, very thick (~25 μm to 5 mm) photoreactive polymers have been reported, which offer higher time resolution, on the order of ~20 ms,[76-78] but this technique has not been applied to the study of HSQ. Similar in concept to real-time FTIR, the sub-second time resolution of the broadband CARS method employed here provides detail about the early stages of the HSQ cross-linking in thin films as the process is monitored *in situ*.[79] Furthermore, the same pulsed near IR light source used for the CARS spectroscopy is also used here to induce multiphoton HSQ cross-linking. Due to the non-linearity of the process, control of the temporal and spectral profile of the laser pulses allows the cross-linking rate to be finely controlled, even to a level that it initiates (essentially) no cross-linking, while maintaining a strong CARS signal intensity.

1.4.2 Scanning transmission X-ray microscopy

While CARS can provide a great amount of chemical information on a relatively short time scale, the spatial resolution is limited to ~300-400 nm. To understand the behavior of photoresists for nanostructure fabrication, chemical information at much higher spatial resolution is required, a need fulfilled by scanning transmission X-ray microscopy (STXM). In STXM, X-rays are focused on a thin sample and the transmitted flux is measured as the sample is raster scanned perpendicular to the X-ray beam to create a pixel-by-pixel image. In routine state-of-the-art X-ray microscopy, the typical spatial resolution is ~30 nm, achieved by focusing the X-rays with a diffraction based Fresnel zone-plate with an outermost zone radius of 25 nm, as detailed in section 2.4. Zone plates with 12 and 15 nm outer zone radius have recently been fabricated for the next generation of improved resolution STXM instruments,[10-12] and interestingly, e-beam lithography of HSQ resists is used to fabricate these very zone plates.

When an X-ray of sufficient energy interacts with an atom, it can be absorbed by promoting a photoelectron from one of the inner core shells. The near edge X-ray absorption fine structure (NEXAFS) spectrum, explained in section 2.3, reveals the element-specific local electronic structure of a material. The high resolution STXM at beamline 5.3.2 of the Advanced Light Source (ALS) at Lawrence Berkeley National Lab was specifically designed for the study of polymeric materials through their carbon, nitrogen and oxygen 1*s* absorption edge NEXAFS spectra (core binding energies of approximately 280 eV, 410 eV and 543 eV, respectively), and several different positive and negative-tone photoresists have previously been imaged and studied at this STXM.[50, 80-81] An additional, undulator-based STXM at beamline 11.0.2 of the ALS extends the accessible energy range to 130 eV - 2000 eV, which encompasses the ~1850 eV K-edge absorption of silicon, also useful for the study of HSQ. Recently, the first STXM studies of HSQ thin films were performed on latent e-beam patterns at beamlines 5.3.2 and 11.0.2, revealing differences in the NEXAFS spectrum of the cage versus cross-linked HSQ, and a significant, unexpected spatial spread of the reaction beyond the e-beam exposure boundaries.[50] Reaction spread is also observed in this work after X-ray exposure, which is explored in detail in section 5.6.

Due to the high photon energies used, X-ray microscopy can induce sample damage. The STXM interface allows the user to balance signal levels with photodamage by minimizing the total radiation dose delivered during imaging and spectroscopy. HSQ is known to be sensitive to X-ray exposure, so significant optimization is required to acquire HSQ images and spectra in the STXM without inducing significant sample cross-linking. However, it is likewise possible to increase the X-ray flux through the sample in order to induce bond scission or cross-linking of polymers, a concept recently explored for direct-write patterning of positive tone polymer photoresists such as PMMA (polymethylmethacrylate) and PAN (polyacrylonitrile).[81-82] As reported in this work, this X-ray induced cross-linking can also be used to directly write patterns in the HSQ films.[83] The beam diameter (FWHM) at the focus is ≤50 nm and the position of the sample in the beam can be controlled with <10 nm of jitter, so fine patterns can be written directly by the X-ray beam by scanning the sample through the beam in a pre-defined pattern with a sufficient photon flux and per-point exposure time. Photolithography of HSQ is a sought-after tool for high-throughput resist processing, so a number of studies have investigated the limits and characteristics of EUV and X-ray lithography of HSQ, where blanket exposures through a mask are typically used.[41-43, 53-55, 84-85] Direct-write patterning with the STXM is slower than such blanket exposures, to be sure, but it enables characterization of the films immediately after patterning, minimizing the post-patterning delay (during which sample changes may occur)[2, 48-49] and eliminating the development step prior to analysis of the photochemistry. Thus, STXM is used to investigate in detail the X-ray induced cross-linking chemistry and reaction rate and to define the spatial extent of the reaction spread. These results provide insight into the photolithography mechanism, and hopefully provide some guidance on how new silicon-based photoresist materials might be altered for faster, more reliable nanolithography.

1.5 Outline: Optimizing microspectroscopy techniques to study HSQ chemistry

A detailed review of the theory and design of the novel, single-beam broadband CARS method is given in Chapter 2, with examples of (damage-free) polymer blend imaging to demonstrate the temporal and spatial resolution of the technique. This is followed by a brief overview of the theory of NEXAFS spectroscopy, the design of the (well-established) STXM microscope at beamline 5.3.2, and the optimization of the STXM framework for direct-write X-ray patterning of HSQ thin films. The discovery of near IR multiphoton HSQ cross-linking is presented in Chapter 3, followed by an analysis of the CARS and spontaneous Raman spectral intensities and lineshapes of HSQ thin films. In Chapter 4 broadband CARS is utilized to reveal the power-dependent cross-linking rate, and possible HSQ cross-linking mechanisms are discussed in detail, especially as they pertain to the multiphoton-induced cross-linking. In Chapter 5, cross-linked patterns are produced in HSQ thin films with the focused X-ray beam of the STXM. NEXAFS spectra and STXM images of the latent patterns, along with spectra of related POSS compounds, reveal details about X-ray cross-linking mechanism and reaction rates, analogous and complementary to the CARS results. Furthermore, a common reproducibility effect in HSQ is observed and explained by measuring the spatial extent of the spread in X-ray patterned features with 30 nm resolution. Several of the X-ray patterned films are developed and imaged with SEM to compare the feature characteristics before and after development.

Connections are drawn between the CARS and STXM HSQ results in Chapter 6 and discussed in the context of previously reported phenomena, along with preliminary results regarding cross-linking inhibitors and ideas for future research directions in studying the photochemistry of HSQ and improving its photolithography characteristics for current and new applications.

2 Experimental techniques: theory and design

2.1 Coherent anti-Stokes Raman scattering (CARS)

When light is scattered by a molecule, elastic (Rayleigh) scattering is the most probable, whereby the scattered light has the same frequency as the incident light. Following classical electrodynamics, the scattering is produced by the oscillating polarization (dipole) of the molecule induced by the incident electric field of the light:

$$\vec{P}_{Rayleigh}(t) \propto \underline{\underline{\alpha}} \left|\vec{E}\right| \cos \omega_0 t \,, \tag{2.1}$$

where $\vec{P}$ is the induced (transient) dipole oscillating with frequency ω_0, $\underline{\underline{\alpha}}$ is the polarizability (tensor) of the molecule and $\left|\vec{E}\right|$ is the amplitude of the incident electric field, also of frequency ω_0. In rare instances – about 1 in 10^7 scattering events – inelastic Raman scattering occurs, shifting the incoming frequency by the energy of the vibrational modes of the molecule:

$$\vec{P}_{Raman}(t) \propto \left|\vec{E}\right| Q_i^0 \frac{\delta \underline{\underline{\alpha}}}{\delta Q_i} [\cos(\omega_0 - \omega_i)t + \cos(\omega_0 + \omega_i)t], \tag{2.2}$$

where ω_i is the i^{th} vibrational frequency of the molecule with an amplitude of Q_i^0, and $\frac{\delta \underline{\underline{\alpha}}}{\delta Q}$ is the (first order) change in the polarizability with the vibrational motion along the molecular vibrational (normal) coordinate Q_i, which must be non-zero for Raman scattering to occur. Thus, depending on the initial vibrational state of the molecule, the frequency of the Raman scattered light can be lower (Stokes, ω_0- ω_i) or higher (anti-Stokes, ω_0+ω_i) than the incident light, as shown in Figure 2.1(a).

While infrared absorption only occurs when there is a change in the permanent dipole moment along the vibrational coordinate, Raman scattering requires that the polarizability changes with the vibrational motion. Therefore, some vibrational modes not accessible in IR spectroscopy can be observed with Raman, and vice versa. (Specifically, in molecules with a center of symmetry, vibrational modes can be either Raman or IR active, but not both.) When the light has a wavelength far longer (lower energy) than any electronic transitions in the atom, then the polarizability is independent of wavelength (although the scattered light intensity does vary as ω_0^4). Therefore, unlike IR absorption, Raman spectra can be obtained from a monochromatic source of almost any color in the visible to near IR portion of the electromagnetic spectrum, avoiding direct electronic excitation or IR absorption. Since the incident light is not in the IR, water is transparent and thus hydrated samples do not pose a problem as they do in IR spectroscopy. Also, if the polarization of the incoming light is not oriented parallel to one of the principal axes of the polarizabilty of the molecule, the scattered light will be depolarized; that is, it will have some portion polarized perpendicular to the incident field, $\vec{E}$. This will be discussed in more detail when depolarization Raman spectra of HSQ are presented in section 3.4.

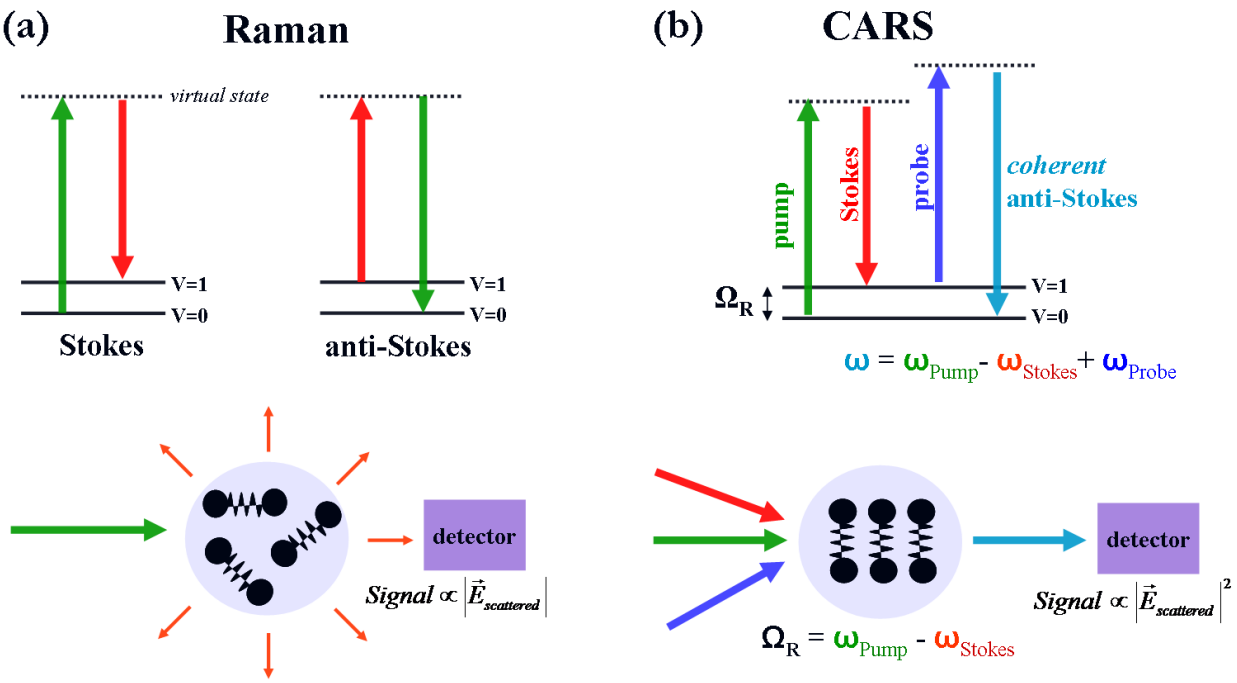

Figure 2.1 Schematic of (a) Raman and (b) CARS processes

Accounting for the quantized nature of molecular excited states, for spontaneous Raman the anti-Stokes to Stokes intensity ratio for a single vibrational mode is given by the thermal distribution of vibrational excitation according to:[86]

$$\frac{I_A}{I_S} = \left(\frac{\omega_0 + \omega_i}{\omega_0 - \omega_i}\right)^4 \exp\left(\frac{-\hbar\omega_i}{kT}\right) \tag{2.3}$$

where I_A and I_S are the anti-Stokes and Stokes scattered light intensity, respectively, $\hbar$ is the reduced Planck's constant, k the Boltzmann constant, and T the sample temperature. For room temperature samples, most of the molecules are thus in the ground vibrational state, so the Stokes Raman scattering intensity is always much larger than the anti-Stokes. In coherent anti-Stokes Raman scattering (CARS), the first vibrational level is "populated" by laser excitation, greatly increasing the probability for anti-Stokes scattering.

While Raman scattering involves single-photon excitation, CARS is a four-wave mixing process in which two intense laser fields, called the pump and Stokes fields, interact with the sample to induce coherent molecular vibrations, and a third probe field then scatters off of these vibrations to produce the coherent anti-Stokes Raman signal at a higher frequency, shown in Figure 2.1(b). This signal is strongly enhanced when the energy difference between the pump and Stokes fields matches the energy of an intrinsic molecular vibrational level. Due to the coherence of the scattered light, the signal is proportional to the square of the scattered field intensity, much stronger than in the spontaneous Raman scattering process. Also, the directionality of the CARS signal makes it more straightforward to collect all of the scattered light than in spontaneous Raman, which scatters with approximately 4π geometry. The CARS signal enhancement over spontaneous Raman can be up to ~10^5, but it depends strongly upon sample thickness, density, excitation and detection geometry, and whether a single vibrational mode (narrowband) or the entire spectrum (broadband) is excited. In spontaneous Raman

scattering, the Stokes signal is typically used for microscopy and sample identification because the anti-Stokes signal is significantly weaker. One big advantage of detecting the anti-Stokes term instead is the absence of overlap with the fluorescence, especially in samples with strong fluorescence under laser illumination.

The induced polarization due to higher order photon interactions (to third order) is:

$$\vec{P} = \chi^{(1)}\vec{E} + \chi^{(2)}\vec{E}^2 + \chi^{(3)}\vec{E}^3, \tag{2.4}$$

where $\chi^{(n)}$ is the n^{th} order susceptibility of the molecule, which is a tensor of rank $n+1$, and $\vec{E}$ is again the electric field of the incident light.[87] Thus, $\chi^{(1)} \equiv \underline{\underline{\alpha}}$, the polarizability of the molecule, which accounts for Rayleigh and spontaneous Raman scattering, $\chi^{(2)}$ is responsible for second-order processes such as second harmonic generation, and $\chi^{(3)}$ is a fourth-rank tensor called the third-order nonlinear susceptibility, responsible for the coherent anti-Stokes Raman scattering process. The total $\chi^{(3)}$ contains contributions from many other possible frequency combinations of the incident fields which do not correspond to CARS, such as third harmonic generation and other instantaneous electronic four-wave mixing processes. Since we are interested only in vibrational resonances leading to CARS signal, all the other third-order processes besides CARS will be defined as nonresonant (NR), giving:

$$\chi^{(3)}(\Omega) = \chi_R^{(3)}(\Omega) + \chi_{NR}^{(3)}(\Omega), \tag{2.5}$$

where $\chi_R^{(3)}(\Omega)$ is the resonant CARS part of the third-order nonlinear susceptibility, and $\chi_{NR}^{(3)}(\Omega)$ is the nonresonant part, which are given by:

$$\chi_R^{(3)}(\Omega) = \alpha_R \sum_R \frac{a_R}{(\Omega_R - \Omega) + i\Gamma_R} \tag{2.6}$$

and:

$$\chi_{NR}^{(3)}(\Omega) = \frac{\alpha_{NR}}{\Omega} \tag{2.7}$$

where α_R and α_{NR} are the amplitude coefficients for the resonant and NR susceptibilities, respectively, a_R, Ω_R and Γ_R are the intensity, energy and line width of vibrational mode R, respectively, and $\Omega = \omega - \omega_{\text{Pr}}$, where ω_{Pr} is the frequency of the probe field.[88-89] Thus, $\chi_{NR}^{(3)}(\Omega)$ is purely a real quantity, but $\chi_R^{(3)}(\Omega)$ contains real and imaginary parts, corresponding to the phase shift that occurs during forced, damped vibrations, as experienced here by the electric-field induced oscillating dipole.[90] Thus, vibrational excitations have Lorentzian natural lineshapes, and the imaginary part of this lineshape is what is detected in spontaneous Raman spectroscopy.[91] The signal detected at frequency ω is enhanced when the difference between the pump and Stokes fields is in resonance with a vibrational frequency of the molecule, as shown in Figure 2.1(b). That is, the signal is most enhanced when:

$$\Omega = \omega_S - \omega_P = \Omega_R \tag{2.8}$$

where ω_P and ω_S are the frequency of the pump and Stokes fields, respectively. Thus, when $\omega_P - \omega_s$ is tuned to a vibrational resonance, the total signal at frequency ω is a combination of both resonant anti-Stokes Raman scattering and NR four-wave mixing signals. The implications of the complex nature of $\chi_R^{(3)}(\Omega)$ on the CARS signal intensity and lineshape are further explored in section 2.2.1.

Typically, narrowband CARS utilizes one picosecond laser to supply the pump and probe beams at the same frequency and a second picosecond laser for the energy-shifted Stokes beam [Figure 2.1(b) and Figure 2.2(a)]. Single vibrational resonances can be probed one at a time by tuning the difference between the pump/probe and Stokes beams to match these vibrational frequencies. However, since the vibrational fingerprint region extends from about 800 to 1800 cm^{-1}, it is desirable to simultaneously acquire this full vibrational spectrum at each spatial location in a sample. To accomplish this, a broadband pump beam can be used to excite multiple vibrational modes simultaneously, while a narrow probe beam provides higher spectral resolution in the CARS spectrum [Figure 2.2(b)], and this is known as multiplex or broadband CARS, depending on the frequency range of the technique used. Multiple definitions have been proposed, but typically multiplex CARS refers to techniques with <1000 cm^{-1} of bandwidth, while broadband CARS applies when 1000-3000 cm^{-1} of bandwidth are accessible. There are, however, tradeoffs necessary to gain this spectral width. With narrowband CARS the signal sensitivity and signal acquisition rate can be much higher, but with broadband CARS the full Raman-equivalent spectrum is provided in a single pulse, and in microscopy the spatial locations of multiple species can therefore be obtained in a single image scan. Also, higher laser power is necessary to populate and measure all the vibrational modes for broadband CARS versus a single mode in narrowband CARS, increasing the risk of sample damage. For broadband CARS, the nonresonant signal due to $\chi_{NR}^{(3)}(\Omega)$ can even exceed the resonant CARS signal, as there are many different combinations of the three fields that contribute to the NR signal at each frequency. As such, significant signal manipulation is required to retrieve the smaller resonant signal and Raman-equivalent spectrum.

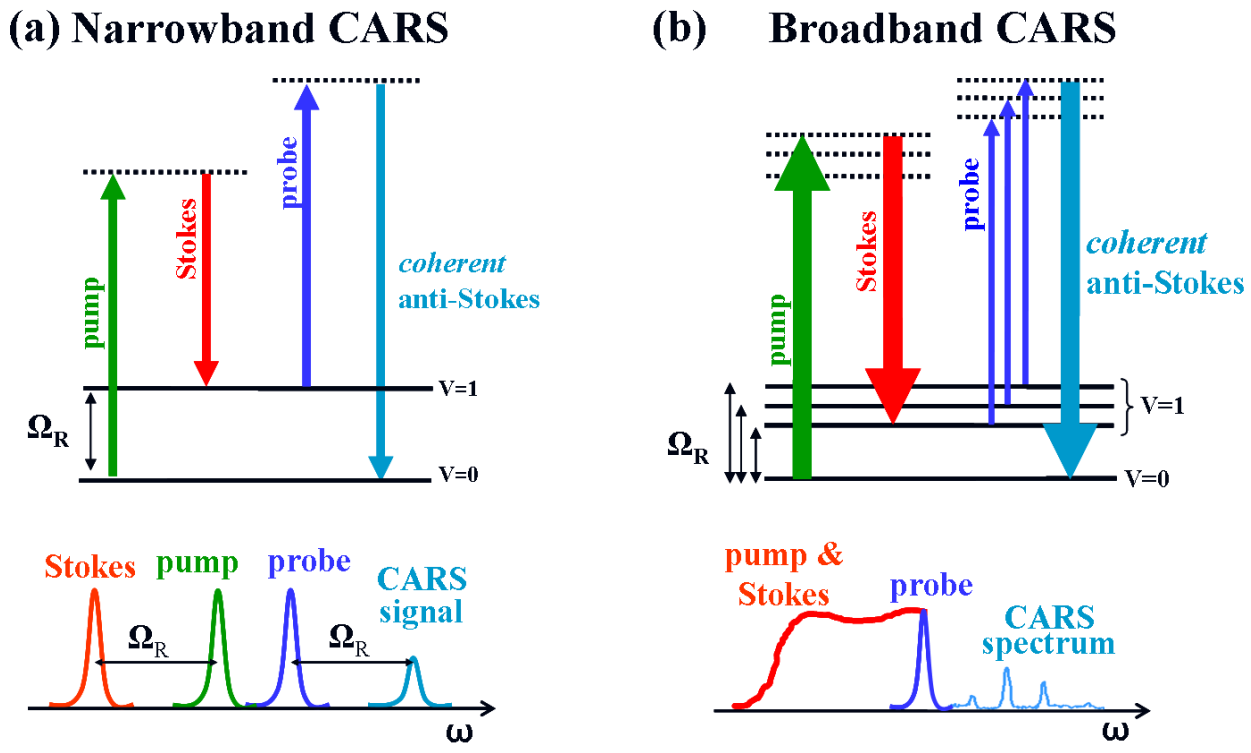

Figure 2.2 Schematic of (a) narrowband vs (b) broadband CARS processes.

2.2 Single-beam, broadband CARS microscopy

A variety of novel coherent anti-Stokes Raman scattering (CARS) methods have been developed in recent years that utilize ultrafast lasers, sometimes with a chirped or fiber-broadened spectrum, to obtain broadband vibrational information from molecules.[92-102] For a narrow bandwidth probe, these techniques typically employ a second, narrowband laser or use a split beam in two paths to generate the broadband and narrowband components separately. An important advantage of these broadband methods for microscopy is that full chemical composition analysis is possible in a single microscope scan, rather than the multiple scans that are necessary with narrowband CARS microscopy. However, due to the high peak-power of the ultrafast pulses, purely electronic four-wave mixing processes within the sample lead to a much larger NR background across the entire spectrum [not shown in Figure 2.2(b)]. This large NR signal and its corresponding shot noise have been the primary challenge for implementing sensitive broadband CARS spectroscopy. Since this NR signal results from the interaction of the laser field with the sample of interest, creative manipulations are necessary for suppression or elimination of this NR background so that the much smaller intensity resonant spectrum can be obtained.

An important breakthrough came when phase and polarization pulse shaping techniques were employed to obtain multiplex CARS spectra with a single laser beam from an ultrafast laser, eliminating complications associated with tuning, timing and alignment between two separate beams.[103] The whole array of pump and Stokes frequencies were provided simultaneously by the broadband pulse, and the resulting coherent molecular vibrations were probed by a narrow spectral part of the total bandwidth within the same laser pulse. The narrow probe part of the beam was differentiated only by shifting the phase and polarization of that narrow spectral region of the laser pulse, but not separated spatially from the broadband part of the beam. Furthermore, single-beam pulse shaping methods were developed to significantly reduce or eliminate the NR background,[104] and fingerprint-region CARS spectra with up to 700 cm^{-1} of bandwidth were previously obtained.[105]

A novel variation of this pulse shaping and signal acquisition scheme developed previously in our laboratory improves the sensitivity to allow spectra and spectral images to be obtained in an even shorter acquisition time with up to 1000 cm^{-1} of bandwidth per spectrum.[88] The essential feature of this method is the use of a single, femtosecond (fs) pulsed laser, which simultaneously provides all three photons necessary to produce the CARS signal, followed by pulse shaping and spectral interferometry of the signals within the single beam. Rather than eliminating the NR signal prior to detection, the NR signal is utilized as a local oscillator for homodyne amplification of the resonant signal. With this fast, single-beam, broadband CARS spectroscopy, spectral images are acquired in the vibrational fingerprint regime,[89] and the time-dependent spectra during photochemical conversion are measured to determine solid-state cross-linking kinetics of HSQ.[79]

2.2.1 Double Quadrature Spectral Interferometry (DQSI) CARS

Figure 2.3 shows the experimental system used for this single-beam broadband CARS technique, called double quadrature spectral interferometry (DQSI) CARS. [106] [88] A Ti:Sapphire oscillator with ~15 fs pulses operating at a repetition rate of 90 MHz provides ~120 nm of

bandwidth centered at a wavelength of ~800 nm (MTS, KM Labs). After the laser beam is expanded, it passes through an all-reflective 4*f* geometry pulse shaper, shown in Figure 2.4. It is dispersed horizontally (parallel to laser table) by an 800 grooves/mm diffraction grating, collimated by a spherical mirror, passed through a dual-mask spatial light modulator (SLM 640-D, CRi), and then refocused and re-compressed by an additional spherical mirror and grating. The SLM consists of two banks of 640 liquid crystal pixels whose birefringence is controlled by changing the applied voltage to the individual pixels, explained in detail in the following section.

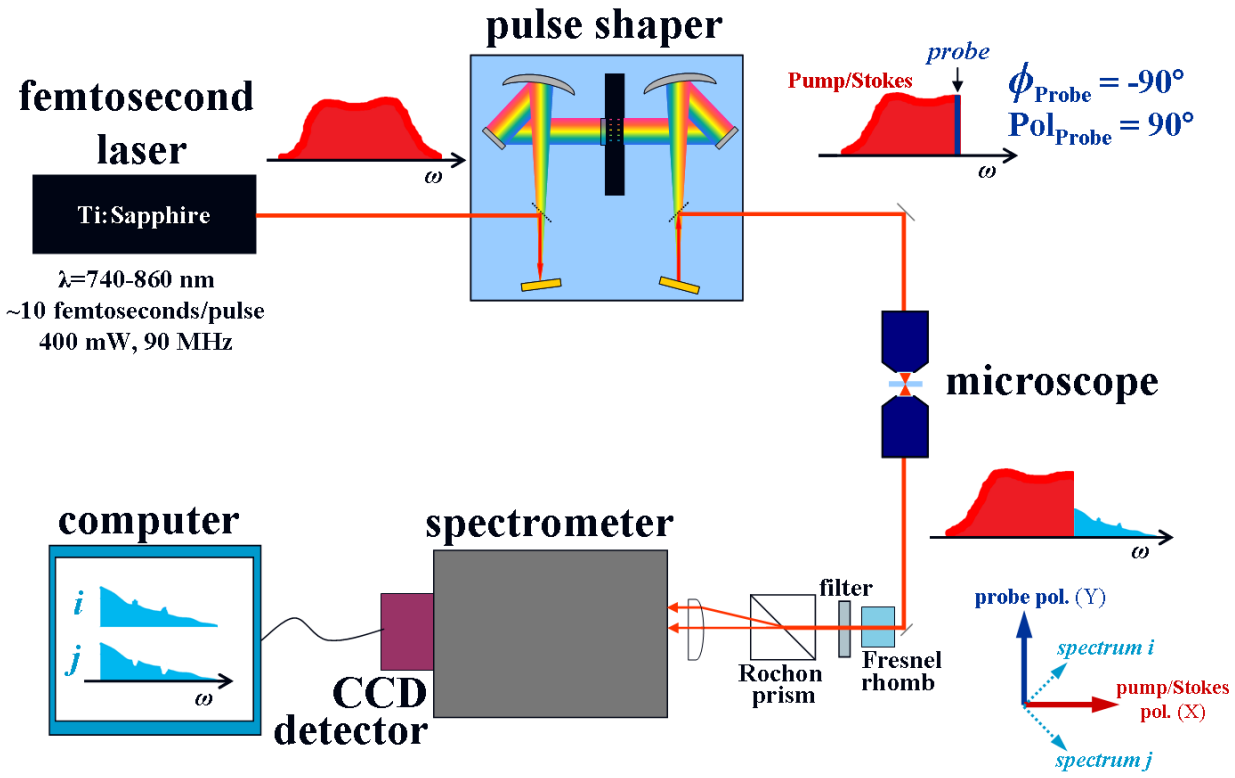

Figure 2.3 DQSI CARS experimental setup.

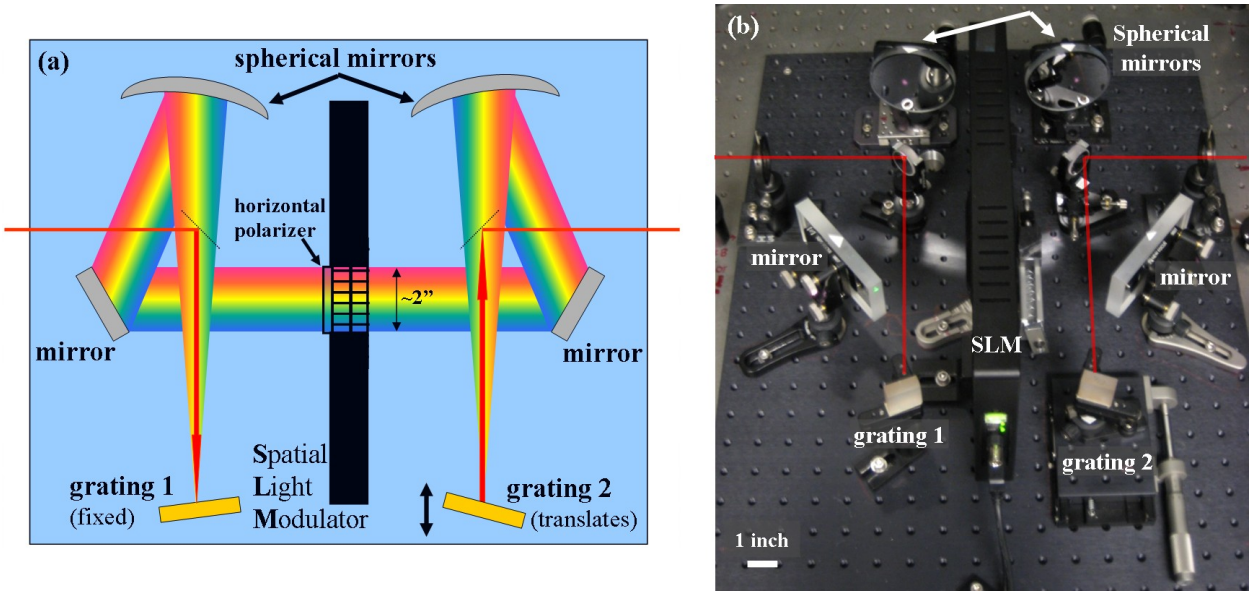

Figure 2.4 (a) Schematic top view of pulse shaper, with SLM at center. (b) Top view photograph of pulse shaper. Note that the dispersed beam passes over the top of the small entrance and exit mirrors.

The pulse shaper serves two purposes: producing a narrowband probe field within the broadband beam, and compressing the spectral phase (chirp) introduced in the ultrafast pulse along the beam path. As the dispersed laser beam passes through the SLM, the probe field is differentiated from the remainder of the spectrum by shifting the phase and polarization of just a very narrow portion of the spectrum, which is described in detail below. Furthermore, with such a broad bandwidth spectrum, any difference in optical path length between the different frequencies introduces significant spectral phase, corresponding to temporal dispersion (chirp) which stretches the pulse duration and lowers the peak power. The SLM can be used to compensate for this spectral phase, resulting in the shortest possible pulses and highest peak power at the sample position in the microscope focus, a critical factor in achieving high CARS signal intensity and multiphoton HSQ cross-linking. The pulse shaping and chirp compression techniques are explained in the following section (2.2.2).

After phase and polarization pulse shaping, the beam is again collimated and the light is focused through a 1.2 numerical aperture (NA), near IR optimized, water immersion microscope objective (60× UPlanApo, Olympus) into a condensed phase sample on an XY piezoelectric translation stage (Physik Instrumente). After interaction with the sample, the light is collected through a 0.85 NA air objective or 1.0 NA water immersion objective (60x PlanFluor, Olympus) and the laser frequencies are filtered out with a sharp-edge short-wave pass filter (740 AESP, Omega Optical). The polarization of the light is rotated by 45° by an achromatic half-wave plate (Fresnel rhomb, CVI), and the signal is split spatially into two separate directions using a Rochon prism (CVI). Both signal traces are focused into a spectrometer (SP-2300i, PI-Acton) and the resulting spectra are imaged onto a two-dimensional CCD detector (DV-401-FI, Andor).

The resonant (CARS) and NR parts of the signal can be considered independently, where P_R is the resonant transient induced polarization, given by:

$$P_R(\omega) = \int_0^\infty \chi_R^{(3)}(\Omega) E_{\mathrm{Pr}}(\omega - \Omega) A(\Omega) d\Omega \qquad \textbf{(2.9)}$$

and P_{NR} is the NR transient induced polarization:

$$P_{NR}(\omega) = \int_0^\infty \chi_{NR}^{(3)}(\Omega) E_{\mathrm{Pr}}(\omega - \Omega) A(\Omega) d\Omega . \quad \textbf{(2.10)}$$

$E_{\mathrm{Pr}}(\omega\text{-}\Omega)$ is the narrowband probe, and the amplitude of the excitation is given by:

$$A(\Omega) = \int_0^\infty E_P(\omega') E_S^*(\omega' - \Omega) d\omega' \quad \textbf{(2.11)}$$

where E_P and E_S are the pump and Stokes fields, respectively. Thus, the resonant and NR contributions to the total signal, $S(\omega)$ are:

$$S(\omega) = \left| P_R(\omega) + P_{NR}(\omega) \right|^2 = P_R^*(\omega) P_R(\omega) + P_{NR}(\omega)^2 + P_{NR}(\omega)\left[P_R^*(\omega) + P_R(\omega) \right] \quad \textbf{(2.12)}$$

As noted in the previous section, the NR contribution is entirely real, but the resonant part of the signal contains both real and imaginary parts. This is evident by approximating E_{Pr} as a delta function and inserting the equations for the third order susceptibility (equations 2.6 and 2.7) into equations 2.9 and 2.10, giving:

$$P_R(\omega) \approx \alpha_R A(\omega - \omega_{\mathrm{Pr}}) L(\omega) e^{i\phi_{\mathrm{Pr}}} \quad \textbf{(2.13)}$$

$$P_{NR}(\omega) \approx \alpha_{NR} \int_0^\infty \frac{A(\Omega)}{\Omega} d\Omega \quad \textbf{(2.14)}$$

where $L(\omega)$ is now the Lorentzian lineshape function for the resonant CARS:

$$L(\omega) = \sum_R \frac{a_R}{\Omega_R + \omega_{\mathrm{Pr}} - \omega + i\Gamma_R} . \quad \textbf{(2.15)}$$

The purely resonant part of the total signal, $P_R^*(\omega) P_R(\omega)$, is the smallest term while the NR part, $[P_{NR}(\omega)]^2$, is the largest term. The cross term in equation 2.12, $P_{NR}(\omega)[P_R^*(\omega) + P_R(\omega)]$, is linear in the NR contribution, but also contains the real and imaginary parts of the resonant contribution. The technique used here detects this larger cross-term, in which the NR signal effectively amplifies the resonant signal, so-called homodyne amplification.

The NR background and resonant CARS signals are coherent and phase locked with each other. While the resonant signal depends on the phase of the probe part of the pulse, most of the NR signal is produced by the broadband part of the pulse, which has a different phase. Thus, it is possible to implement interferometry between the resonant and NR parts of the signal by controlling the phase difference between them. Inducing different phase shifts in the probe part of the pulse with respect to the broadband part results in different spectral interference between the resonant and NR signals that are acquired simultaneously. Also, in order to directly obtain the resonant CARS spectrum using broadband pulses, the NR background must be eliminated. By altering the polarization of the probe part of the pulse, the signal can be separated into two slightly different spectra (*i* and *j*), as shown in Figure 2.5(a) and (b). The resonant contributions to these two spectra are equal in magnitude but opposite in sign:

$$P_R^i(\omega) = \frac{1}{\sqrt{2}} P_R \qquad \text{and} \qquad P_R^j(\omega) = -\frac{1}{\sqrt{2}} P_R \quad \textbf{(2.16)}$$

while the signals at both polarizations contain the same NR background:

$$P_{NR}^i(\omega) = P_{NR}^j(\omega) = \frac{1}{\sqrt{2}} P_{NR}(\omega) \quad \textbf{(2.17)}$$

resulting in an equal but opposite interference between the resonant and NR signal in the two spectra (*i* and *j*) at the vibrational resonances, shown in Figure 2.5(b) for toluene. Note that these two spectra are acquired simultaneously on the CCD. Thus the total signal in each trace is obtained by plugging 2.16 into equation 2.12:

$$S^i(\omega)=\left|P_R^i(\omega)+P_{NR}^i(\omega)\right|^2 \qquad \text{and} \qquad S^j(\omega)=\left|P_R^i(\omega)+P_{NR}^j(\omega)\right|^2 \tag{2.18}$$

Expanding 2.18 and subtracting one spectrum from the other results in the difference signal:

$$S^i(\omega)-S^j(\omega)=2\alpha_R|P_{NR}|A(\omega-\omega_{\mathrm{Pr}})(\mathrm{Re}[L(\omega)]\cos\phi_{\mathrm{Pr}}-\mathrm{Im}[L(\omega)]\sin\phi_{\mathrm{Pr}}). \tag{2.19}$$

Thus, with ϕ_{Pr}=-90 the real part becomes zero and only the imaginary part of the lineshape is detected, corresponding directly to the spontaneous Raman scattering line shape, as shown in Figure 2.5(c). Considering that the resonant signal is much smaller than the non-resonant, the sum of the signals, S^i+S^j, will be mostly non-resonant signal. Thus, the normalized signal intensity, S_N, in units of $\sqrt{counts}$, is equivalent to non-amplified field amplitude of the resonant CARS signal only, given by:

$$S_N(\omega)=\frac{S^i(\omega)-S^j(\omega)}{\sqrt{S^i(\omega)+S^j(\omega)}}\approx 2\alpha_R A(\omega-\omega_{\mathrm{Pr}})\mathrm{Im}[L(\omega)] \tag{2.20}$$

Because the two signal traces are detected 90° out of phase (in quadrature), the method is called double quadrature spectral interferometry (DQSI) CARS.[88]

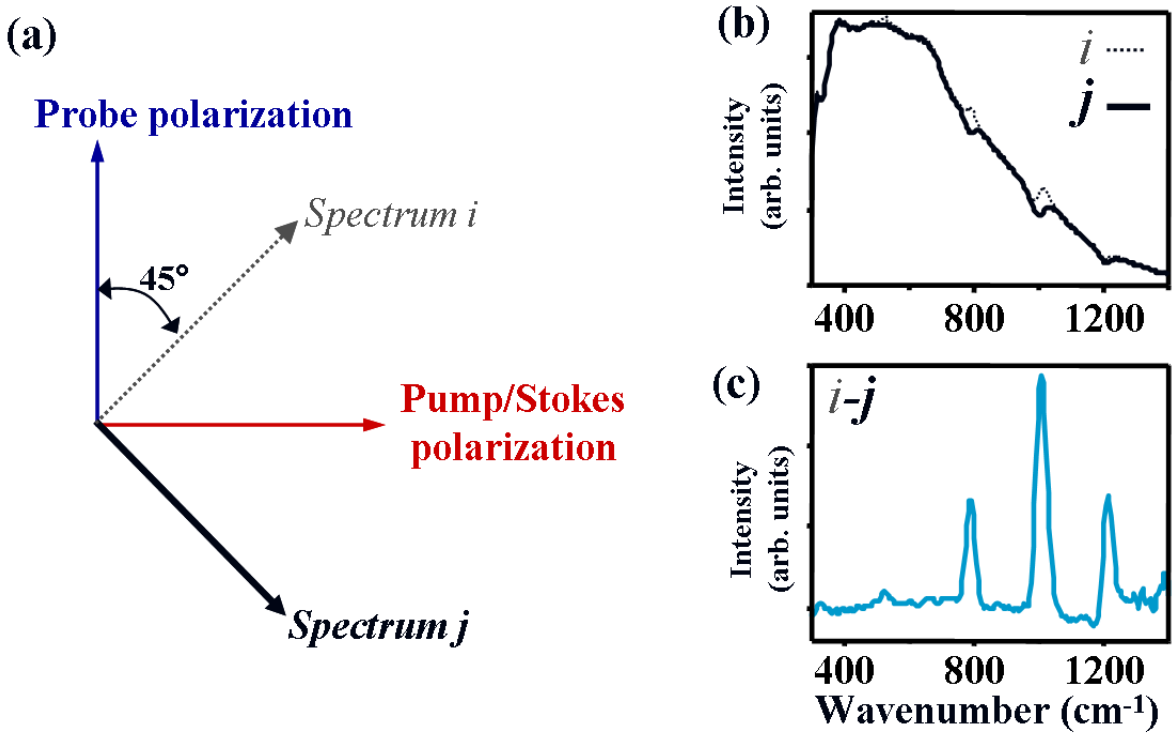

Figure 2.5 DQSI CARS detection scheme,[107-108] showing (a) polarization of incident fields and detected signals, (b) total signal from toluene for each spectrum and (c) difference of two signals.

Note that the NR signal from the sample itself serves as the local oscillator here, which amplifies the resonant signal significantly, providing a sensitivity improvement over previous CARS spectroscopy techniques in which the NR signal is suppressed prior to detection. Since the local oscillator comes from the sample itself, this is called homodyne amplification. Heterodyne amplification of the CARS signal has been previously demonstrated, where the resonant and NR spectra were acquired separately from different samples, followed by interfermometry between the two signals using an interferometer.[100, 109] The key improvement here is that there is no need for separate beams prior to the sample or an interferometer, since the

interferometry takes place within the single beam. Thus the key advantages of this technique (versus other broadband CARS techniques) are the single beam configuration, signal enhancement by homodyne amplification with the NR signal, and the Raman-like line shape. Furthermore, the normalized signal intensities are linearly proportional to the concentration of the vibrational modes/molecules being detected, as in spontaneous Raman spectroscopy; this is not the case in most other CARS microscopy techniques.

Sample damage due to three-photon absorption and subsequent local heating is a limiting factor in many types of samples. Samples in solution or surrounded by water show increased resilience to photo-degradation, but fast scan rates make it possible to acquire spectral images of more readily damaged polymers; an example of this is shown in Figure 2.6.[108, 110] A thin-film of polymethylmethacrylate (PMMA) and polystyrene (PS), which are known to phase separate,[111] is prepared by dissolving 1:1 PMMA/PS in chloroform and spin-casting the solution into a film approximately 2-5 μm thick (verified with AFM). The sample is placed in the microscope perpendicular to the laser beam and scanned through the laser focus in the XY direction with the piezoelectric translation stage. A spectrum is obtained in 10 ms for each pixel in the image. The spectra for the individual materials are shown in Figure 2.6(a)-(b). The image is 100 pixels × 100 pixels, containing a total of 10,000 separate spectra. The total image size is 20 μm × 20 μm, and the total time for data acquisition and transfer is about 3.5 minutes. The spectra for the two polymers have similar features around both 1000 cm^{-1} and 800 cm^{-1}, so chemically selective imaging requires a full spectrum and analysis of the ratio of the peak intensities for each pixel in the image. The false-color contrast scale for the image in Figure 2.6(c) is shown, where the bright red corresponds to 1000 cm^{-1}/800 cm^{-1} = 4, the ratio of the spectral peaks in the pure PS spectrum, and the dark blue is 1000 cm^{-1}/800 cm^{-1} = 0.5, corresponding to pure PMMA. With current state-of-the-art spontaneous Raman microscopy systems, it typically takes one second or more to acquire each of these spectra with the same signal-to-noise ratio, which would result in a total imaging time of three hours for a scan of similar size and spatial resolution. The spatial resolution in Figure 2.6 is about 400 nm, which is less than expected theoretically. Due to the third order nonlinearity of the CARS signal, enhanced spatial resolution of 230 nm is expected under these conditions, and <300 nm resolution has previously been observed.[75, 89] The degradation of the spatial resolution is most likely the result of slight chromatic aberrations and misalignment through the focusing objective, which can be significant due to the exceptionally broad bandwidth of the spectrum.

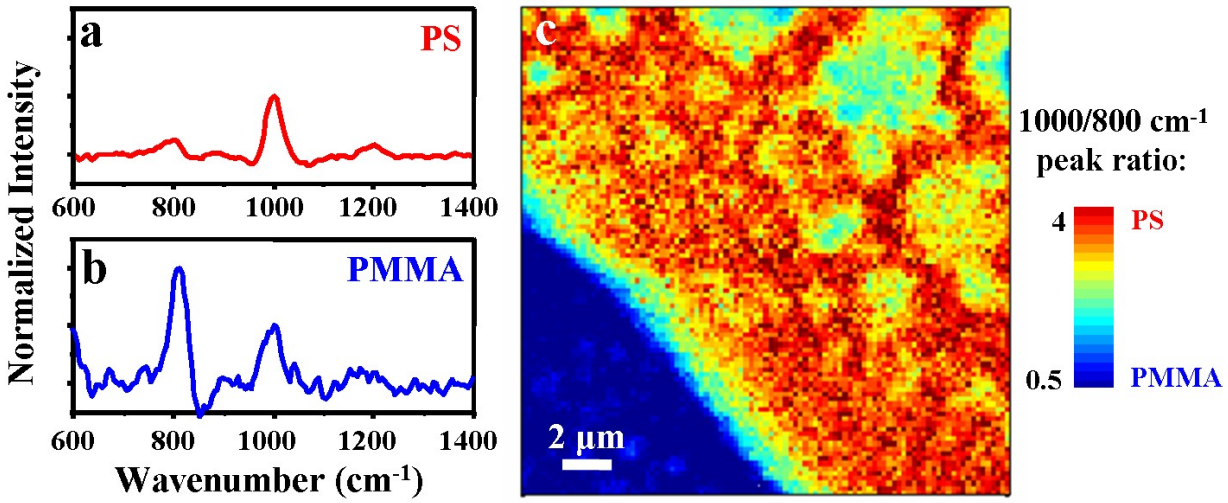

Figure 2.6 DQSI-CARS spectra of (a) PS and (b) PMMA, acquired in 10 ms each. (c) DQSI CARS spectral image of a self-segregated PMMA/PS blend, acquired in 3.5 minutes.[108, 110]

Acquiring the full spectrum at each pixel enables not only imaging of multiple components with similar spectral features, but also ratiometric analysis of the relative amounts of each component at a particular position. For example, in Figure 2.6(c), regions containing a blend of PS and PMMA are observed, shown in light blue, green and yellow, depending on the fraction of PMMA or PS present. This is important for the study of HSQ photoresists because the cage and network structures, and hence their Raman spectra, are very similar. For imaging and microspectroscopy, the amount of cage versus cross-linked HSQ at each sample position is desired, which reveals the relative degree of cross-linking. Spontaneous Raman and CARS spectra of HSQ thin films are not found in the literature, so they are reported with the experimental results in section 3.4.

2.2.2 Pulse Shaping and Compression with a Spatial Light Modulator

The heart of the single beam, broadband CARS microscope is the dual mask, liquid crystal spatial light modulator (SLM), shown in Figure 2.7. This device allows independent control of the phase and polarization of individual frequency components of the broadband laser spectrum; with the simple addition of an exit polarizer, this translates to phase and amplitude control. With 640 pixels spanning the full laser spectrum from 700 to 900 nm, each SLM pixel controls a spectral range of ~0.3 nm. As the precise control of the SLM is critical to obtain the CARS spectra and control the peak power at the microscope focus for multiphoton absorption polymerization, a brief explanation of its operation is given here. Interestingly, the dispersed laser spectrum is visible in the photographs in Figure 2.7(a) (see right side of SLM, higher order diffraction) and Figure 2.7(b) (center of entrance polarizer, first order diffraction). The blue and orange colors in Figure 2.7 are an artifact of the photography, but the blue side does correspond to the lower wavelength (700 nm) and the orange side is the higher wavelength (900 nm).

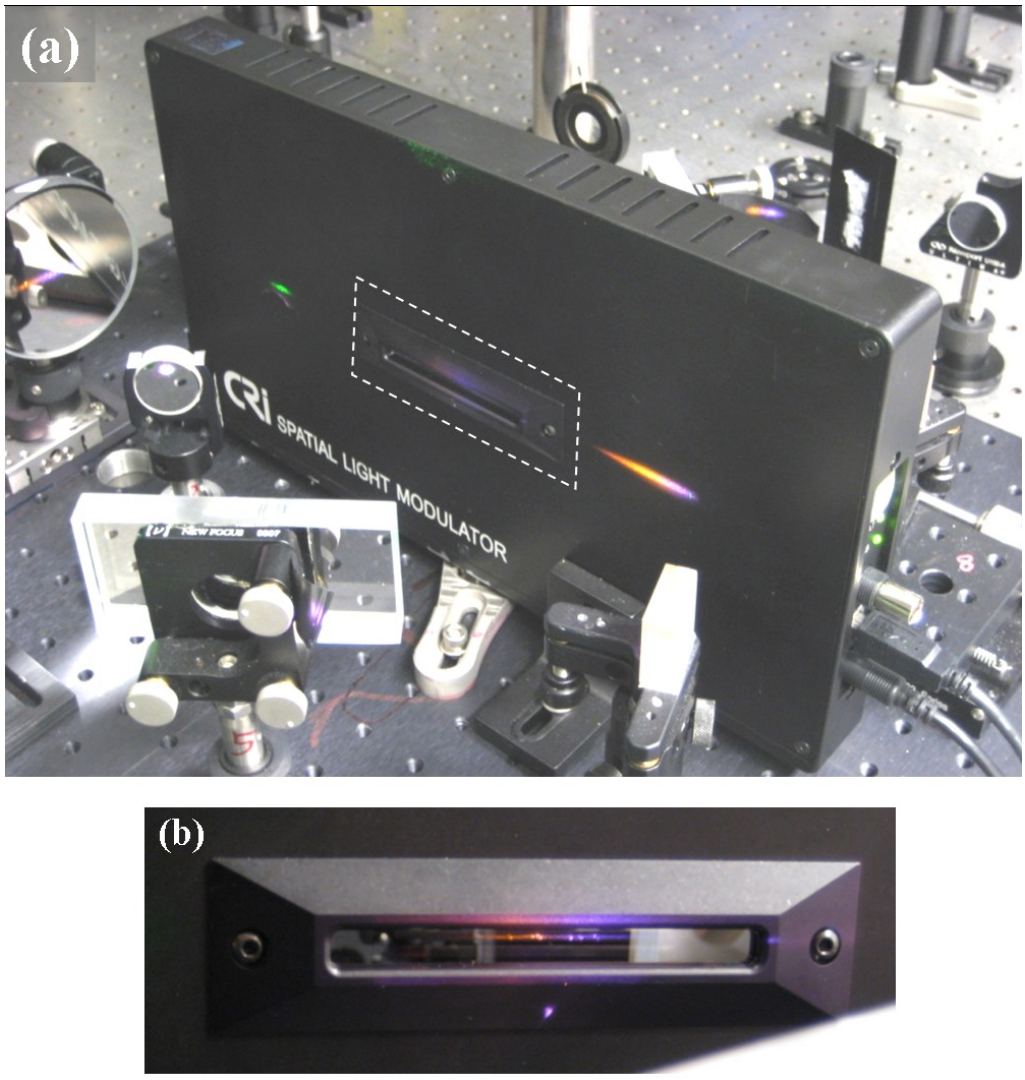

Figure 2.7 (a) Photograph of SLM (front), with dashed line around entrance polarizer. (b) Close up of entrance polarizer, showing faint back reflection of broadband laser spectrum.

The main components of the dual-mask SLM are an entrance polarizer, two masks of 640 liquid crystal (LC) pixels and an (optional) exit polarizer, shown in Figure 2.8. The light from the oscillator is horizontally polarized, so the horizontal entrance polarizer of the SLM serves only to ensure pure polarization enters the LC masks. After the entrance polarizer is the first liquid crystal mask. Each pixel of this mask consists of nematic phase liquid crystal molecules with their optical axes oriented at +45° with respect to the incident light polarization along the XY plane (which is perpendicular to the beam propagation axis), as shown in Figure 2.9. When a voltage is applied vertically across the pixel, the molecules rotate in the z-axis (beam axis), out of the XY plane. The voltage, and therefore the amount of Z-tilt of the molecules, determines the amount of retardance (phase shift) imparted to the incident light. The same pixel in the second mask contains liquid crystal pixels with their optical axes oriented orthogonal to the first mask; in other words, at -45° with respect to the incident light. In the same way, a voltage applied vertically to this pixel will rotate the molecules in the Z-axis, and shift the phase of the incoming light accordingly.

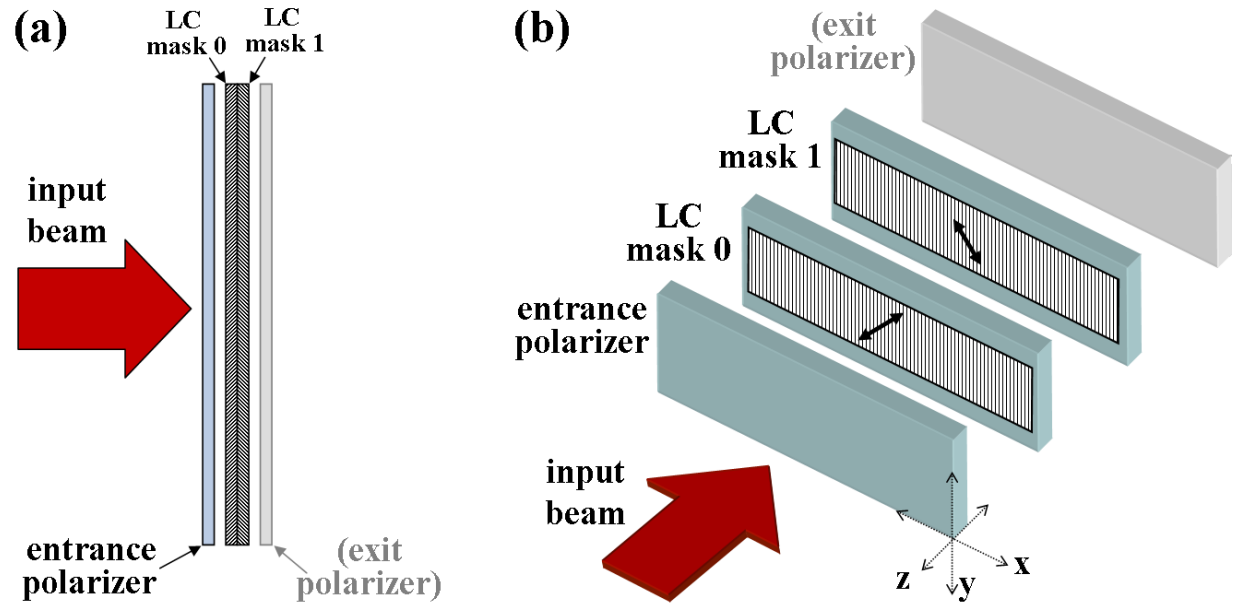

Figure 2.8 Schematic representation of SLM liquid crystal (LC) masks and polarizers, (a) top view and (b) front perspective view. Bold black arrows represent the optical axis of the individual LC molecules within each mask. For DQSI CARS, the exit polarizer is removed completely.

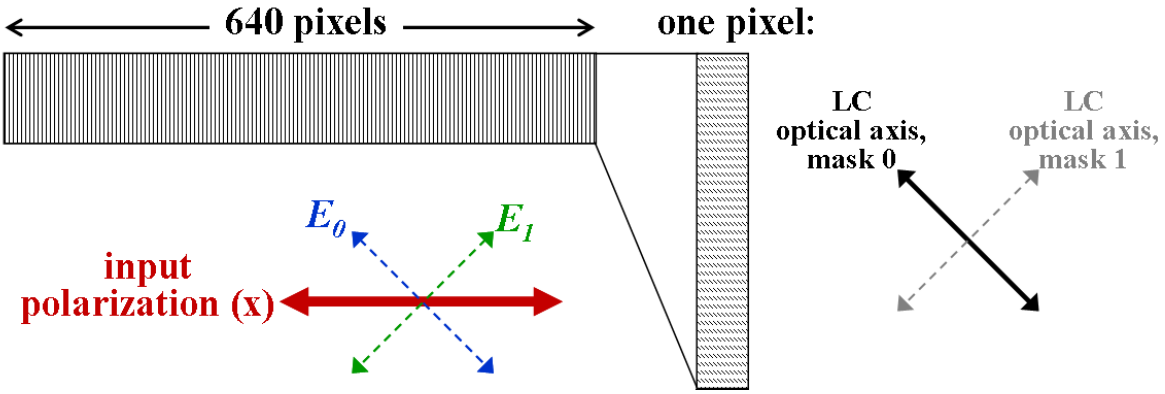

Figure 2.9 Front view schematic of liquid crystal (LC) mask, showing orientation of incoming light polarization and its orthogonal components with respect to LC optical axes.

To operate as a phase only modulator, the same phase is shift is applied with both masks, introducing an overall phase shift, $\Delta\Phi$ of:

$$\Delta\Phi = \frac{\Delta\phi^{(0)}(V) + \Delta\phi^{(1)}(V)}{2} \tag{2.21}$$

where $\Delta\phi^{(0)}(V)$ and $\Delta\phi^{(1)}(V)$ are the voltage dependent birefringence (phase shift) of the liquid crystals in mask 0 and mask 1, respectively. If a different amount of phase shift is introduced at each mask, then the overall polarization of the light will be altered based on the difference in phase experienced by the orthogonal polarization components of the incoming light, analogous to the principle of a half-wave plate (shown in Figure 2.10). The output polarization will differ from the input polarization by the angle $\Delta\theta$, where:

$$\Delta\theta = \frac{\Delta\phi^{(0)}(V) - \Delta\phi^{(1)}(V)}{2}. \tag{2.22}$$

Accordingly, when the exit polarizer is in place, this difference term corresponds to output amplitude control instead, such that phase and amplitude modulation of the spectrum is possible. The factor of two in the denominator in equations 2.21 and 2.22 is based on the fact that $\Delta\phi^{(0)}(V)$ and $\Delta\phi^{(1)}(V)$ are not overall phase offsets of the electromagnetic field, but offsets in the orthogonal components of the field; physically, this can be understood by testing how phase shifts of the orthogonal components in Figure 2.10 will effect the overall phase shift of the field.

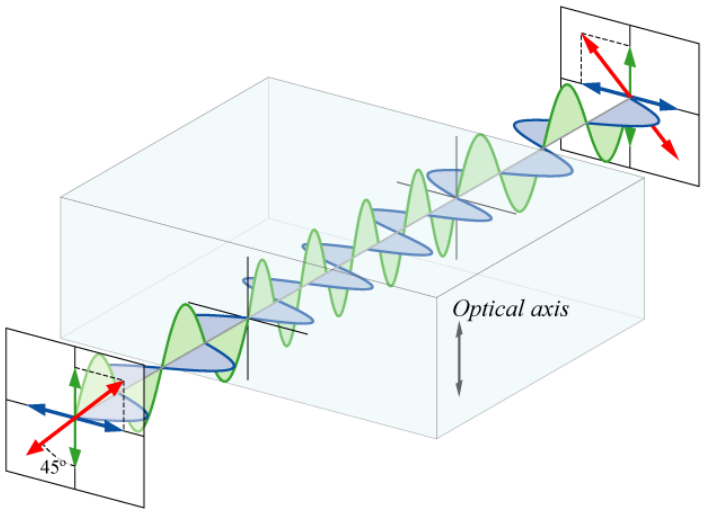

Figure 2.10 Schematic diagram of a birefringent crystal based half-wave plate, showing 90° rotation of incident light polarization (red) by introducing a 180° phase shift between of the E_x (blue) and E_y (green) components. As in the SLM, the incident light here is polarized at 45 degrees with respect to the optical axis of the crystal.[112]

When the exit polarizer is removed, then the output phase and polarization can be controlled, and thus the SLM operates essentially as a variable-polarization waveplate. Thus the total output field depends upon the applied phase shifts as:

$$\begin{aligned}\vec{E}_{out} &= \frac{E_{in}}{2}\left[\exp\left(i\Delta\phi^{(0)}\right)\left(\vec{x}+\vec{y}\right)+\exp\left(i\Delta\phi^{(1)}\right)\left(\vec{x}-\vec{y}\right)\right] \\ &= E_{in}\exp\left[\frac{i\left(\Delta\phi^{(0)}+\Delta\phi^{(1)}\right)}{2}\right]\left[\vec{x}\cos\left(\frac{\Delta\phi^{(0)}+\Delta\phi^{(1)}}{2}\right)+i\vec{y}\sin\left(\frac{\Delta\phi^{(0)}-\Delta\phi^{(1)}}{2}\right)\right],\end{aligned} \tag{2.23}$$

where $\vec{E}_{out}$ is the total output field, E_{in} is the amplitude of the incident x-polarized light, and $\vec{x}$ and $\vec{y}$ polarized components of the output field, respectively.[113] Again, there will be no intensity in the y-polarized output field if there is no difference in phase applied between mask 0 and mask 1, corresponding to no shift in the overall polarization.

During DQSI CARS experiments, the desired output phase and polarization are the known quantities, while the phase shift needed at each LC mask is unknown. Combining equations 2.13 and 2.14, we can solve for the phase shift required at each mask for a desired total output phase and polarization shift:

$$\begin{aligned}\Delta\phi^{(0)}(V) &= \Delta\Phi - \Delta\theta \\ \Delta\phi^{(1)}(V) &= \Delta\Phi + \Delta\theta\end{aligned} \tag{2.24}$$

For example, if no phase shift and 90° polarization change is desired, the phase difference between mask 0 and 1 should be 180°, requiring $\Delta\phi^{(0)} = +90°$ and $\Delta\phi^{(1)} = -90°$. The actual value sent to the SLM is a voltage, so to achieve the desired phase shift at each LC pixel, a careful calibration of the voltage-to-phase response of each LC mask is required with the SLM in its precise, final position within the pulse shaper.[113]

As mentioned previously, one important role of the pulse shaper and SLM is to compress the spectral phase at the sample position. When an ultrafast pulse of light passes through any medium, it acquires a frequency dependent phase shift (spectral phase), which corresponds to a stretching of the pulse in time, called chirp. The total spectral phase $\Phi(\omega)$ can be approximated by a Taylor expansion about ω_0, the central frequency of the laser spectrum:

$$\Phi(\omega) = \phi_0 + \phi_1(\omega - \omega_0) + \frac{1}{2!}\phi_2(\omega - \omega_0)^2 + \frac{1}{3!}\phi_3(\omega - \omega_0)^3 + \frac{1}{4!}\phi_4(\omega - \omega_0)^4 + \ldots \quad \textbf{(2.25)}$$

where ϕ_n is the n^{th} order spectral phase. Taking the first derivative of the spectral phase gives the group delay, τ_g:

$$\tau_g = \frac{d\phi(\omega)}{d\omega}. \quad \textbf{(2.26)}$$

The analogous quantity to the group delay in the time domain is the instantaneous frequency or chirp, $\omega(t)$, defined as the first derivative of the temporal phase, $\phi(t)$:

$$\omega(t) = \omega_0 + \frac{d\phi(t)}{dt}. \quad \textbf{(2.27)}$$

Thus the chirp is always of order n-1; that is, 2nd order spectral phase corresponds to "linear chirp," 3rd order to "quadratic chirp," and so on. More chirp (positive or negative) stretches the pulse temporally, resulting in lower peak power. The microscope objective induces not only second order spectral phase (linear chirp), which can be compressed by translating the 2nd grating of the pulse shaper (Figure 2.4), but also significant higher order spectral phase, which must be compensated at the microscope focus using the SLM. This chirp is a significant limiting factor for acquiring broadband CARS spectra, because Raman scattering occurs on timescales the order of ~1 fs, meaning that both the pump and Stokes pulses (which may be from opposite ends of the spectrum) must interact with the molecules within that time frame to populate the vibrationally excited state at $\Omega_R = \omega_P - \omega_S$ (equation 2.8). As is common in discussion of ultrafast pulses, the term "chirp" will be used when referring to the temporal effects of the spectral phase.

To measure the spectral phase at the sample focus, a procedure called multiphoton intrapulse interference phase scan (MIIPS) is utilized. Developed by a group at the University of Michigan for control of multiphoton processes, several comprehensive papers have been published regarding the theory and practice of the technique.[114] Using MIIPS, the unknown spectral phase is retrieved by measuring the second harmonic generation (SHG) spectrum while applying a known spectral phase. In the CARS microscope, a 10 μm thick β-barium borate crystal (BBO, Casix) is placed on a glass coverslip at the microscope focus and the light is carefully focused within the BBO to maximize the intensity of the second harmonic signal. The signal is collected with a 0.54 NA objective, followed by a short wave pass filter to remove the transmitted laser light (740 AESP, Omega Optical) and measured with a fiber-coupled spectrometer (USB2000, Ocean Optics). Once it is known, the spectral phase is fit to a 4th order polynomial and is pre-compensated by applying the opposite spectral phase profile on the SLM. Then the MIIPS routine is run again, to monitor how well the chirp is compressed by this spectral phase function; 2-3 iterations of the MIIPS routine are typically required to compress the

higher order spectral phase to within ~1 radian, which is more than sufficient for strong CARS signal intensities.[89, 115] The quality of the chirp compression determines the length of the pulse at the focus; better chirp compression results in a shorter laser pulse at the focus, and therefore higher peak power per pulse, which results in higher CARS signal and faster HSQ cross-linking rates. This is explained in more detail in the context of experimental results in chapters 3 and 4.

2.3 Near edge X-ray absorption fine structure (NEXAFS) spectroscopy

Optical microscopy provides resolution on the order of 200-400 nm at best. With much shorter wavelengths, X-ray microscopy can provide imaging and micro-spectroscopy at resolutions far exceeding this, as low as 30 nm with current widely-available technology, and the next generation of microscope technology gives 15 nm resolution.[10-12] The power of scanning transmission X-ray microscopy (STXM) is that it enables mapping of functional group composition with ~30 nm resolution by acquiring the full NEXAFS spectrum within the tight X-ray focus.

At X-ray energies near a core shell binding energy of a particular element of interest, there is an increase in the absorption cross-section, the so-called absorption edge, resulting from the single-photon ionization of the core electron. The absorption probability near this edge is further enhanced when the X-ray energy is in resonance with a transition from the core to an unoccupied molecular orbital (MO), leading to peaks (i.e. fine structure) in the near edge X-ray absorption spectrum, as shown schematically in Figure 2.11. The spectral features just below and within about 30 eV above the edge are therefore sensitive to bond angle, length, orientation, and local bonding environment within the sample, providing a fingerprint of the functional group(s) within which the element resides.[116-117] Note that some unoccupied MOs lie above the vacuum level/ionization potential, as shown in Figure 2.11 and are therefore referred to as quasi-bound states. For core-excited molecules, it is also possible for some unoccupied MOs to be shifted in energy away from their expected ground state configurations; e.g. states lying above the vacuum level can be shifted below it. Interference between outgoing photoelectrons and those backscattered from neighboring atoms also leads to energy-dependent oscillations in the X-ray absorption intensity, which decay with increasing energy above the absorption edge. These oscillations extend out to 100 eV or more above the edge in highly ordered samples such as diamond and graphite, and so these features are known as the extended X-ray absorption fine structure (EXAFS) and are a further measure of bond length and long range order in the sample.[116]

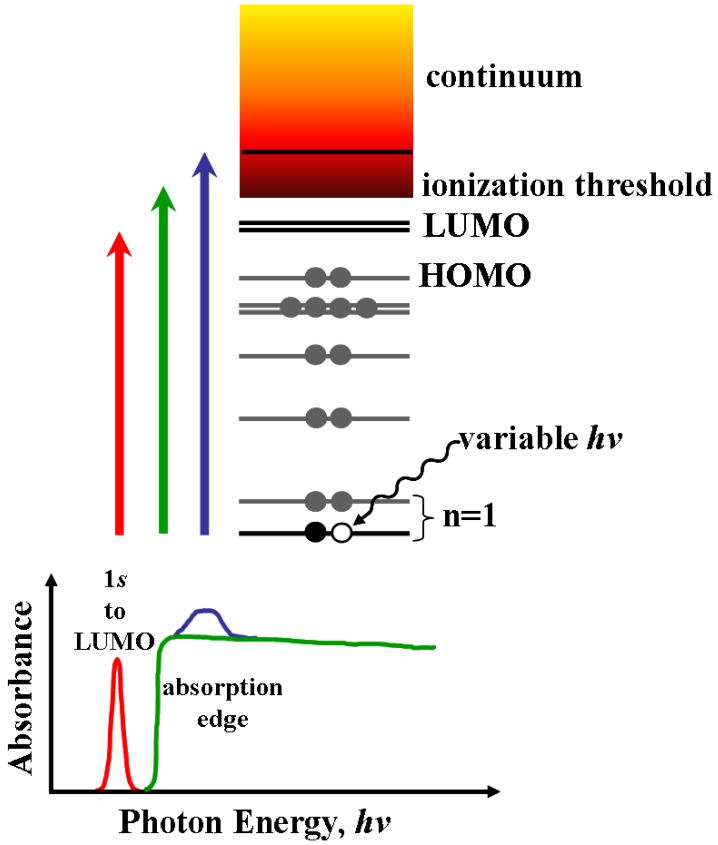

Figure 2.11 Simplified schematic of near-edge X-ray absorption process, showing possible transitions to the lowest unoccupied molecular orbital (LUMO), continuum and quasi-bound MO.[117]

		K-edge		L-edge		l_{abs} (nm)	
Element	**Z**	**E (eV)**	**λ (nm)**	**E (eV)**	**λ (nm)**	**E= 100 eV**	**E=1 keV**
C	6	284	4.36	--	--	190	2100
N	7	410	3.02	--	--	--	--
O	8	543	2.28	--	--	--	--
H_2O						160	2300
Si	14	1839	0.674	99	12.5	63	2700

Table 2.1 Comparison of selected elemental X-ray absorption edge energies and absorption depths, where l_{abs} = 1/*e* absorption depth for the photon energies listed.[4] These values vary slightly with chemical environment.

The core shell binding energies of some atoms are detailed in Table 2.1. The n=1 state (*s* orbital) is called the K-shell, n=2 (*p* orbital) the L-shell and n=3 (*d* orbital) the M-shell; thus "K-edge absorption" refers to absorption of X-rays with energies at and just above the binding energy, E_B, of the K-shell electrons. Following X-ray absorption, the photoelectron can be promoted to an unoccupied (virtual) molecular orbital (MO) or escape into the continuum with kinetic energy $E_{kin}=\hbar\omega-E_B$, shown schematically in Figure 2.12(a).[4] The core hole left by the outgoing photoelectron can then be filled by an electron from an outer shell, resulting in fluorescence [Figure 2.12(b)] or non-radiative Auger decay [Figure 2.12(c)], where an outer shell electron fills the core hole, and the resulting energy release kicks out an additional outer shell

electron (not necessarily from the same shell), which escapes with some characterstic kinetic energy $E_{kin}<\hbar\omega-E_B$.[4] (The label on the Auger electron refers to the shell in which the hole originated (K), the shell from which the hole-filling electron came (L), and the shell from which the Auger electron was emitted (L).) Between the Auger and fluorescence pathways to fill the core vacancy, the Auger process is more probable for low-*Z* atoms (with core electron binding energy < ~2 keV), while fluorescence is dominant in high-*Z* atoms.[4]

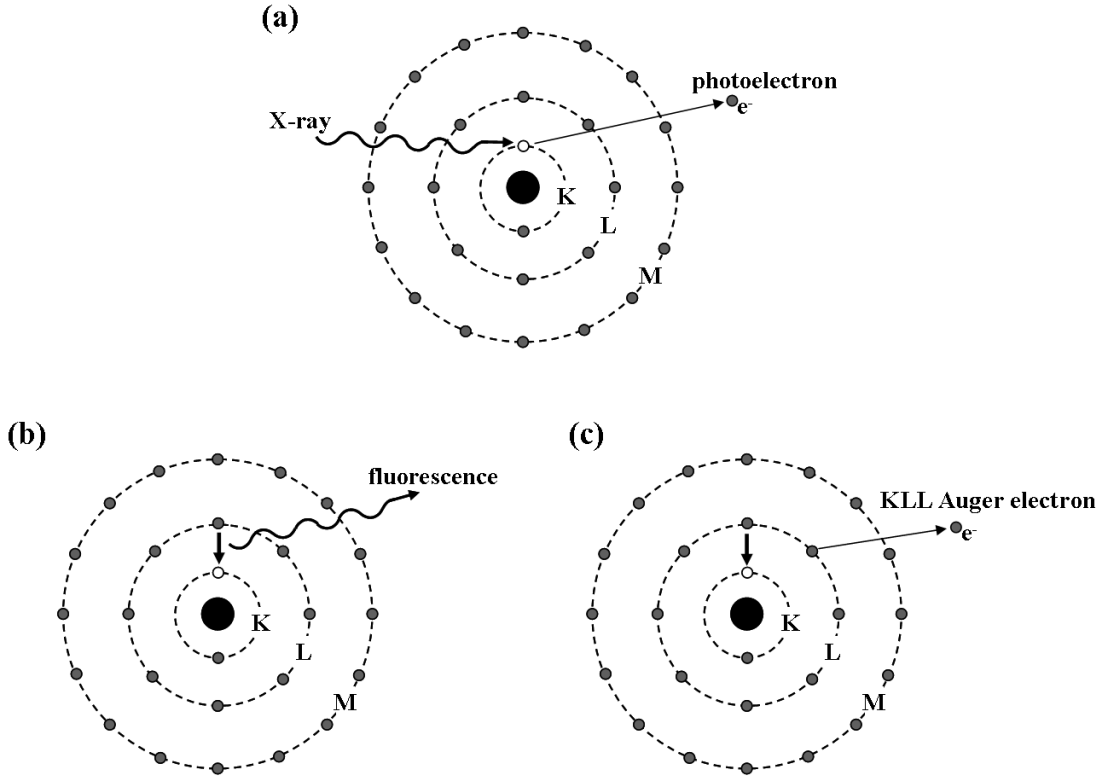

Figure 2.12 Schematic of X-ray induced core electron transitions.[4] (a) Single-photon ionization of 1*s* electron, which is followed by (b) fluorescence emission or (c) non-radiative Auger decay.

The energy dependent X-ray photoabsorption cross-section, $\sigma_{abs}(E)$, of a material is determined by the local environment of an atom, and it is enhanced when the X-ray energy is in resonance with a transition to a bound or quasi-bound electronic state of the molecule in which the atom resides. The absorption coefficient is defined as the number of electrons excited per unit time divided by the incident photon flux, $F(E)$ (the number of incident photons per unit time per unit area); thus, it has units of area, usually expressed in cm^2 or barn ($1\ cm^2 = 10^{24}$ barn):

$$\sigma_{abs}(E) = \frac{P_{if}(E)}{F(E)} \tag{2.28}$$

where $P_{if}(E)$ is the transition probability per unit time from state $|i\rangle$ to state $|f\rangle$ driven by a time-dependent harmonic perturbation, according to Fermi's "Golden Rule." From this, the absorption cross-section for transitions into the continuum is approximated as:

$$\sigma_{abs}(E) = \frac{4\pi\hbar^2}{m^2}\frac{e^2}{\hbar c}\frac{1}{\hbar\omega}\left|\langle f|\vec{e}\cdot\vec{p}|i\rangle\right|^2 g_f(E) \tag{2.29}$$

where m and e are the mass and charge of the electron, respectively, $\vec{e}$ is the unit vector of the plane electromagnetic wave of frequency ω, $\vec{p}$ is the sum of linear momentum operators of the electrons, and $g_f(E)$ is the energy density of final states, which depends upon the normalization of the wavefunctions; here, the continuum states are normalized to a Dirac delta function in the kinetic energy of the photoelectron.[116] For bound states, the absorption cross-section is approximately:

$$\sigma_{abs}(E) = C\frac{df_\omega}{dE} = Cf_\omega g_b(E) \tag{2.30}$$

where C is a constant (C=1.1 x 10^2 megabarn eV), $g_b(E)$is the bound state energy density of final states, and f_ω is the optical oscillator strength, a measure of the intensity of a particular resonance:

$$f_\omega = \frac{2}{m\hbar\omega}\left|\langle f|\vec{e}\cdot\vec{p}|i\rangle\right|^2 \tag{2.31}$$

A significant body of work on NEXAFS of small molecules has led to simple, semi-empirical rules that allow interpretation of near-edge structures independent of theoretical calculations of absorption cross-sections,[116] and so comparison to previously reported peak assignments are used to assign the NEXAFS features for HSQ spectra in this thesis.

By defining a mass-dependent elemental absorption coefficient, $\mu(E)$:[118-119]

$$\mu(E) = \frac{N_A}{M}\sum_i x_i\sigma_i(E)\,, \tag{2.32}$$

where N_A is Avogadro's number, M is the molecular mass, x_i is the number of atoms of type i per molecule, and $\sigma_i(E)$ is the atomic photoabsorption cross-section of type i atom, the X-ray transmission can be expressed simply in terms of mass density, ρ, and thickness, l, of the sample according to the Beer-Lambert law:

$$Transmission = \frac{I}{I_{in}} = e^{-\mu(E)\rho l}\,, \tag{2.33}$$

where I_{in} and I are the incident and transmitted X-ray flux, respectively. This is then rearranged and defined as the absorbance (A) or optical density (OD) of the material:

$$A = OD = -\ln\left(\frac{I}{I_{in}}\right) = \mu(E)\rho l\,, \tag{2.34}$$

which will be used extensively in this work for the quantitative analysis of NEXAFS spectra and STXM images.

Figure 2.13 is a sample oxygen K-edge NEXAFS spectrum for an HSQ thin film, showing the absorption edge "jump" and Gaussian peak fits to the near-edge resonance features. Although the strong, asymmetric feature in Figure 2.13 is fit best with two Gaussians (peaks 2 and 3, 538.5 eV and 541.2 eV, respectively), it is in reality a single peak due to one type of electronic transition. The characteristic asymmetric line shape of this peak is due to a unique type of inhomogeneous broadening.[116] Detailed peak assignments are provided in section 5.3. After NEXAFS spectra are obtained for different locations in a sample, one can determine which peak shows the greatest difference in intensity (contrast) between the species of interest, and tune the X-rays to that single energy for rapid imaging. The oxygen and silicon K-edge NEXAFS spectra of HSQ show distinct differences before and after cross-linking occurs, due to changes in

the absorption cross-section caused by a modified local bonding structure around the Si and O atoms.[50]

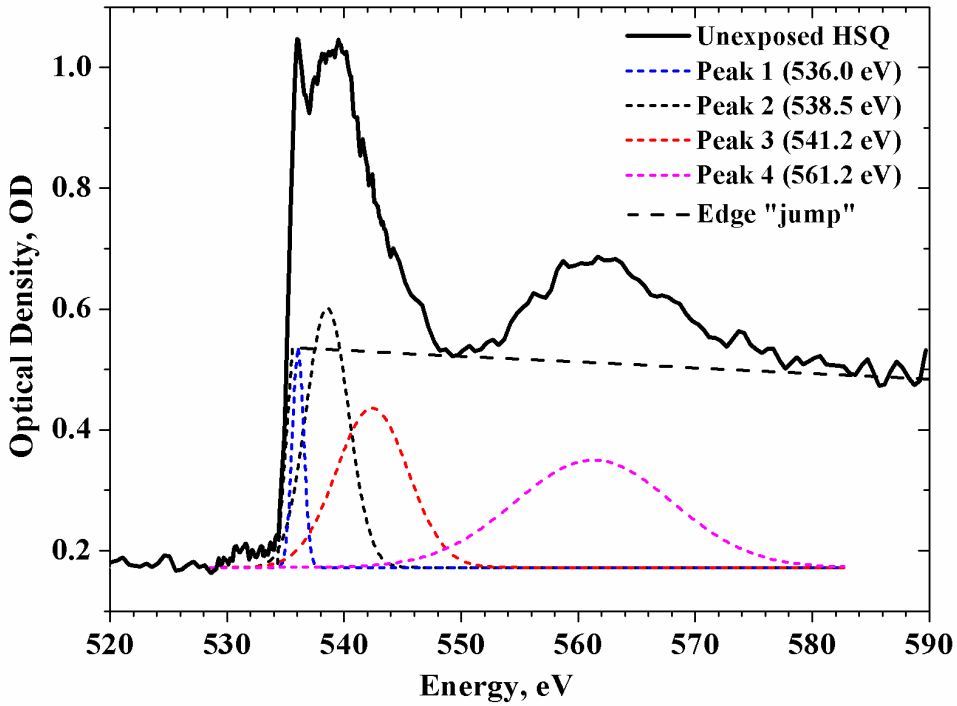

Figure 2.13 Representative oxygen K-edge NEXAFS spectrum of HSQ thin film, with Gaussian peak fitting. Placement of sharp absorption edge "jump" is approximate.

2.4 Scanning transmission X-ray microscopy (STXM)

The experiments presented in chapter 5 were performed at the STXM at beamline 5.3.2 of the Advanced Light Source (ALS) synchrotron at Lawrence Berkeley National Laboratory, hereafter referred to as the 5.3.2 STXM. The instrument was not designed as part of this work, and the design details have been previously published.[120] An overview of the main components of the 5.3.2 beamline is shown in Figure 2.14. The X-rays are produced by a bend magnet within the ALS synchrotron storage ring, providing ~10^7 photons/s at 250-700 eV ($\lambda = 5.0$ nm to 1.8 nm). The photon energy is selected by a monochromator and the X-rays are focused by a 25 nm outer radius Fresnel zone-plate through an order sorting aperture (OSA) to remove higher order light, resulting in an ~30 nm FWHM beam diameter on the sample. The sample is raster scanned through the beam focus as the transmitted X-ray flux is detected by a phosphor-coated Lucite "light pipe" followed by a photomultiplier tube (PMT). Figure 2.15 shows images of the various components of the 5.3.2 STXM. More detail is given below for select components of critical importance for these experiments, in the order they are encountered along the beam path.

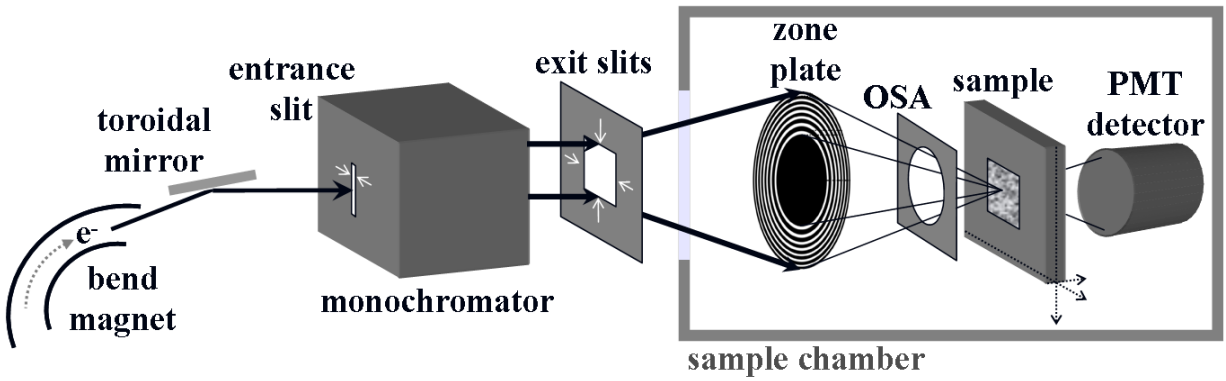

Figure 2.14 Overview schematic of 5.3.2 STXM.

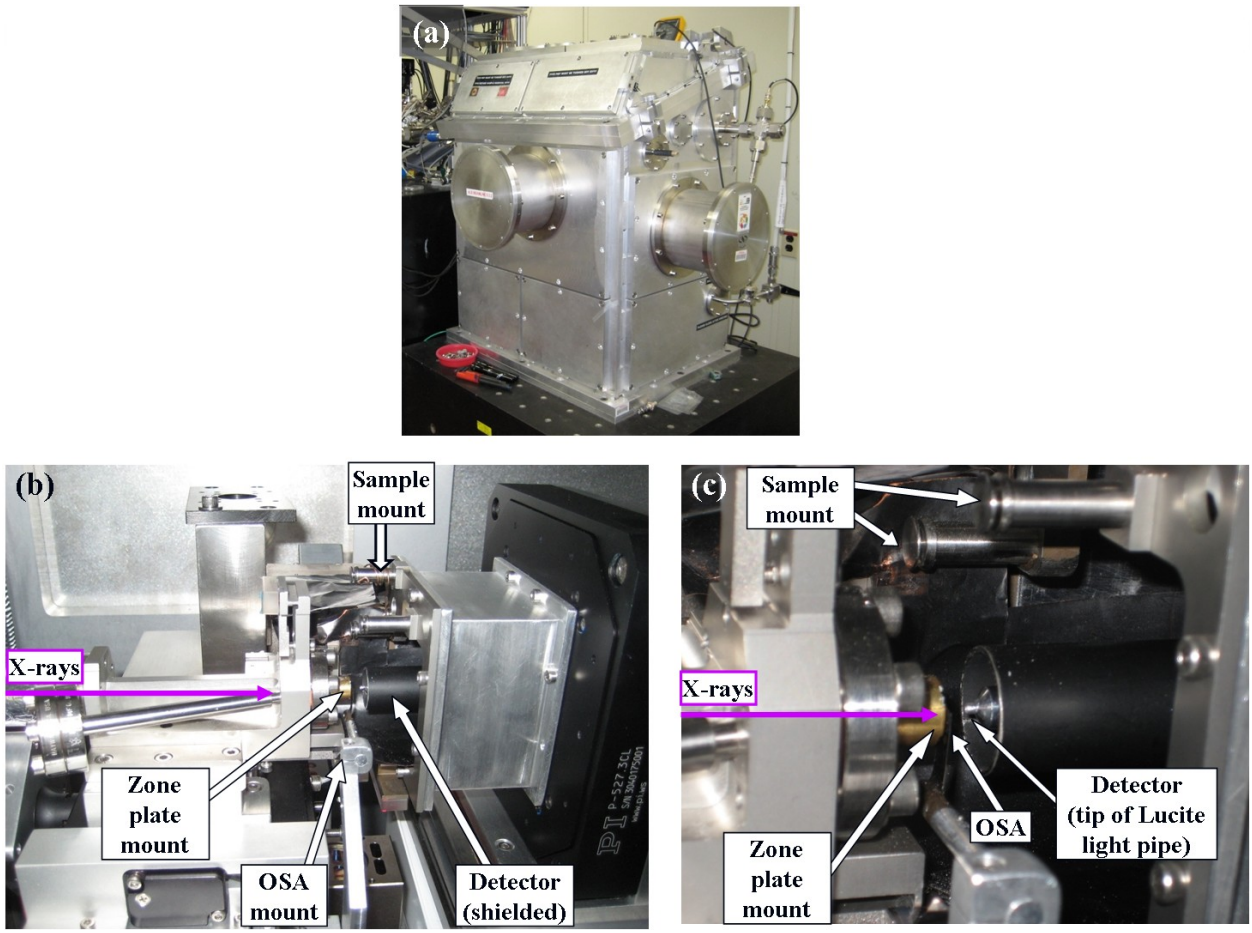

Figure 2.15 Photographs of STXM 5.3.2. (a) Microscope vacuum chamber. (b) Microscope components. (c) Close up of area where the sample holder (Figure 2.17) is mounted directly in front of the phosphor-coated tip of the Lucite light pipe.

The monochromator has three slits: an entrance slit, a dispersive exit slit and a non-dispersive exit slit, allowing for control of the spatial and spectral resolution and photon flux. Table 2.2 provides a summary of how the microscope imaging resolution depends on the various slit widths for a 45 nm outer radius zone plate. However, a newer, higher resolution zone plate is

used for the experiments in this thesis, with a 25 nm outermost zone radius, giving a spatial resolution of 30 nm to 50 nm depending on the slit widths used (versus 50 to 60 nm resolution for the 45 nm outer radius zone plate), but the general trends in flux and resolution with changing slit size in Table 2.2 are still applicable.

Slit Widths (μm)			Energy Resolution (meV)	Spatial resolution (nm)	Flux at 320 eV (MHz)
Entrance	Exit Dispersive	Exit Non-dispersive			
25	**10**	**35**	**75**	**50**	**0.22**
40	**25**	**35**	**100**	**50**	**1.40**
50	**30**	**35**	**125**	**50**	**1.80**
60	**35**	**35**	**150**	**50**	**2.15**
75	**35**	**35**	**175**	**50**	**2.70**
90	**35**	**35**	**200**	**50**	**3.20**
25	**10**	**60**	**75**	**60**	**0.42**
40	**25**	**60**	**10**	**60**	**2.55**
50	**30**	**60**	**125**	**60**	**3.95**
60	**35**	**60**	**150**	**60**	**4.50**
70	**40**	**60**	**175**	**60**	**5.30**
90	**45**	**60**	**200**	**60**	**6.85**

Table 2.2 Trade-off of monochromator slit widths with flux and resolution for a 45 nm outer radius zone plate. This set of parameters has not yet been determined for the 25 nm zone plate.

The X-ray zone plate is a circular diffraction grating with variable line spacing, shown schematically in Figure 2.16(a). The zone plates used at the 5.3.2 STXM consist of gold zones, opaque to the X-rays, on a thin, relatively transparent silicon nitride membrane support. The spatial resolution is limited by the spacing of the outermost zones of the zone plate, called the outermost zone radius, Δr, according to the Rayleigh resolution criterion:

$$\Delta r_{Rayleigh} = \frac{0.610\lambda}{NA} \tag{2.35}$$

where $\Delta r_{Rayleigh}$ is defined as the minimum separation necessary to resolve two point sources, based on their Airy disk patterns, and the NA is the numerical aperture of an objective lens, approximated for small NA as:

$$NA \approx \frac{\lambda}{2\Delta r} \tag{2.36}$$

Putting this back into equation 2.35 gives:[4]

$$\Delta r_{Rayleigh} \approx 1.22\Delta r\,. \tag{2.37}$$

Thus for the zone plate used here with $\Delta r = 25$ nm, the spatial resolution limit is approximately 30.5 nm. In addition to the tightly focused light useful for microscopy, the zone plate also transmits the zero-order (undiffracted) light with reduced intensity and produces higher diffraction orders, which must be blocked by an order sorting aperture (OSA) in order to achieve high spatial resolution imaging, as shown in Figure 2.16(b). The xy position of the OSA is centered with the central stop of the zone plate prior to each set of measurements, and the coarse sample z-stage is used to position the sample about 200 μm behind the OSA. The detector is positioned with respect to the beam with x, y and z stages as well and consists of a phosphor-coated Lucite "light pipe" in front of a photomultiplier tube (PMT); the PMT is surrounded by a

mu-metal shield, which is extended over the light pipe to protect it from stray light (see Figure 2.15(c)).[120]

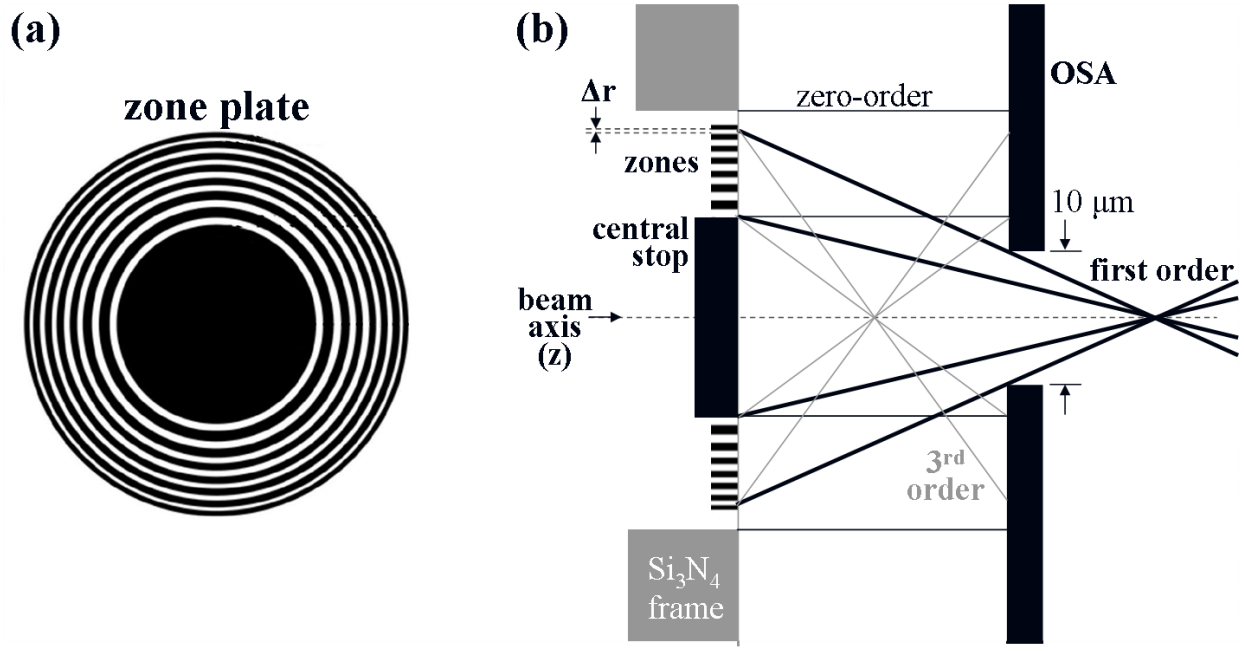

Figure 2.16 Schematic of zone plate (a) front view and (b) side view, showing OSA and position of focus for different diffraction orders. The first order focus is used for STXM imaging, with the sample positioned perpendicular to the beam axis and precisely at the focus.

The position of the zone plate is fixed in x and y with respect to the incoming X-ray beam, but the zone plate-to-sample distance is finely controlled by translating the zone plate along the z axis (beam axis) with a small, high-precision, crossed-roller-bearing stage.[120] The focal length, *f*, of the zone plate is defined as the distance from the zone plate to the first order focus, which is proportional to the wavelength of the light (photon energy). The focal length is given by:

$$f = \frac{D\Delta r}{\lambda} \tag{2.38}$$

where D is the outer diameter of the zone plate.[4, 120] The microscope focus must be adjusted whenever the energy is changed, as in acquiring NEXAFS spectra or taking images at different energies. For example, for oxygen K-edge measurements at 540 eV (λ = 2.3 nm) with Δr=25 nm and D=155 μm, the focal length is ~1.685 mm. The depth of focus of the X-ray beam, Δz, is defined as the region of displacement along the beam axis from the focus within which the on-axis intensity decreases by only 20%:[4]

$$\Delta z = \pm \frac{\lambda}{2(NA)^2} \tag{2.39}$$

For example, at 540 eV the 5.3.2 STXM has NA ~0.046 and the depth of focus is ± 543.5 nm. This is essentially the distance over which the tight focus is maintained; when the sample is positioned at this distance Δz (e.g. ~543.5 nm) "out of focus," the spot size of the beam is only larger by about 8%. For this example, a beam with a 30.5 nm FWHM at the focus expands to ~33 nm at a distance Δz from the focus; for a 50 nm FWHM focused beam, the FWHM is

~54 nm at Δz. This beam size at different sample depths is very important for X-ray patterning of ~500 nm thick HSQ films, as the size of the X-ray beam on the sample determines the pattern resolution (defined as the minimum possible width for a single-pass line exposure, explained further in section 5.2).

To transmit some of the X-rays, HSQ samples must be very thin; for the experiments in this work, HSQ films of 100-500 nm thickness are spin-cast directly onto 100 nm thick silicon nitride membrane "windows." More details on HSQ film preparation and characteristics are presented with experimental results in section 5.2. The commercially available 1 mm × 1 mm, 100 nm thick Si_3N_4 membrane window (Silson Limited) is produced by back-etching into a 5 mm × 5 mm, 500 μm thick frame, which is shown close up in Figures 2.17(a) and (b). After coating with HSQ films, the substrates are fixed to a sample holder plate with double-sided tape as shown in Figure 2.17(c). The sample holder consists of two rows of ~3 mm diameter holes through which the X-ray flux is measured, and each membrane window is thus positioned over one of these holes. The tape covering these clearance holes is removed prior to sample mounting.

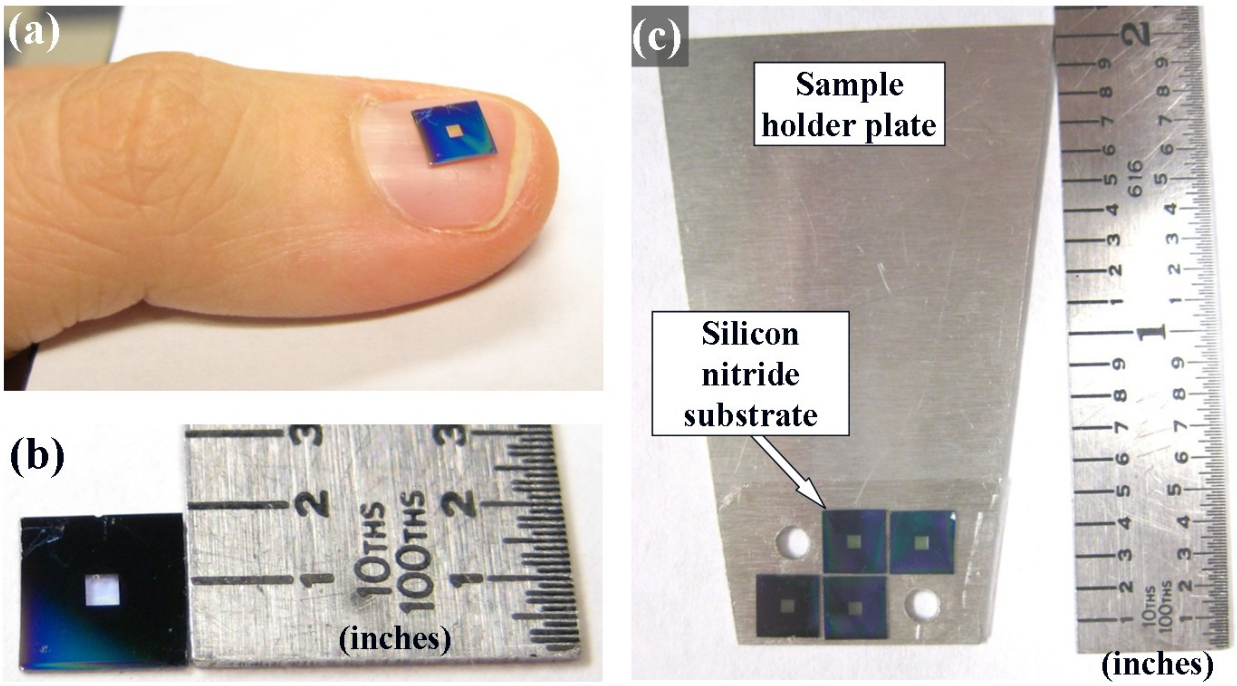

Figure 2.17 Two views, (a) and (b), of the silicon nitride substrate, a 5x5 mm, 525 μm thick frame with 1x1 mm, 100 nm thick membrane window at center, coated with HSQ thin film. (c) Substrates taped to the sample holder plate for the 5.3.2 STXM.

To position the sample in the X-ray beam, the transmission is measured as the sample is scanned in x and y (perpendicular to beam axis) with a coarse stepper motor (range 200 μm to 1 mm). When a smaller, well defined region of interest is chosen, the sample fine motion (range < 200 μm) is controlled by an xy piezo stage. Several different STXM data acquisition modes are used in this work, controlled by a LabView program with a graphical user interface, detailed in section 5.2. To focus the X-rays on the sample, the zone plate-to-sample distance is adjusted to the proper focal length for the precise energy and sample position using a semi-automated focus scan routine. An "overview" image is taken of an area of interest with an opaque feature,

such as the edge of the silicon nitride window or a gold nanoparticle. When the feature is in focus it will have sharp edges in the image; otherwise, it will be blurry, and the sample to zone-plate distance must be adjusted. A one-dimensional line scan (along x-axis) is defined by the user across the feature of interest, as shown in Figure 2.18(a) for focusing across a 100 nm diameter gold nanoparticle. The STXM software then scans the sample through the beam along this line repeatedly as the zone plate-to-sample distance is adjusted slightly for each subsequent scan, as shown in Figure 2.18(b); note how the particle is not visible when this focal distance is off by more than 5 μm. The range of the zone plate along the z-axis during the focus scan is defined by the user (typically ~10 to 100 μm range); if the proper focal length is within the scan range, then at some point during the scan the feature will be in focus, indicated by the black arrows in Figure 2.18(b), and the zone plate is subsequently fixed at this position. The tightest focus is possible when the features used have a thickness less than the depth of focus of the beam (equation 2.41); 100 nm gold particles are ideal for this purpose, and more detail about their use is given in section 5.2. Typically, for HSQ thin film studies, a rough focus scan with a large z-axis range (e.g. 100 μm) is followed by a smaller range scan (e.g. 10 μm) to focus the beam to within ± 500 nm of the film surface, which is within the beam depth of focus. The zone plate position is adjusted automatically by the instrument when switching to a different photon energy near the same absorption edge. However, when moving to a new region of the sample or changing energies by more than ~100 eV, the focus scan is repeated to ensure that tight focusing is maintained.

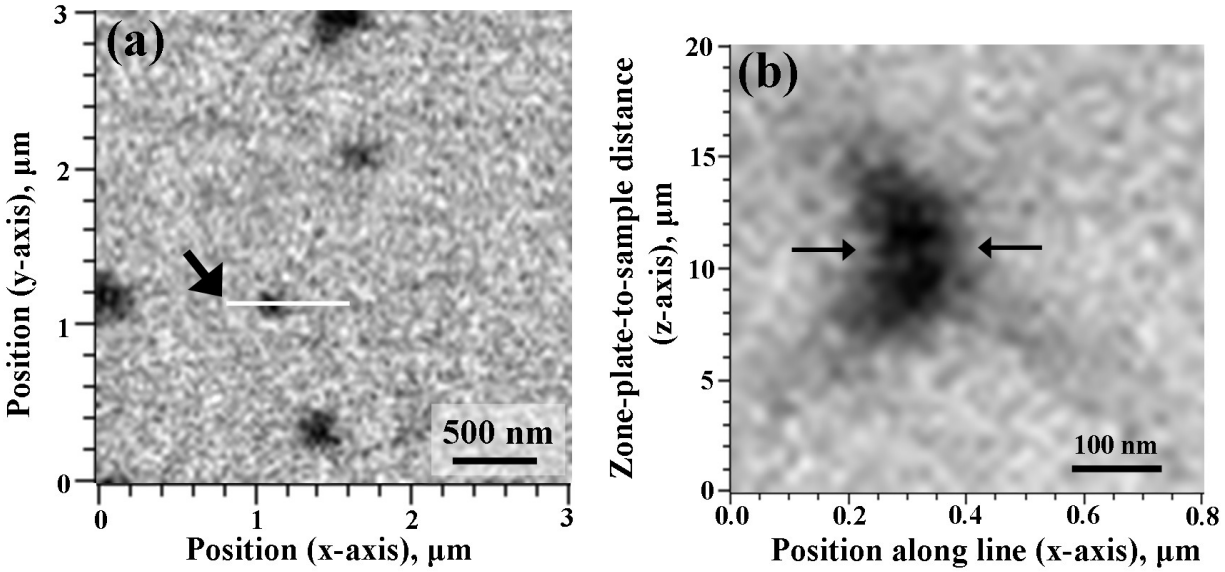

Figure 2.18 Example STXM focus scan. (a) Nearly focused image (550 eV) of 100 nm Au nanoparticles and clusters on HSQ film surface. Bold black arrow points to position of 1D line scan (white line, drawn in). (b) Resulting focus scan across 1D line as zone-plate-to-sample distance is varied. Black arrows indicate the relative zone-plate-to-sample distance for optimal focusing.

3 Observing multiphoton cross-linking of HSQ with broadband CARS

This chapter is based on the following publication:
Caster, A.G.; Kowarik, S.; Schwartzberg, A.M.; Nicolet, O.; Lim, S.H.; and Leone, S.R..
Observing hydrogen silsesquioxane cross-linking with broadband CARS. *J. Raman Spectrosc.* **2009**, *40*, 770.

Broadband CARS microscopy is used for real-time measurements of *in situ* cross-linking of HSQ photoresist films. Using films baked at different temperatures, and therefore cross-linked to varying degrees, characteristic Raman bands are identified for the open "cage" structure and cross-linked "network" structure. The first reported multiphoton initiated cross-linking of HSQ is induced by absorption of high intensity near IR laser light (~10^{12} W/cm^2 peak power). The sub-second time resolution of broadband CARS is used to follow the laser-induced reaction in real time by monitoring the characteristic Raman bands, revealing two-stage first order cross-linking kinetics.

3.1 Introduction: Near infrared multiphoton absorption polymerization of HSQ

After the e-beam sensitivity of HSQ was first discovered in 1998, researchers noticed that the areas outside of the e-beam exposed region that were exposed to background electromagnetic radiation within the e-beam exposure column also became slightly cross-linked.[43] Since then, multiple studies have examined and utilized the sensitivity of HSQ to photons from soft X-rays (1-2 nm) to the EUV (13.4 nm) and UV (157 nm).[41-43, 53-55, 84-85, 121] While previous works show that cross-linking of HSQ can be induced by absorption of photons up to a wavelength of about 157 nm (7.9 eV per photon), above that wavelength HSQ reportedly exhibited no cross-linking sensitivity.[43] However, several other polymer resists that only absorb at wavelengths in the UV and below have recently been utilized for multiphoton absorption polymerization (MAP) using visible and near infrared (NIR) laser sources, and the multiphoton nature of the process leads to a decrease in the size of features that can be patterned far beyond the diffraction limit.[61, 65, 122-125]

To investigate the possibility of multiphoton lithography in HSQ, an HSQ thin film is placed in the CARS microscope described in section 2.2.1, at the focus of the ultrafast pulsed NIR beam, and MAP is observed in HSQ for the first time. To understand the process in detail, the cross-linking progress is monitored in real time by following the changes in the CARS peaks that correspond to the cage and network structures. Comparison to CARS and spontaneous Raman spectra of thermally cross-linked films confirms that the spectral changes are in fact due to HSQ cross-linking. By taking spectra in 500 ms intervals during the NIR multiphoton induced reaction, the initial, fast kinetics are accessible, suggesting a two-stage, first-order cross-linking mechanism.

3.2 Sample preparation and experimental setup

HSQ films are prepared from a flowable oxide solution (FOx-25®, DOW Corning, 15-40 wt% HSQ in a volatile methyl siloxane solvent). Thin films are produced by spin-coating 120 μL of the solution onto glass microscope coverslips at 800 RPM for 30 seconds, yielding films of approximately 1 - 1.2 μm in thickness, as measured with profilometry. Films are cured on a hot plate in air for 10 min at 150 ºC to evolve any remaining solvent. Measurements are performed in air, but all samples are stored under high nitrogen flow when not being measured. For temperature dependent measurements, samples are baked for 10.0 ± 0.5 min at 150 °C, 250 °C, 300 °C, 350 °C and 450 °C (all temperatures are ±15 ºC). The broadband CARS setup detailed in section 2.2 (Figure 2.3) is used to expose and obtain spectra of the thin films. For these experiments, a probe centered at 759 nm with a width of ~1 nm is employed, corresponding to a spectral resolution of about 17 cm^{-1}. The light is focused on the sample through a 1.2 NA water-immersion objective (60x UPlanApo, Olympus), and the signal is collected through a 0.85 NA air objective or 1.0 NA water objective. Homodyne-amplified CARS spectra are collected with a spectral range of ~250 to 1200 cm^{-1}, and the region from 300-650 cm^{-1} is analyzed to monitor the changing HSQ bands during cross-linking.

Prior to taking spectra, the spectral phase is compressed with the appropriate phase mask on the SLM, as discussed in section 2.2.2. The average beam power is 46 mW before the microscope, focused to a diffraction limited spot of ~400 nm diameter, and the transform-limited, shortest possible pulse duration with the measured laser bandwidth is ~15 fs. This corresponds to an approximate peak intensity of 2.7×10^{13} W/cm^2 if the full power reaches the focus. However, the mirror and microscope objective also reduce the average power by ~50%, and autocorrelation measurements reveal that pulse compression before the microscope (2^{nd} order spectral phase, only) results in a pulse duration of ~38 fs. Using MIIPS for pulse compression at the microscope focus, the pulse duration is likely similar or slightly longer, resulting in an approximate peak intensity of $\leq 5.4 \times 10^{12}$ W/cm^2 at the microscope focus within the sample.

Spontaneous Raman spectra of the unbaked and baked HSQ thin films are measured in a home-built microscope with a 10 mW, 633 nm HeNe laser source and 100x, 0.95 NA air objective. The spectra shown later, in Figure 3.5, are acquired with a more sensitive state-of-the-art commercial Raman microscope (alpha500, Witec) with a 532 nm laser (38 mW) also focused through a 100x, 0.95 NA objective (Nikon), and the signal is collected back through the same objective. Raman depolarization spectra are measured on this microscope by placing a polarization filter in the beam collection path, which is oriented to transmit the scattered light polarized either parallel or perpendicular to the input laser polarization.

3.3 Measuring real-time cross-linking kinetics

Figure 3.1(a) shows CARS spectra for HSQ films baked for 10 minutes at temperatures of 150 °C, 250 °C, 300 °C, and 450 °C. Clear spectral changes are visible with increasing baking temperature, demonstrating the chemical sensitivity of CARS with respect to the HSQ microstructure. The film baked at 150 °C corresponds primarily to the nominal cage structure, as established in previous studies of thermal curing of HSQ, which show that the HSQ cages cross-link to the network structure only upon heating above 190 ºC.[36, 126] With increasing baking temperature, and therefore increased cross-linking, Raman bands at 342 cm^{-1}, 454 cm^{-1}, and

562 cm^{-1} disappear, while a band characteristic of the network structure grows in at 484 cm^{-1}. In order to identify the Raman bands in the cage and cross-linked HSQ, Raman spectra are measured for films baked at 150 ºC as well as 350 ºC for 10 min, shown in Figure 3.2. The acquisition time for each of these spontaneous Raman spectra was 60 seconds. Comparison of the CARS spectra in Figure 3.1(a) to spontaneous Raman spectra in Figure 3.2 demonstrates very good agreement of peak positions and lineshapes in the region from 300-650 cm^{-1} (although the CARS wavenumber calibration is likely ~12 cm^{-1} too low), showing that the homodyne-amplified CARS spectra are equivalent to the spontaneous Raman spectra within this range. (However, outside of the 300-650 cm^{-1} range, there are significant differences between the DQSI-CARS and spontaneous Raman spectra, which are explored in detail in section 3.4.) Furthermore, the comparison demonstrates the higher sensitivity of the broadband CARS, which requires integration times of only 1 s for the spectra in Figure 3.1(a), as opposed to 60 seconds for the spontaneous Raman with comparable signal-to-noise ratios in Figure 3.2. (The more sensitive commercial Raman microscope can achieve similar signal-to-noise in ~30 s, shown in the following section (Figure 3.5).)

In a second set of experiments, CARS spectra are obtained in 50 ms intervals as the HSQ film remains in the beam focus, in order to study the kinetics of near IR cross-linking, as shown in Figure 3.1(b). In contrast to curing the films at different temperatures for Figure 3.1(a), the changes in Figure 3.1(b) are induced by focusing the near IR beam into a diffraction limited volume, with an approximate peak intensity of $5x10^{12}$ W/cm^2, as noted above. For improved signal-to-noise, the spectra shown in Figure 3.1(b) are the average of 10 spectra (50 ms each, total 500 ms acquisition time) which is still fast compared to the timescales of cross-linking. With increasing near IR exposure time, spectral changes occur similar to those observed upon baking of the HSQ films, demonstrating that absorption of the intense NIR light does induce HSQ cross-linking, although possibly by a different mechanism.

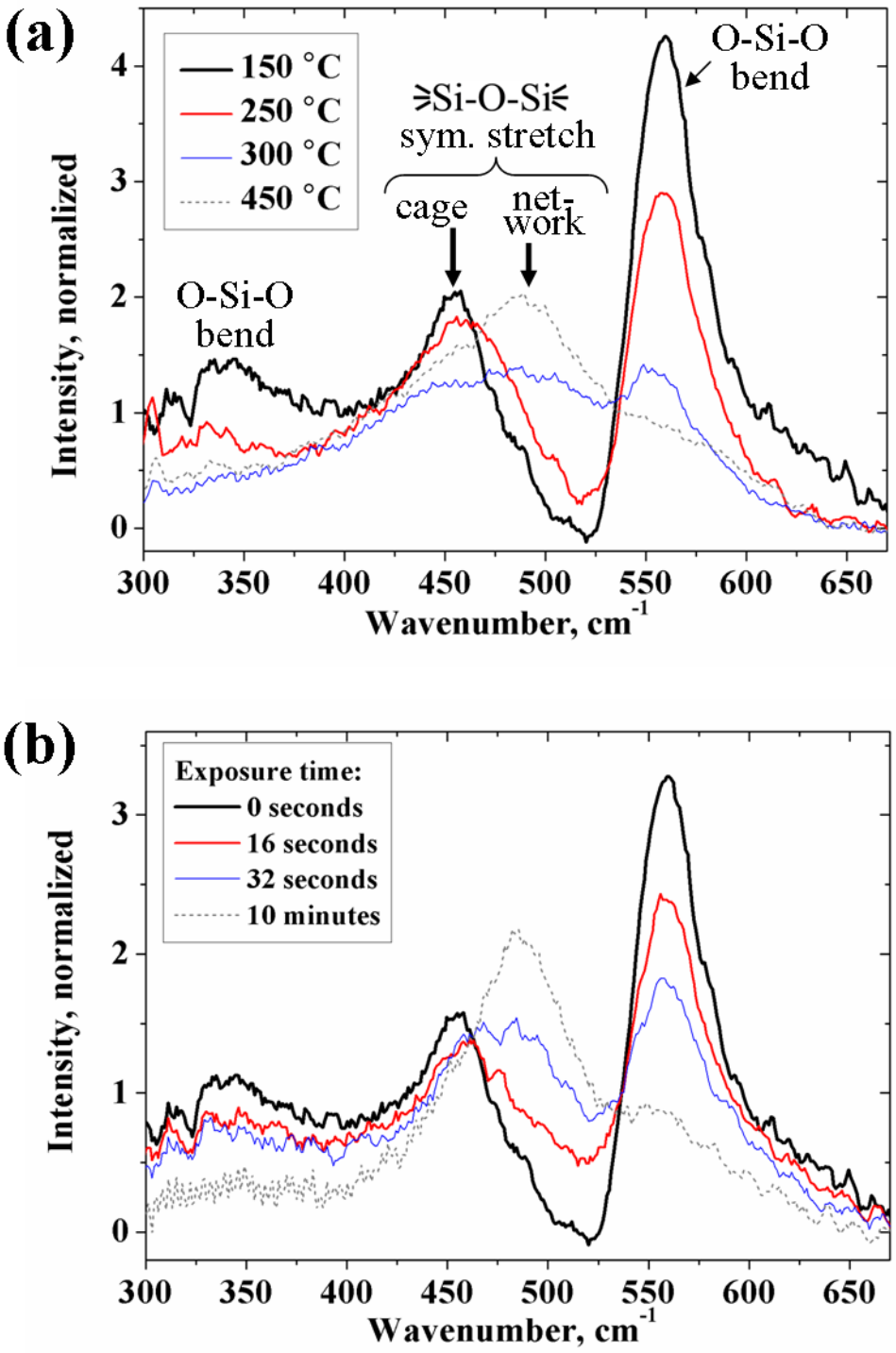

Figure 3.1 DQSI CARS spectra of HSQ thin films. (a) Temperature dependence of cross-linking. (b) Real-time monitoring of cross-linking in focused, pulsed near IR laser beam.

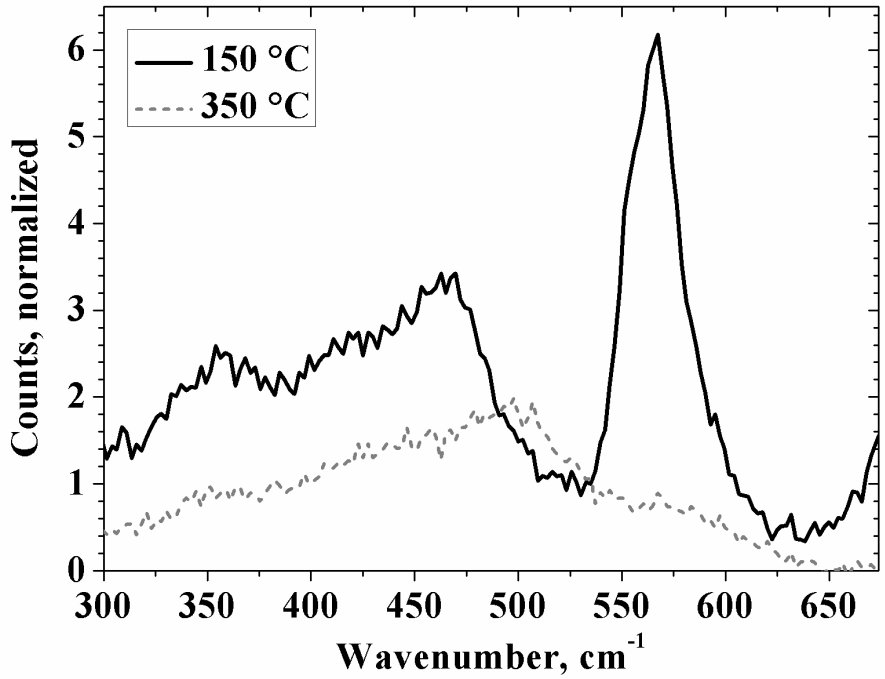

Figure 3.2 Spontaneous Raman spectra of HSQ thin films baked for 10 minutes at 150 °C or 350 °C.

A clear isosbestic point at 535 cm^{-1} in Figure 3.1(b) suggests the loss of one species and the growth of another. The thermally cross-linked spectra (Figure 3.1(a) and Figure 3.2) are obtained from different (identical) films, but are likewise normalized from 0 to 1 at 535 cm^{-1}. By comparing the spectra in Figure 3.1(a) and (b), one sees that the amount of conversion to the network structure after 10 minutes of near IR exposure is greater than for the sample heated to 300 ºC for 10 minutes. Since it has been reported that HSQ does not have any direct sensitivity to cross-linking under near IR exposure,[43] multiphoton absorption and heating in the focus of the intense beam are considered as two possible conversion mechanisms. At the powers used, some heating of the sample is expected in the beam focus, but note that a temperature of at least 190 °C must be reached to initiate significant bond redistribution in HSQ.[11] To determine if heating is the primary mechanism, the cross-linking rate is measured again using a water immersion collection objective. If heating plays a significant role in the cross-linking, water is expected to slow the cross-linking by better thermal removal of the heat, thus resulting in a lower temperature within the focal volume. However, it is observed that when water is in contact with the sample during exposure, the cross-linking rate does not change. Furthermore, it is observed that when the average laser power is reduced by half, the rate for the initial stage of cross-linking decreased by approximately a factor of ten. This implies a strongly non-linear process, suggesting that the primary cross-linking mechanism in the laser focus is MAP, which will be explored in more detail in Chapter 4.

The peaks in the CARS spectra of non-cross-linked (cage) HSQ can be assigned based on observations and calculations reported by Bornhauser and Calzaferri.[127] However, previous Raman assignments for cross-linked (network) HSQ thin films are not available. Furthermore, all previously reported Raman studies were performed on pure (powdered) HSQ solids rather than the thin films, which have slightly different characteristics. For the non-cross-linked HSQ films, the 342 cm^{-1} and 562 cm^{-1} peaks are assigned to O-Si-O bends, compared to spontaneous

Raman spectroscopy values of 341 cm^{-1} and 576 cm^{-1} (calculated).[127] The 454 cm^{-1} peak is assigned to the ⋗Si-O-Si⋖ symmetric stretch, compared to 446 cm^{-1} (calc.).[127] The three bond symbol, ⋙, represents all the other cage-like or network-like bonds to the silicon atom.

After 10 minutes of near IR exposure, the O-Si-O bend peaks at 342 cm^{-1} and 562 cm^{-1} decrease to about 25 % of their original intensity, as does the ⋗Si-O-Si⋖ symmetric stretch at 454 cm^{-1}, while a new peak at 484 cm^{-1} emerges. As the HSQ cages cross-link, the structure becomes more and more like that of SiO_2 ($SiO_{4/2}$), as ⋗Si-O-Si⋖ bonds replace ⋗Si-H bonds.[35] The loss of the O-Si-O bending peaks is attributed to the change of the cage O-Si-O bonds, with an angle of approximately 109.5º,[127] to the network O-Si-O bonds, which are possibly more linear and rigid compared to the cage bonds. The 484 cm^{-1} peak is tentatively assigned to a ⋗Si-O-Si⋖ symmetric stretch after cross-linking, as FTIR spectra show that the ⋗Si-O-Si⋖ stretch grows in as the network structure forms,[35] and there is a known IR active ⋗Si-O-Si⋖ symmetric stretch for cage HSQ at 481 cm^{-1},[127] which may become Raman active in the network structure due to changes in symmetry. Furthermore, an increased rigidity of ⋗Si-O-Si⋖ bonds in the network structure can explain the increase of the stretching wavenumber from 454 cm^{-1}. This increasing rigidity can be pictured using a physical model of the monomer cage, which is free to stretch and compress in almost any direction, while the cross-linked cages become more fixed in their positions as they form more bonds to other cages and the existing network. Also, the 484 cm^{-1} peak is substantially more broad (FWHM 61 cm^{-1}) than the initial 454 cm^{-1} peak (FWHM 30 cm^{-1}), which may be due to the fact that network O-Si-O bonds have a variety of possible angles and bond lengths (including some remaining cage-like bonds) at different cross-linked sites,[35] leading to inhomogeneous broadening of the spectral linewidth.

For a more detailed analysis of the kinetics of cross linking, the peaks in the spectra in Figure 3.1(b) are fit to a Gaussian profile to determine the area of the 454 cm^{-1}, 484 cm^{-1}, and 562 cm^{-1} CARS bands. Figure 3.3 shows the decay of the 562 cm^{-1} peak (O-Si-O bend) characteristic of the cage structure, and the rise of the peak at 484 cm^{-1} (⋗Si-O-Si⋖ symmetric stretch) characteristic of the network structure, from 0 to 10 minutes. The data is best fit by a double exponential decay, with a fast initial time constant (decay lifetime, τ_1) of 24.4 ± 1.3 seconds for the decay of the O-Si-O bend and the increase of the network ⋗Si-O-Si⋖ stretch, demonstrating a direct conversion from cage to network structure without long lasting intermediate species. The second stage of the HSQ cross-linking kinetics occurs on a much slower timescale for which the fit gives different constants (τ_2) of 221 ± 16 seconds for the decay and 123 ± 11 seconds for the growth, with the difference probably due to fit uncertainties and neglecting inhomogeneous broadening. The decay lifetime, τ, for each stage is defined as the time at which 1/e (37%) of the cage-like peak area remains. This data set was reproduced on different days with several different HSQ thin film samples, with time constants for the initial, fast regime ranging between 10 seconds and 30 seconds. The variability in the experiment is most likely due to variations in the film thickness and, more critical, differences in laser peak intensity due to incomplete chirp compression, which will be discussed in more detail in section 4.3.

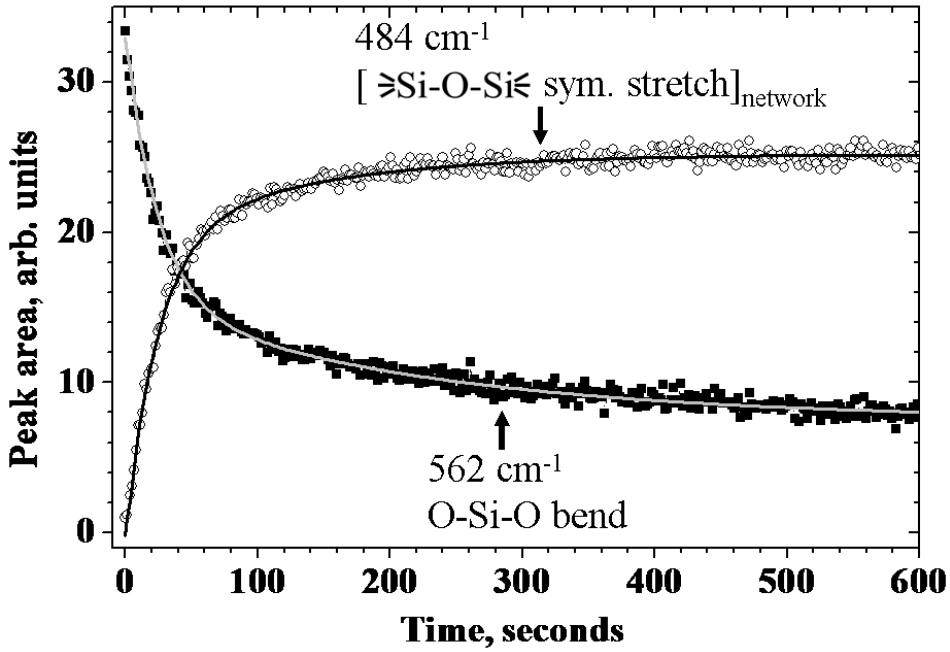

Figure 3.3 Decay of the 562 cm^{-1} peak area (cage-like O-Si-O bend) with time in the focused near IR beam, and growth of the 484 cm^{-1} band (network-like ⩾Si-O-Si⩽ symmetric stretch). Solid lines are double exponential decay fit. Both the decay and growth kinetics exhibit a fast first stage with a time constant of ~24 s and a much slower second stage.

Zero, first and second order kinetics were considered for each stage of the measurements in Figure 3.3 and several similar measurements, and two-stage, first order kinetics (in the rate limiting step) best explains the double exponential decay curves. In previously reported photoinduced polymerization reactions, first-order kinetics were also observed, which was expected when a fixed concentration of photoinitiator molecules is initially present.[128] In HSQ, cross-linking may proceed by the network conversion of a limited number of reactive sites in the as-spun film (prior to exposure), where the atoms have approximately the optimal relative orientation and juxtaposition for network formation. The two first-order stages of cross-linking with exposure time (at constant laser power) can then be explained if there is an initial concentration of easily cross-linked sites, which react quickly, leaving a only some less favorable reaction sites that result in the much slower, second stage of the reaction, possibly by a slightly different mechanism. This two-stage cross-linking kinetics of HSQ has also been observed in multiple experiments in our laboratories by using X-ray induced cross-linking and X-ray spectroscopic detection, which will be discussed in detail in Chapter 5.

Different cross-linking mechanisms have been proposed for e-beam and thermally induced cross-linking of HSQ, but the end result of each mechanism is an increase in the ⩾Si-O to ⩾Si-H ratio of the exposed or heated film. For thermally-induced cross-linking of HSQ above the onset of curing at ~190º C,[36, 126, 129] redistribution of the network leading ultimately to $SiO_{4/2}$ bond formation and evolution of silane gas (SiH_4) is the primary mechanism proposed for curing from ~250-350 ºC. Remaining ⩾Si-H bonds within the network structure create the porosity that gives the network HSQ its low dielectric constant. Two-stage, zero-order kinetics[58] have previously been proposed for the low temperature reaction (250-350 ºC). In that work, the

intensity of two characteristic FTIR peaks were measured as a function of HSQ film baking temperature and time, so the time resolution of the measurements was limited to ~1 to 2 minutes, based on the heating and cooling times of the film. However, appreciable cross-linking apparently took place within the first minute of heating, and the linear (zero-order) fits do not match the data well, so it appears that with higher time resolution their data may also fit a single or double exponential (sub-linear) function, as observed in these studies.

From 350-435 ºC, thermally induced bond dissociation, especially ≡Si-H bond cleavage, increases the reaction rate. Direct ≡Si-H bond cleavage is also expected for e-beam exposure, and either mechanism (thermal or e-beam) is followed by the linking of two intact cages via reaction with O_2 or H_2O, incorporating one additional oxygen atom into the network for every cross-linking event. It was previously found that about 400 °C is the optimal temperature for thermal curing of HSQ for use as an ILD for integrated circuits, giving the best balance of mechanical stability and low dielectric constant.[130] Above 435º C, the ≡Si-H dissociation rate increases rapidly, breaking the remaining cage-like bonds, leading to the collapse of the porous network structure. The results presented here suggest that the ultrafast NIR induced cross-linking occurs via a photolytic and not thermal mechanism, and the double exponential decay observed during NIR exposure suggests a two-stage first order mechanism for the cross-linking. The possible reaction mechanisms are explored in detail in Chapter 4 as they relate to the reaction order and multiphoton absorption power dependence.

3.4 Spontaneous Raman spectra and depolarization ratios of HSQ thin films

For the real-time kinetics measurements, only the region from 300-650 cm^{-1} is used (Figure 3.1), but the full (unexposed) DQSI-CARS spectrum from 250-1200 cm^{-1} is shown in Figure 3.4(a). At frequencies higher than 650 cm^{-1}, significant differences are found between this spectrum and the full spontaneous Raman spectrum, shown in Figure 3.4(b). Most puzzling is the absence of several strong Raman lines in the DQSI-CARS spectrum, even though for other samples, such as toluene, PMMA and PS (Figure 2.6(a) and (b)), many strong CARS peaks are visible all the way out to 1200 cm^{-1}. The differences between the strongest peaks in the DQSI-CARS and spontaneous Raman spectra shows that the DQSI-CARS wavenumber calibration is likely too low by ~12 cm^{-1} in this case.

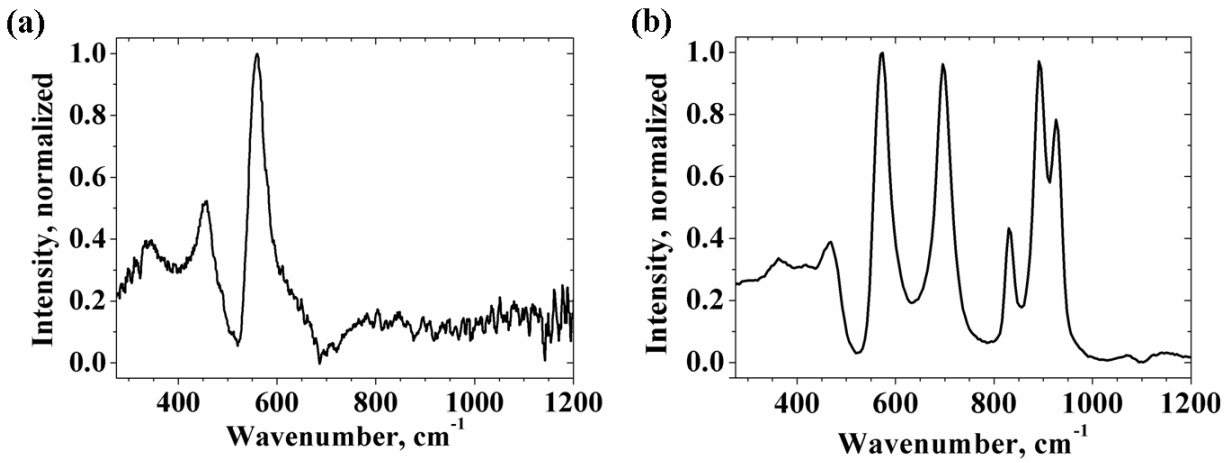

Figure 3.4 (a) Full DQSI CARS spectrum, 0.5 s acquisition time and (b) Raman spectrum over the same spectral range, 50 seconds acquisition time.

Some answers about the missing peaks lie in the depolarized Raman spectrum in Figure 3.5(a), where similar differences in peak intensity are seen between the Raman scattering polarized parallel versus perpendicular to the incident laser polarization. The upper curve in Figure 3.5(a) (black curve) shows the spontaneous Raman spectrum from 0 to 1200 cm^{-1} with all polarizations of scattered light detected, while the lower curves are acquired by placing a polarizer after the microscope but before the spectrometer, transmitting only the scattered light that is parallel (polarized, red curve) or perpendicular (depolarized, blue curve) to the laser polarization. Notably, the strong 574 cm^{-1} and 467 cm^{-1} peaks in the polarized spectrum, which are also the peaks used for the CARS kinetics measurements (at 562 and 484 cm^{-1}), are almost totally extinguished in the depolarized spectrum. Furthermore, at 697 cm^{-1} there is a strong peak in the spontaneous Raman spectrum, but possibly a small negative peak in the DQSI-CARS spectrum. Figure 3.5(b) shows the full range of these spontaneous Raman spectra (all polarizations, polarized and depolarized), from 0 to 3800 cm^{-1}. Note that the peaks used for the real-time kinetics measurements are in fact six times weaker than the strongest, Si-H stretching band at 2270 cm^{-1}.

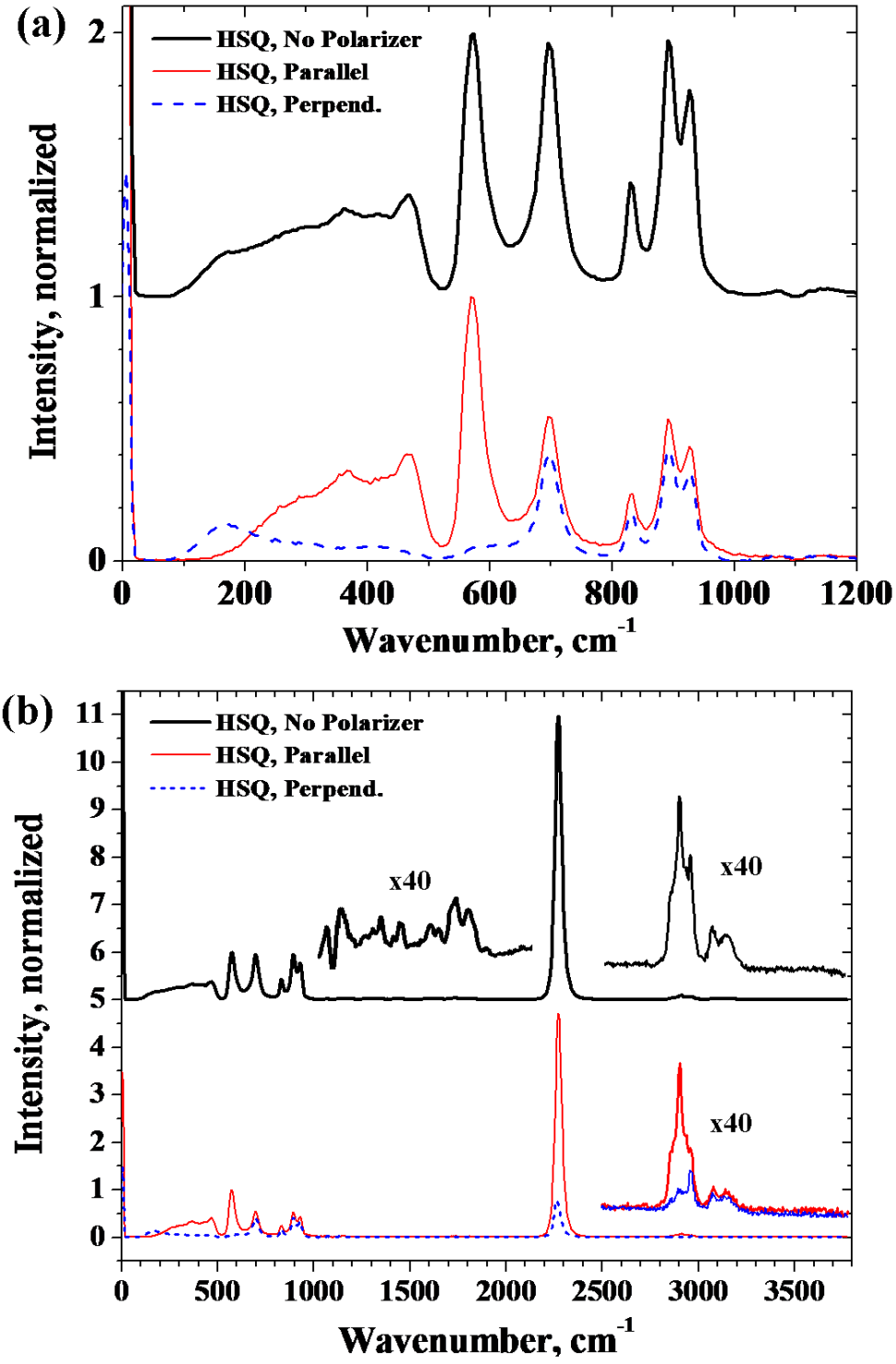

Figure 3.5 Spontaneous Raman spectra of ~1 µm thick HSQ film pre-baked at 150 °C for 10 minute. (a) Region accessible with DQSI CARS, and (b) full spectrum. All scattered polarizations are detected for the upper curves (black), but polarized signal only is detected for the middle curves (red), and the bottom curves (blue) are the depolarized spectra.

The ratio of the depolarized to polarized peak intensity in Raman scattering spectroscopy depends upon the symmetry of each particular vibrational mode. The Raman depolarization ratio for a single vibrational mode is defined as:

$$\rho_d = \frac{I_{perpendicular}}{I_{parallel}} \tag{3.1}$$

where $I_{perpendicular}$ and $I_{parallel}$ are the intensity of the light scattered perpendicular and parallel to the laser polarization, respectively,[86] and the total scattering signal using these definitions is approximately $I_{perpendicular} + I_{parallel}$. Thus, vibrational modes that depolarize the light have a large depolarization ratio, and peaks with a small depolarization ratio are said to be highly polarized. More specifically, the depolarization ratio for totally symmetric vibrational modes is always less than 0.75, and these are called polarized bands, while all other modes should exhibit depolarization ratios of ~0.75, and are thus called depolarized.[86] The 574 cm^{-1} and 467 cm^{-1} bands, assigned to the O-Si-O bend and ⩾Si-O-Si⩽ symmetric stretch, respectively, and the broad (overlapping) bands from 200-400 cm^{-1} are all highly polarized, with depolarization ratios of ≤0.15, and thus are totally symmetric vibrational modes. This is in agreement with the calculated point group for each of these modes; as shown in Table 3.1, the 574 and 467 cm^{-1} bands correspond to normal modes with A_{1g} point group symmetry. The remaining peaks between 574 cm^{-1} and 1200 cm^{-1} all exhibit depolarization ratios of ~0.75, and thus they are not totally symmetric modes. Therefore, it appears that only the totally symmetric modes are observed in the DQSI-CARS spectra.

It is likely that most of depolarized signal is lost in the projection (splitting) and subtraction steps of DQSI-CARS (equations 2.16 and 2.19 and Figure 2.5). For totally symmetric modes, which are highly polarized, most of the resonant CARS signal will be scattered at the same polarization as the probe field, which is assumed for the projection equations (2.16). However, for depolarized modes, 3/4 as much light is scattered perpendicular to the probe polarization; that is to say, ~43% [or $\frac{3}{4}/\left(1+\frac{3}{4}\right)$] of the scattered light is polarized perpendicular and ~57% [or $1/\left(1+\frac{3}{4}\right)$] parallel to the laser polarization. Assuming these depolarization ratios for the non-totally symmetric Raman modes, in the projection step these (non-symmetric) peaks only will not follow equation 2.16, but instead:

$$P_R^i(\omega) = \frac{1}{\sqrt{2}} P_R \qquad \text{and} \qquad P_R^j(\omega) = -\frac{1}{\sqrt{2}}\left(\frac{\frac{1}{4}}{1+\frac{3}{4}}\right) P_R \approx -0.1 P_R \tag{3.2}$$

where P_R is the total resonant CARS signal, given by equation 2.13. Thus, unlike for equations 2.16, the resonant signal in spectrum *j* is no longer equal in magnitude to that in spectrum *i*, and following equations 2.17 through 2.19, the total difference signal for the depolarized (non-symmetric) modes only is:

$$S^i(\omega) - S^j(\omega) \approx \frac{1}{2}\left(\frac{\frac{1}{4}}{1+\frac{3}{4}}\right)\alpha_R |P_{NR}| A(\omega-\omega_{\mathrm{Pr}})\left(\mathrm{Re}[L(\omega)]\cos\phi_{\mathrm{Pr}} - \mathrm{Im}[L(\omega)]\sin\phi_{\mathrm{Pr}}\right) \tag{3.3}$$

Here, the pre-factor in the difference signal is just ~0.07, compared to a value of 2 in equation 2.19, which has proven to be valid only for totally symmetric Raman modes; thus, only ~4% as much signal is collected for depolarized peaks as for polarized ones! Furthermore, there is also a possibility that some signal is lost in the scattering process itself based on the symmetry of the peaks; as the pump and Stokes fields are parallel in polarization, it is feasible that they do not coherently excite the depolarized oscillations as effectively as the polarized ones. However, to fully understand the DQSI-CARS depolarization effect on the scattering intensity will require

theoretical treatment of the third-order nonlinear susceptibility (a fourth-rank tensor) with respect to the polarization of the pump and probe fields and the symmetry of the vibrational modes. Instead, other variations of broadband CARS that use phase-shaping techniques only, such as Fourier-transform spectral interferometry (FTSI) CARS,[131] can be used in the future to circumvent these polarization effects. However, for the HSQ kinetics measurements in this study, the peaks from 300 to 650 cm^{-1} are sufficient to assess the degree of cross-linking.

The Raman and CARS peak values and assignments for the HSQ thin films are summarized in Table 3.1. The previously reported HSQ Raman have all been for powdered, crystalline HSQ, which show some differences in peak positions and intensities from the thin films. This supports earlier reports of structural differences that occur upon spin coating of HSQ, even under vacuum at room temperature,[47, 132] and could also be due to slight chemical differences of the HSQ used in the Dow Corning spin-on solution.

Peak assignments, present work HSQ thin film				**Source of assignment, literature**					
Observed (cm^{-1})		**Type of Vibration (ν=stretch, δ=bend)****	**polarized or depolarized (ratio)**	**Ref. #**	**Type of sample**	**Observed (calculated) (cm^{-1})**	**Raman or IR active (R, IR)**	**Type of Vibration (ν=stretch, δ=bend)**	**Symmetry**
Spont. Raman (relative strength)*	**DQSI-CARS**								
165 (w)	n/a	$\delta(OSiO)_{cage}$	depol (5)	127	HSQ powder	171 (168)	R	δ(OSiO)	T_{2g}
364 (w)	342	$\delta(OSiO)_{cage}$	pol (0.15)	133	HSQ powder	(341)	R	δ(OSiO)	T_{2g}
				127	HSQ powder	399 (397)	IR	δ(OSiO)	T_{1u}
414 (vw)			--	127	HSQ powder	414 (418)	R	δ(OSiO)	T_{2g}
					HSQ powder	423 (423)	R	δ(OSiO)	E_g
467 (m)	454	$\nu_s(SiOSi)_{cage}$	pol (0.07)	127	HSQ powder	446 (456) 456 (456)	R	ν_s(SiOSi)	A_{1g}
--	484	$\nu_s(SiOSi)_{network}$	--	127 133	HSQ powder	468 (468)	IR	ν_s(SiOSi)	T_{1u}
					HSQ powder	465 (481)	IR	ν_s(SiOSi)	T_{1u}
574 (s)	562	$\delta(OSiO)_{cage}$	pol (0.05)	133	HSQ powder	580 (576)	R	δ(OSiO)	A_{1g}
					HSQ powder	610 (613)	R	ν_s(SiOSi)	T_{2g}
697 (s)	NONE	ν_s(SiOSi)	depol (0.75)	127	HSQ powder	697 (691)	R	ν_s(SiOSi)	E_g
833 (m)	NONE	δ(SiOH) ?	depol (0.72)	134	$(CH_3)_3SiOH$ (theory)	(832)	--	δ(SiOH)	
				135	3-aminopropyl-triethoxysilane	840	R		
				136	silica	840			
				137	silica	834	IR		
				30	"T_{14}" $(HSiO_{3/2})_{14}$	830	IR	δ(OSiH) ?	
894 (s)	NONE	δ(OSiH)	depol (0.79)	133	HSQ powder	890 (894)	R	δ(OSiH)	T_{2g}
925 (s)	NONE	δ(OSiH)	depol (0.77)	133	HSQ powder	932 (922)	R	δ(OSiH)	E_g
1067 (vw)	NONE	ν_{as}(SiOSi)	--	133	HSQ powder	1117 (1116)	R	ν_{as}(SiOSi)	T_{2g}
1146 (vw)	NONE	ν_{as}(SiOSi)	--	133	HSQ powder	1141 (1143)	IR	ν_{as}(SiOSi)	T_{1u}
1270 (vw)	n/a	solvent ?	--	138	$Si(OC_2H5)_4$ (*l*)	1295	R		
1306 (vw)	n/a		--						
1350 (vw)	n/a		pol (~0)						

1453 (vw)	n/a	δ(SiOH)	depol (~1)	[139]	uranyl silicates	1453	R	δ(SiOH)	
		$\delta_{as}(CH_3)$ (solvent)		[138]	$Si(OC_2H_5)_4$ (*l*)	1458	R	$\delta_{as}(CH_3)$	
1606 (vw)	n/a	?	depol (~1)						
1652 (vw)	n/a	?	depol (~1)	[138]	silica gel	1635	R		
1736 (vw)	n/a	?	depol (0.87)						
1805 (vw)	n/a	?	depol (0.87)						
1894 (vw)	n/a	solvent ?	pol (~0)	[138]	$Si(OC_2H_5)_4$ (*l*)	1895	IR		
2271 (vs)	n/a	ν(SiH)	pol (0.17)	[133]	HSQ powder	2277 (2381)	IR	ν(SiH)	T_{1u}
				[133]	HSQ powder	2291 (2381)	R	ν(SiH)	T_{2g}
				[133]	HSQ powder	2302 (2381)	R	ν(SiH)	A_{1g}
2865 (vw)	n/a	solvent ?	pol (~0)	[138]	$Si(OC_2H_5)_4$ (*l*)	2870	R		
2908 (w)	n/a	$\nu_s(CH_3)$ (solvent)	pol (0.19)	[134]	$(CH_3)_3SiOH$	2906 (pol)	R	$\nu_s(CH_3)$	
				[135]	3-aminopropyl-triethoxysilane	2887,2929			
2938 (vw)	n/a	solvent ?	pol (~0)	[138]	$Si(OC_2H_5)_4$ (*l*)	2930	R		
2966 (w)	n/a	$\nu_{as}(CH_3)$ (solvent)	depol (0.70)	[134]	$(CH_3)_3SiOH$	2967 (depol)	R	$\nu_{as}(CH_3)$	
				[135]	3-aminopropyl-triethoxysilane	2974			
3079 (vw)	n/a	?	depol (0.84)						
3153 (vw)	n/a	?	depol (0.85)						

*Relative peak strength: vw=very weak, w=weak, m=medium, s=strong and vs=very strong.
**ν_{as}=anti-symmetric stretch, ν_s=symmetric stretch.

Table 3.1 Observed Raman and DQSI-CARS spectrum peaks and peak assignments, with corresponding literature values for similar samples. Peaks highlighted in yellow are used for kinetics analysis in this work.

3.5 Conclusions

With broadband CARS microscopy, cross-linking kinetics are measured in a relatively novel spin-on dielectric and photoresist material, hydrogen silsesquioxane, *in situ* in 500 ms time-intervals. The robust, single beam interferometric method used here to acquire broad Raman equivalent spectra allows for fast measurements that contain a great deal of spectral information. These studies show that substantial HSQ cross-linking occurs within the first minute of focused, pulsed NIR laser exposure, followed by a slower second stage, and proceeds with apparently first-order kinetics. This discovery opens the possibility for direct-write, muliphoton lithography (MAP) in HSQ and related materials with visible and NIR laser sources. The experiments detailed in the following chapter explore the non-linearity of the NIR induced cross-linking, and possible mechanisms to explain the two stage nature of the cross-linking process. X-ray microscopy experiments detailed in Chapter 5 further elucidate the photo-intiated reaction mechanism, also showing that the reaction may follow two-stage first order kinetics, and gives some insight about which species are involved in the two stages of the reaction.

The first spontaneous Raman spectra of HSQ thin films are presented with peak assignments, and comparison to the DQSI-CARS spectra reveals that the non-totally symmetric modes are not accessible with DQSI-CARS. While the totally symmetric modes are sufficient to monitor the degree of HSQ cross-linking, with new variations of the single beam, broadband CARS technique, it will be possible to gain more information about not only HSQ, but also the properties of other rapidly-changing chemical systems.

4 Investigating the near-IR multiphoton cross-linking mechanism of HSQ

The power dependence of the HSQ cross-linking rate in the focused, pulsed near IR laser beam reveals that at high average powers (>45 mW) the process is initiated by absorption of approximately 6±1 near IR photons, similar to the amount of energy necessary for UV lithography at 157 nm, indicating a photoinduced cross-linking mechanism driven by ≡Si-H bond breaking. The cross-linking rate is much slower below this average power threshold, suggesting a photothermal bond redistribution mechanism at low powers. As a highly nonlinear process, the multiphoton HSQ cross-linking is very sensitive to spectral phase, or chirp, on the ultrafast pulse, with a greater than 100-fold increase in cross-linking rate when higher order chirp (3rd and 4th order spectral phase) is compressed at the beam focus within the sample. By controlling both the chirp and laser power, the HSQ cross-linking rate is finely tuned across a wide range of values while still maintaining a strong CARS signal. Various potential reaction mechanisms are explored to explain the highly non-linear power dependence and apparent reaction order of the multiphoton-induced cross-linking.

4.1 Introduction

Recently, features as small as 40 nm have been patterned in polymer photoresists using focused, pulsed near IR lasers via multiphoton absorption polymerization (MAP).[18, 60, 140] With direct-write multiphoton photolithography, it was even possible to expose and etch positive-tone resists with the laser in a single step, eliminating the need for post-exposure development.[59, 141] Power dependence studies of such processes have shown that they are highly non-linear, requiring the absorption of up to ~7 photons to initiate each bond breaking event in positive tone resists, producing features as narrow as 120 nm in PMMA with a single, tightly focused beam of pulsed 870 nm light (170 fs pulse duration).[59, 141] The lithographic resolution enhancement is greatest for highly nonlinear photoabsorption processes. The near infrared (NIR) induced HSQ cross-linking rate is very sensitive not only to average laser power but also peak intensity, indicating that it is a highly non-linear process. Therefore, by utilizing MAP of HSQ, it may be possible to pattern sub-micron features with direct-write lithography using relatively inexpensive pulsed NIR lasers. If the resolution is sufficient for microfabrication applications, the lower cost of the NIR exposure source is a big advantage when compared to the high cost of X-ray, e-beam and EUV sources otherwise required for patterning of HSQ.

Another particularly exciting application of MAP that cannot be achieved with single-photon or e-beam exposure processes is the fabrication of 3D micro and nanostructures in thicker films, such as photonic crystal fibers and 3D optical data storage structures.[17, 124, 140] While HSQ and related materials have not yet been investigated for these applications, exploring the NIR MAP of HSQ opens the door for new opportunities in complex 3D microstructure fabrication in HSQ and HSQ-like materials. Understanding the number of NIR photons, and thus the amount of energy, required to initiate the cross-linking gives a key insight into the photolytic process, whether it is dominated by or limited, for example, by ≡Si-H versus ≡Si-O bond breaking, and this knowledge can be used to fine tune the chemistry of HSQ-like resist materials for sensitive, high contrast multiphoton lithography, as well as for X-ray, e-beam and EUV lithography. Furthermore, with the same source used for exposure, broadband CARS

spectra are used for *in situ* analysis of the degree of cross-linking achieved. This is highly desirable for analyzing the chemistry and structural integrity of polymer microstructures, as previously demonstrated using narrowband CARS microscopy.[75, 142]

When the laser power before the microscope is maximized (67 mW average power) and the higher order chirp is fully compressed with the SLM (~38 fs pulse duration), both the CARS signal and HSQ cross-linking rate are maximized. However, when only the linear chirp is compressed, a slightly weaker CARS signal is detected without inducing appreciable HSQ cross-linking. Upon further investigation, it is evident that the rate of cross-linking is very sensitive to the degree of chirp, and hence the peak power, of the laser pulses. This suggests that each HSQ cross-linking event requires more photons, on average, than the third-order CARS process. To assess the non-linearity of the HSQ cross-linking rate, the pulsed NIR beam is focused into the HSQ thin film and the rate of decay of the concentration of cage-like HSQ species is measured repeatedly for different average laser powers, ranging from 34 mW to 67 mW. The cross-linking rate increases as the average power is increased, and a threshold power is observed above which the multiphoton non-linearity of the process appears to change, suggesting that there are different photoconversion mechanisms at low versus high laser power. These results are consistent with previous reports of multiphoton ablation lithography in positive tone resists.[59] The previously proposed HSQ cross-linking reaction mechanisms are presented in the context of these observations to explain the non-linear power dependence and apparent first order kinetics of the cross-linking reaction.

4.2 Sample preparation and experimental setup

Following the same methods as described in the chapter 3, HSQ films are prepared by spin-coating 200 μL of the flowable oxide solution (FOx-25®, DOW Corning) onto borosilicate glass microscope coverslips at 830 ± 30 RPM for 30 seconds, yielding films approximately 1 μm thick. Films are cured on a hot plate in air for 2 min. at 150 ± 5 ºC to evolve any remaining solvent. Again, the broadband CARS setup detailed in section 2.2.1 and Figure 2.3 is used to obtain coherent Raman spectra of the thin film samples. The light is focused on the sample through a 1.2 NA water-immersion objective (60x UPlanApo, Olympus), and the signal is collected through a 0.85 NA air objective.

As in Chapter 3, homodyne-amplified CARS spectra are collected with a spectral range of ~250 cm^{-1} to 1200 cm^{-1}. The kinetics of the HSQ cross-linking reaction are measured by focusing the beam into the HSQ thin film and acquiring the CARS spectrum in 500 ms intervals over a period of ~200 seconds at each laser power. The decay of the 562 cm^{-1} peak area, characteristic of the cage-like O-Si-O bend in HSQ, is analyzed versus exposure time, to assess the relative degree of cross-linking, decay lifetime and cross-linking rate for different laser pulse conditions. Optimal chirp compression at the microscope focus results in a pulse duration of ~38 fs, which is focused to a diffraction limited spot of ~400 nm diameter. With 67 mW of average power before the microscope, this corresponds to $\leq 7.8 \times 10^{12}$ W/cm^2 peak power density at the focus in the sample.

The HSQ cross-linking rate is controlled by adjusting the peak power of the laser at the microscope focus in two different ways: by adjusting the chirp at constant average laser power, or adjusting the average laser power with the same (constant) degree of chirp. As described in section 2.2.2, the chirp is measured immediately prior to inserting the sample by placing a BBO

crystal at the microscope focus; linear chirp (2^{nd} order spectral phase) is compressed by translating the second grating of the pulse shaper (Figure 2.4(a)) in order to optimize the SHG signal from the BBO, and the 3^{rd} and 4^{th} order spectral phase are then measured using MIIPS. First, the HSQ cross-linking is measured with only the linear chirp compressed at the microscope focus. Next, without removing the sample, the higher order chirp (3^{rd} and 4^{th} order spectral phase) is compressed by applying the appropriate phase with the SLM, as determined by the MIIPS measurement. With compressed pulses, the HSQ cross-linking rate is measured as a function of average laser power before the microscope, varied from 34.5 mW to 67 mW with a variable neutral density filter wheel placed just after the pulse shaper. Each measurement is taken at a single point in the HSQ thin film. Then, the laser power or chirp is adjusted, and the sample is subsequently translated laterally by ~20 μm to a new spot on same film.

To directly compare cross-linking rates and lifetimes at many different laser powers, the exact same focusing characteristics and pulse duration (based on the chirp) must be maintained for each measurement. This is challenging due to long-time drift in the chirp, laser power and beam pointing stability, so each full set of power dependence measurements (at constant chirp) was acquired within a period of less than two hours. To accomplish this, the kinetics curves at each power are measured for less than five minutes (300 seconds) each. Besides the small lateral shift to a new sample position for each measurement, nothing is changed between subsequent kinetics measurements in a given data set.

4.3 Dependence of cross-linking rate on peak intensity: chirp effects

For an average laser power of 67 mW before the microscope with only linear chirp compressed, the decay of the 562 cm^{-1} peak area, and thus the increase in HSQ cross-linking, proceeds only very slowly, as shown in the upper curve of Figure 4.1(a). By comparison, when the higher order chirp is compressed with the SLM at the same average laser power, the initial cross-linking proceeds more than 100 times faster, as shown in the lower curve in Figure 4.1(a). To directly compare the initial lifetime τ_1 of the chirped versus compressed measurements requires the same normalization for both curves, which is shown in Figure 4.1(b).

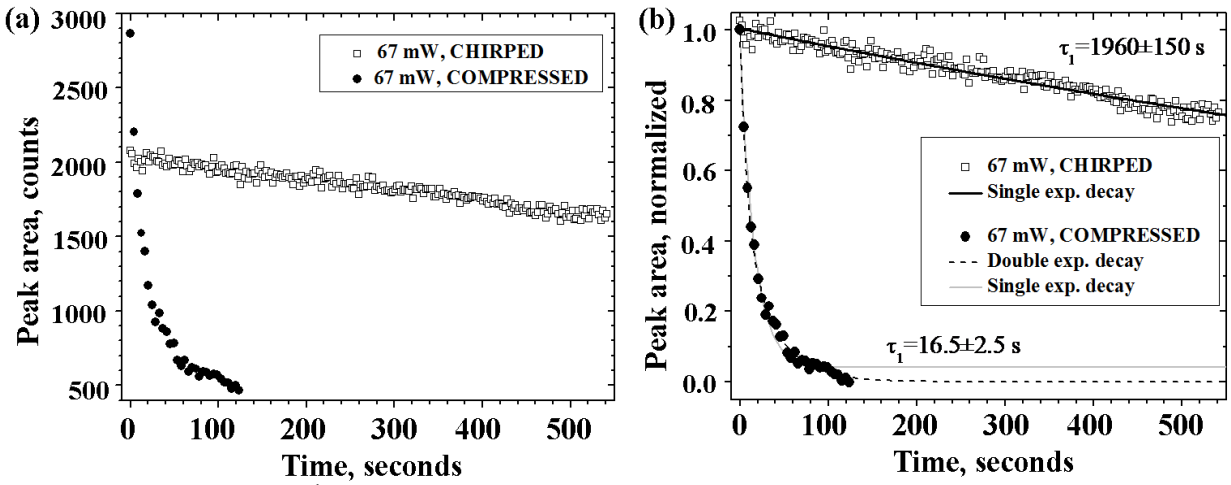

Figure 4.1 Decay in 562 cm^{-1} peak area for a chirped pulse (upper curve, open squares) versus compressed pulse (lower curve, filled circles) at the focus in the HSQ thin film, (a) raw data, before normalization and (b) normalized data, showing exponential decay fit curves with > 100x faster cross-linking rate when the chirp is compressed.

Based on many previous measurements (including those shown in Figure 3.3), a double-exponential decay profile is expected for all measurements of 562 cm^{-1} peak area versus exposure time, indicating two distinct stages of cross-linking.[79] However, for the compressed measurement (lower curve in Figure 4.1(a)), the cross-linking has proceeded only just past the first stage within the relatively short measurement time used here. The characteristic decay lifetime of the first stage, τ_1, defined as the time at which 1/e (37%) of the initial peak area remains, is determined for the raw data based on the single exponential decay equation:

$$A_t = y_0 + A_0^{(1)} e^{-t/\tau_1} \tag{4.1}$$

where A_t is the peak area at time t, and $A_0^{(1)}$ is the amplitude of the fit curve for the first stage. The offset y_0 is the minimum peak area reached at the end of the first cross-linking stage, which will be important when comparing different measurements. The initial peak area, A_0, for the raw data at t=0 is related to these parameters as:

$$A_0 = y_0 + A_0^{(1)}. \tag{4.2}$$

The data in Figure 4.1 yield an initial lifetime of 16.5 ± 2.5 s for the compressed measurement; the lower end of this range (14 s) fits the early points best, while the longer time (19 s) fits the later points better. This is similar to the previously reported initial lifetime of 24.4 ± 1.3 s (Figure 3.3) with slightly lower average power (~46 mW) and different chirp, as well. In all previous measurements, the lifetime of the second stage was always between 5 to 15 times longer than the first stage.

For the so-called "chirped measurement" shown in Figure 4.1(a), the cross-linking does not proceed enough within the measurement time to fit a single exponential decay to the raw data. Also, the CARS peak intensities are weaker when the pulse is chirped, causing the initial peak area to be lower for the chirped measurement. For fitting, it is assumed that the reaction will start with the same degree of cross-linking at t=0, and proceed to the same final degree of cross-linking at t=∞ regardless of cross-linking rate; thus, the relative offset for the chirped measurement, y_0'/A_0', is estimated to be the same as for the compressed measurement:

$$y_0' = \frac{y_0}{A_0} A_0' \tag{4.3}$$

where A_0' is the measured peak area of the chirped measurement at t=0, and the fixed offset y_0' is used to fit a single exponential decay to the chirped measurement. This yields an approximate single-exponential decay lifetime of τ_1=1960 ± 150 s for the first stage of the chirped measurement, which is ~119 times greater than for the first stage of the compressed measurement. With the chirped and compressed measurement each normalized to unity at their initial (maximum) peak area (A_0' and A_0, respectively), this large difference in cross-linking rates is clearly visible in Figure 4.1(b).

4.4 Non-linear power dependence of cross-linking rate

For the raw data in Figure 4.1(a), the CARS signal level increases by less than a factor of two after the higher order chirp is compressed, while the cross-linking is faster by a factor of more than 100, so it is clear that the HSQ multiphoton cross-linking is even more non-linear than the CARS process; that is, the reaction requires more than three photons to be absorbed per cross-linking event to proceed at an appreciable rate. To assess the number of photons necessary to initiate the cross-linking reaction, the cross-linking rate is measured as a function of laser power. As shown in Figures 4.2(a) and (b), the cross-linking rate clearly increases with increasing laser power. For data set 1 in Figure 4.2(a), the same chirp compression was maintained as for the compressed measurement in Figure 4.1. A slightly more optimized chirp compression was utilized for the data set 2, shown in Figure 4.2(b), which results in slightly higher cross-linking rates at the same average laser powers, due to the shorter pulse duration and therefore higher peak power.

Due to the extremely slow cross-linking at lower powers, analogous to the slow cross-linking in the chirped measurement (top curve of Figure 4.1), only the two highest power curves proceed past the first stage of the previously observed double exponential decay during the short measurement period. As described in the previous section, the normalized decay in peak area versus time for each laser power is fit to a single exponential decay to obtain the characteristic decay lifetime of the first stage, τ_1, for each laser power used. For all the curves at P<50 mW, the final peak area (offset, y_0') again had to be estimated, based on the more complete decay curves, according to equation 4.3, and fixed at that value to approximate the single-exponential decay lifetime. To see more clearly how the rate increases with laser power, the fit curves alone are plotted in Figures 4.2(c) and (d).

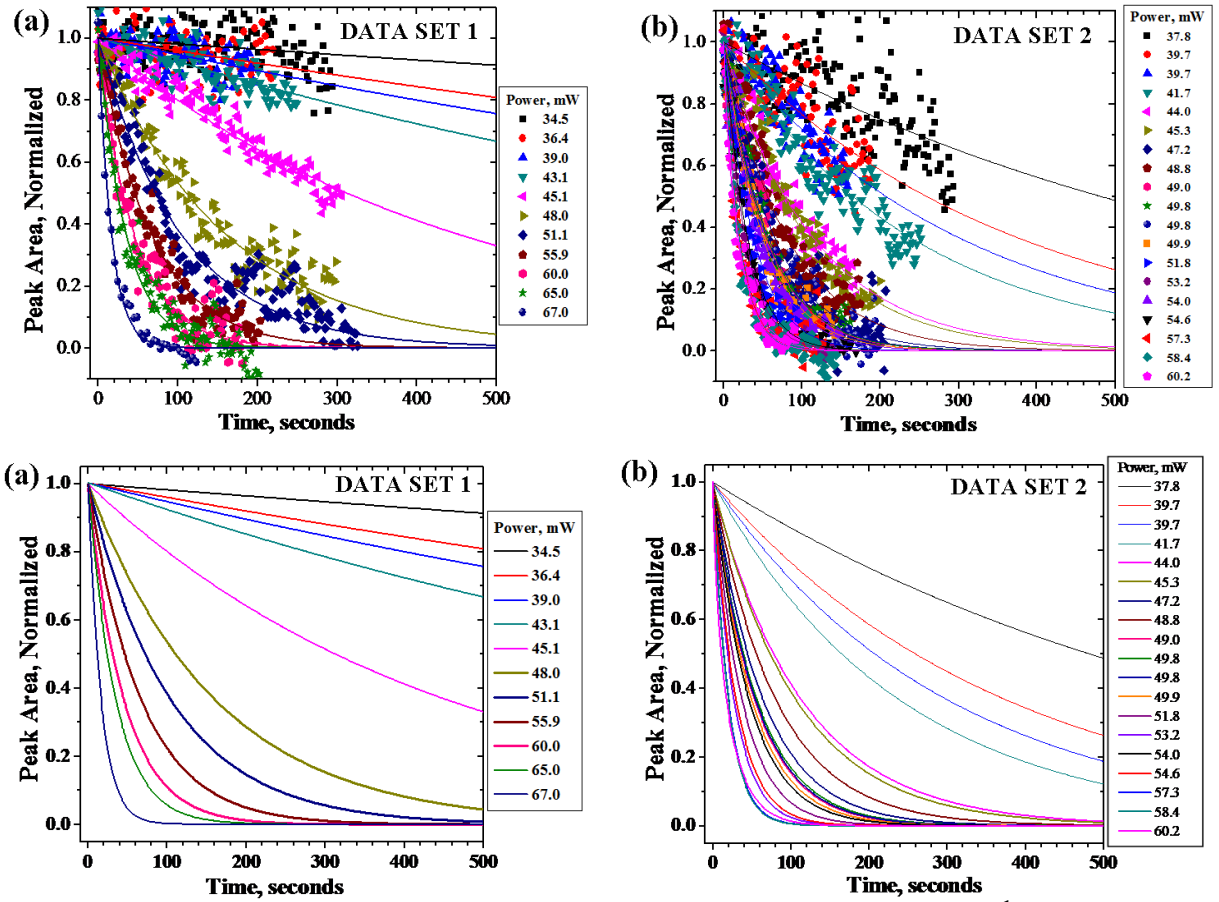

Figure 4.2 Normalized decay in the peak area for the cage-like HSQ band at 562 cm^{-1} at different laser powers for (a) data set 1, with slight chirp, and (b) data set 2, with optimal chirp compression. The normalized peak area is equivalent to the relative degree of HSQ cross-linking (Eq. 4.7). A strong increase in cross-linking rate is observed with increasing laser power in both set 1 and set 2. For clarity, single exponential decay fit curves are shown alone in (c) for data set 1 and (d) for data set 2. The better compression in set 2 results in slightly higher peak power and therefore slightly higher cross-linking rates at the same average powers.

HSQ cross-linking always involves a decrease in ≡Si-H linkages in exchange for more ≡Si-O-Si≡, and depending on the specific reaction steps, it is possible that other reactants are also consumed (such as O_2 or H_2O), and gaseous products released (such as SiH_4, H_2 or H_2O), explained in more detail in the following section (section 4.5). Regardless of the specific reaction pathway, it is clear that for pulsed 800 nm excitation, a single cross-linking event is only initiated when multiphoton absorption effectively "activates" a reactive site within the solid HSQ film. A simplified, net HSQ cross-linking reaction for a single cross-linking event can be expressed very generally as:

$$HSQ_{cage} + n\text{Photons} \rightarrow HSQ^*_{cage} \rightarrow HSQ_{network} \quad \textbf{(4.4)}$$

where HSQ_{cage} refers to a reactive site in the as-spun film, capable of forming a cross-link between "cage-like" species containing H, Si and O. HSQ^*_{cage} is the (short-lived) activated reactive site, prior to cross-linking, possibly including a neutral excited state complex, broken bonds, and ions or radicals. $HSQ_{network}$ refers to the "network-like" products of the single cross-linking reaction, whether only partially cross-linked (still contain H atoms) or cross-linked to the maximum extent possible, i.e. $SiO_{4/2}$. The photo-activated reactive site in HSQ is analogous to a

photoinitiator molecule utilized in UV curing of traditional polymers,[128] and first order kinetics are expected if the rate of the photochemical reaction depends on the probability of photoabsorption by this reactive site. The following laser power-dependent rate law is expected:

$$\frac{d[HSQ_{cage}]}{dt} = -k_1[HSQ_{cage}]P^n \tag{4.5}$$

where $[HSQ_{cage}]$ is the total concentration of reactive cage-like species, t is exposure time in seconds, P is the laser power in milliwatts (mW), n is the number of photons required to convert each cage-like HSQ site to a network-like site, and k_1 is a first order (or pseudo-first-order) rate constant with units of $mW^{-n}s^{-1}$. Solving for the concentration of cage-like species versus time:

$$[HSQ_{cage}]_{t,P} = [HSQ_{cage}]_{0,P} e^{-k_1 P^n t} \tag{4.6}$$

where $[HSQ_{cage}]_{0,P}$ and $[HSQ_{cage}]_{t,P}$ are the concentration of cage-like HSQ species present initially (t=0) and after exposure time t.

In these CARS measurements, the concentration versus time is not measured directly, but rather the integrated area of the 562 cm^{-1} CARS peak from the cage-like O-Si-O bend, A_t, versus exposure time at constant power in the focused near IR beam. The CARS peak intensity varies linearly with sample concentration, so the normalized peak area, $A_{t,norm}$, of the O-Si-O bend at 562 cm^{-1} after exposure time t at constant laser power P is directly proportional to the relative concentration of cage-like HSQ bonds remaining after exposure, and thus the relative degree of cross-linking which has occurred :

$$A_{t,norm} = \frac{[HSQ_{cage}]_{t,P}}{[HSQ_{cage}]_{0,P}}. \tag{4.7}$$

Inserting this into equation 4.6 gives:

$$A_{t,norm} = e^{-k_1 P^n t}. \tag{4.8}$$

Thus, equation 4.9 is equivalent to the single exponential decay fit (Eq. 4.1) with $y_0 = 0$. At the characteristic initial decay lifetime, τ_1, 1/e of the amplitude remains:

$$A_{\tau_1,norm} = \frac{1}{e} = e^{-k_1 P^n \tau_1}, \tag{4.9}$$

and taking the natural log gives:

$$\ln\left(\frac{1}{e}\right) = -k_1 \tau_1 P^n \tag{4.10}$$

revealing the equality:

$$\tau_1 = \frac{1}{k_1 P^n}. \tag{4.11}$$

The initial decay lifetime (τ_1) values are plotted (with error bars) versus average laser power (measured before the microscope) in Figure 4.3(a). The uncertainty in the lifetimes, incorporating both normalization uncertainty and noise, is approximately ±25% in set 1 and ±10% for set 2.

The rate constant k_1 is unknown, so to derive the average number of photons, n, required to initiate a single cross-linking event, the decay lifetime is compared for the various laser

powers. Taking the natural log of both sides of equation 4.11 and rearranging results in the form:

$$-\ln(\tau_1) = \ln(k_1) + n\ln(P). \quad \textbf{(4.12)}$$

Thus, a plot of $-\ln(\tau_1)$ versus $\ln(P)$ is linear, with slope n and y-intercept $\ln(k_1)$, as shown in Figure 4.3(b). A change in slope occurs at approximately 44 mW and 45.1 mW average power for data set 1 and set 2, respectively, suggesting that a different cross-linking mechanism occurs at lower powers. This is consistent with previously published works which show an average power "threshold" for multiphoton ablation of positive tone resists.[59] Here, the position of the threshold is defined to maximize the agreement of the linear fits with the individual data points, but the transition between these two regimes may not actually be well defined and instead exhibit a cross-over region of average powers in which both mechanisms are occurring to some extent. The n and k_1 values for each of the data sets and the average values are summarized in Table 4.1.

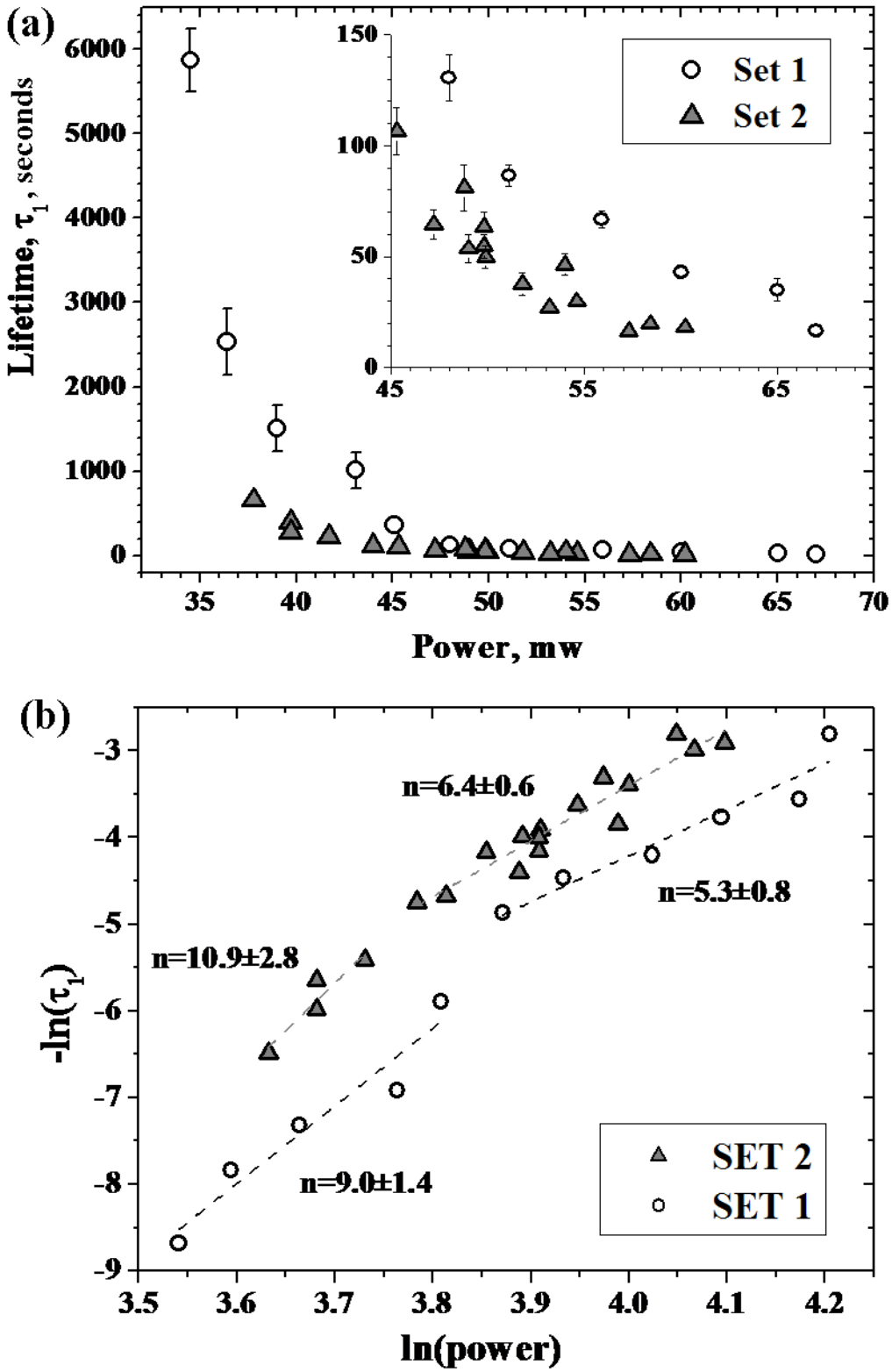

Figure 4.3 HSQ cross-linking lifetime versus laser power. (a) Full range of measurements, inset is zoomed in to high powers only, and error bars are encompassed by size of data markers where not visible. (b) Natural log form of data following Eq. 4.12, error bars not shown. Best fit lines reveal a threshold for cross-linking above which an average of ~6±1 photons is required per cross-linking event.

Data set	Threshold	Above threshold		Below Threshold	
		n (# of photons)	k_1 ($mW^{-n}s^{-1}$)	**n** (# of photons)	k_1 ($mW^{-n}s^{-1}$)
1	~45 mW	5.3 ± 0.8	$8.4\pm1.0\times10^{-12}$	9.0 ± 1.4	$3.5\pm0.4\times10^{-18}$
2	~44 mW	6.4 ± 0.6	$2.3\pm0.2\times10^{-13}$	10.9 ± 2.8	$8.6\pm1.9\times10^{-21}$
Average	n/a	5.9 ± 1.0	n/a	10.0 ± 3.1	n/a

Table 4.1 Summary of fit parameters based on Figure 4.3(b) and equation 4.12.

The non-linearity of the lifetime versus laser power for the different data sets agrees to within experimental uncertainty, suggesting that an average absorption of 6 ± 1 photons at a wavelength of ~800 nm is required to initiate the cross-linking process in the higher power regime, whereas at powers below the threshold an average of 10 ± 3 photons is required. The large error bar below threshold is due to the larger uncertainty in the offset y_0' for the low power curves, as well as worse signal-to-noise in low-power CARS spectra due to lower signal levels. For the low power curves, it is possible that the offset, y_0', is actually lower than estimated, due to a greater degree of cross-linking at $t=\infty$ with the slower reaction rate; this has been shown previously in UV cured polymers with photoinitiators, where a faster initial cross-linking rate limits the total degree of cross-linking by locking in the network structure and stopping the reaction at an earlier stage, with more unreacted monomers remaining.[128] At first it seems counter-intuitive that more photons are required per cross-linking event in the low average power regime, where the cross-linking rate is very low. However, it is possible that a completely different, photothermal mechanism is responsible for the cross-linking in the low power regime, where the energy of the ~10 photons is deposited over many different bonds, while the high-power regime involves direct photo-induced bond breaking. Understanding the non-linearity requires an in-depth look at the possible cross-linking mechanisms, provided in the following section.

The cross-linking rate constant k_1 is higher for data set 2 than for data set 1 because better chirp compression, and therefore higher peak power density, was utilized for set 2 at the same average powers. This higher rate constant (k_1) also results in the lower threshold power for set 2, as shown in Figure 4.3(b) and Table 4.1. This is consistent with the conclusion previously reported by Ibrahim *et al.* regarding multiphoton photolithography of positive-tone resists, where the $k\tau$ values of various materials were compared; a lower $k\tau$ resulted in a higher power threshold for multiphoton lithography and etching.[59]

Also noted by Ibrahim *et al.*, the multiphoton rate constant is very sensitive to small fluctuations in the microscope focus conditions, leading to large uncertainty on the order of $k\tau\pm100\%$. Variations in focus are analogous to variations in chirp, as either an increase in the size of the focal spot or an increase in the pulse duration will decrease the power density at the focus in the sample. For example, in the experiments presented here, an increase in the focal spot diameter from 400 nm to just 450 nm reduces the peak power density significantly, by ~21% (calculated). Likewise, for a fixed spot size of 400 nm at constant average power, a very small amount of chirp is sufficient to increase the pulse duration from 38 to 48 fs, which also reduces the peak power density by ~21% (calculated). Therefore, more realistic error bars on the k_1 values from the linear fit may be on the same order of magnitude as the values themselves.

This sensitivity to peak power explains the fluctuations observed between measurements in the present study. As noted previously, small changes in chirp and focusing likely occur over

time due to variations with sample position, beam pointing, and temperature of optics in the SLM and laser cavity. For the data in set 1, the 67 mW points (chirped and compressed) were acquired first, and the remaining curves were then measured sequentially (in order) from low to high power. Thus, any small drift in the system may lead to systematic error and slightly alter the slope of the fit lines for data set 1 in Figure 4.3(b). However, for data set 2, the measurement of low and high power kinetics curves was alternated in a random order to randomize the effects of long term drift. This is evident in Figure 4.3(b) as larger scatter in the points for data set 2.

Table 4.2 summarizes the average laser powers and measured lifetimes. A single exponential lifetime is used for comparing lifetimes, but double exponential fits can be approximated for a few of the highest power curves. The estimated lifetimes from the double exponential decay, τ_1' and τ_2, are also reported in Table 4.2 when possible. However, due to the short measurement time, these double exponential decay lifetimes are generally underestimated, and they are not accessible for the lower power measurements. In future experiments, it is desirable to improve the long-term stability of the system to measure the decay curve at each power for a much longer acquisition time, such that the τ_1 lifetimes can be assessed with more certainty, and the τ_2 lifetimes can be used to determine the non-linearity of the second stage, as well.

Power, mW (± 0.2 mW)	Single exponential fit decay lifetime, τ_1, seconds	Double exponential fit decay lifetimes, seconds	
		τ_1'	τ_2
67, CHIRPED	1960 ± 150		
DATA SET 1, Nearly Optimized Chirp Compression			
67, COMPRESSED	16.5 ± 2.5	7.6 ± 3.6	33.7 ± 6.3
65.0	35.0 ± 5.0	22.2 ± 4.8	350 ± 350
60.0	43.1 ± 3.0		
55.9	66.8 ± 3.8		
51.1	86.6 ± 5.0		
48.0	130.5 ± 10.2		
45.1	361 ± 90		
43.1	1009.3 ± 218		
39.0	1509.4 ± 271		
36.4	2531.8 ± 395		
34.5	5872.9 ± 377		
DATA SET 2, Optimized Chirp Compression			
60.2	18.2 ± 1.1	5.6 ± 3.6	25.6 ± 7.2
58.4	19.7 ± 1.8	15.3 ± 2.6	163 ± 163
57.3	16.6 ± 0.8		
54.6	29.8 ± 1.6		
54	46.5 ± 3.4		
53.2	27.2 ± 0.7		
51.8	37.6 ± 4.9		
49.9	49.8 ± 3.4		
49.8	63.7 ± 4.6		
49.8	54.7 ± 4.0		
49	53.6 ± 6.5		
48.8	81.1 ± 10.3		
47.2	64.4 ± 4.4		
45.3	106.4 ± 3.1		
44	114.9 ± 3.1		
41.7	225 ± 13		
39.7	397 ± 21		
39.7	284.5 ± 15		
37.8	659 ± 38		

Table 4.2 Summary of all measured power values and time constants for near IR HSQ cross-linking.

4.5 A closer look at potential cross-linking mechanisms and reaction order

As mentioned previously, the high degree of non-linearity for MAP of HSQ is expected based on previous reports of HSQ cross-linking only at exposure wavelengths ≤ 157 nm, corresponding to a photon energy of 7.90 eV. By comparison, the laser spectrum used in this study covers the range from 740 nm to 860 nm, or photon energies from 1.44 eV to 1.67 eV. The non-linearity of 6±1 photons for the pulsed NIR-induced cross-linking "above threshold"

corresponds to 9.4 ± 2.2 eV, the lower limit of which is near the same energy as a single 157 nm photon. This is sufficient to break approximately one SiO bond (~8.94 eV) or two SiH bonds (~4.08 eV each), with any excess energy possibly going into thermal excitation. Notably, a single 157 nm photon would be sufficient to break two ≡Si-H bonds only if the ≡Si-H bond dissociation energy in HSQ is ~3.95 eV, just slightly lower than the previously reported value of ~4.08 eV (under unknown conditions).[43] The exact ≡Si-O and ≡Si-H bond strengths in the HSQ thin film probably do vary somewhat from reported literature values, based on specific sample characteristics. More than one explanation is possible for the high degree of non-linearity in each stage, and several hypotheses are explored here.

Two previously proposed mechanisms, shown below, depend upon the cleavage of two ≡Si-H bonds on adjacent Si atoms to initiate a single cross-linking event. The e-beam mechanism is expected to involve direct ≡Si-H bond cleavage followed by the uptake of water, leading to one added oxygen atom per cross-linking event:[37]

$$2\ \equiv\!\text{Si-H} + 2\ H_2O + \Delta E \longrightarrow \equiv\!\text{Si-O-Si}\equiv + H_2O + 4\ H^{\bullet} \qquad \textbf{(4.13)}$$

via the following reaction steps:

$$\begin{aligned} &\equiv\!\text{Si-H} + \text{H-Si}\equiv + \Delta E \longrightarrow \equiv\!\text{Si}^{\bullet} + {}^{\bullet}\!\text{Si}\equiv + 2\ H^{\bullet} \\ &\equiv\!\text{Si}^{\bullet} + {}^{\bullet}\!\text{Si}\equiv + 2\ H_2O \longrightarrow \equiv\!\text{Si-OH} + \text{HO-Si}\equiv + 2\ H^{\bullet} \\ &\equiv\!\text{Si-OH} + \text{HO-Si}\equiv \longrightarrow \equiv\!\text{Si-O-Si}\equiv + H_2O \end{aligned} \qquad \textbf{(4.14)}$$

where ΔE is energy deposited via e-beam. The fate of the H radicals has not been reported, but it is possible that they form H_2, and/or react with additional Si or O atoms in the HSQ network. A very similar mechanism has been proposed for thermally-induced HSQ cross-linking at high temperatures (>400 °C), which also involves ≡Si-H cleavage and the uptake of oxygen atoms from O_2 instead of water:[129]

$$\begin{aligned} &\equiv\!\text{Si-H} + \text{H-Si}\equiv + O_2 + \Delta E \longrightarrow \equiv\!\text{Si-OH} + \text{HO-Si}\equiv \\ &\equiv\!\text{Si-OH} + \text{HO-Si}\equiv \longrightarrow \equiv\!\text{Si-O-Si}\equiv + H_2O \end{aligned} \qquad \textbf{(4.15)}$$

where ΔE is thermal energy. Although two ≡Si-H bonds must be broken per cross-linking event in either case, the reaction depends upon the two species being in close proximity, so it could still be first order in the number of properly oriented and juxtaposed reactive sites. The initial rate would not likely be limited by the number of individual ≡Si-H bonds present, as they are greatly in excess. Thus, the ~6 photon dependence and possibly first order reaction kinetics (above the threshold) could indicate the breaking of two adjacent ≡Si-H bonds for each cross-linking event.

Perhaps because the ≡Si-H bond is weaker, and the onset of photolytic conversion is 157 nm, no previous mechanisms have mentioned the direct cleavage of an ≡Si-O bond to initiate cross-linking, but the ~9.4 eV energy dependence revealed here is just slightly higher than the expected ≡Si-O bond strength. Thus, another possible photolytic pathway could be cleavage of a single ≡Si-O bond, essentially resulting in a cage opening, followed by the bond redistribution (exchange) mechanism shown in Figure 4.4, where "**R**" represents the remaining cage-like or

network-like structure connected to the oxygen atom. The probability of redistribution in this case would also depend upon the proper juxtaposition and proximity of the neighboring Si atom to the broken ≡Si-O bond. This exchange reaction cross-links adjacent cages, leading to partial network formation, and is closely based on a reported (suggested) low-temperature redistribution mechanism, discussed in more detail below and shown schematically in Figure 4.5(b).[129] Notably, a single 157 nm photon is insufficient to cleave an ≡Si-O bond.

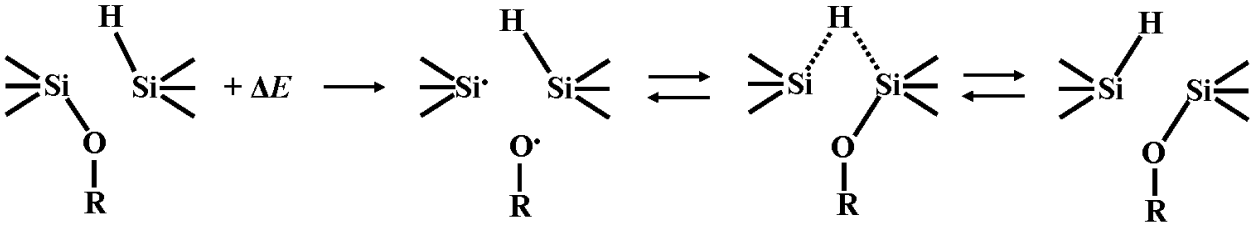

Figure 4.4 Possible redistribution mechanism induced by direct, photolytic ≡Si-O bond cleavage.

Also not mentioned in any previous reports, ≡Si-OH (silanol) is likely present initially at low concentrations, substituted for ≡Si-H on some cages in the spin-on preparations by the manufacturer to increase the HSQ solubility.[132, 143-144] According to equations 4.14 and 4.15, the presence of ≡Si-OH prior to exposure would also result in an increased reaction rate, and thus enhanced film sensitivity. If existing ≡Si-OH reacts with ≡Si-H (in excess), the initial limiting reactant could be ≡Si-OH, or the entire reactive site including ≡Si-OH and an adjacent ≡Si-H in the proper configuration. If this is the case, the reaction rate is expected to slow down dramatically after the initial ≡Si-OH is consumed, and after that the rate depends upon only dual ≡Si-H scission, as in mechanisms 4.14 and 4.15, leading to a two-stage mechanism. However, as silanol groups are highly reactive with each other, the ≡Si-OH concentration in solution must be relatively low, or significant cross-linking would occur in the solution prior to any exposure. A small amount of cross-linking of the stock solution does in fact occur over time, especially if the sample is not stored below room temperature.[2, 48, 132, 144] If ≡Si-OH is present, it is also possible that O-H bond cleavage (~5 eV dissociation energy) plays a role, and the energy of one O-H bond plus one ≡Si-H bond also matches the observed (average) energy dependence for a single cross-linking event of ~9.4 eV, indicating the following reaction if a sufficient initial concentration of ≡Si-OH is present:

$$\begin{aligned} \equiv\text{Si-H} + \text{HO-Si}\equiv + \Delta E &\longrightarrow \equiv\text{Si}^{\bullet} + {}^{\bullet}\text{OSi}\equiv + 2\,\text{H}^{\bullet} \\ \equiv\text{Si}^{\bullet} + {}^{\bullet}\text{OSi}\equiv &\longrightarrow \equiv\text{Si-O-Si}\equiv \end{aligned} \qquad \textbf{(4.16)}$$

where ΔE is energy from the pulsed NIR beam. Analogous to equation 4.14, a similar mechanism would require only a single ≡Si-H bond scission on the HSQ, if adjacent to an existing ≡Si-OH prior to exposure:

$$\begin{aligned} \equiv\text{Si-H} + \Delta E &\longrightarrow \equiv\text{Si}^{\bullet} + \text{H}^{\bullet} \\ \equiv\text{Si}^{\bullet} + \text{H}_2\text{O} &\longrightarrow \equiv\text{Si-OH} + \text{H}^{\bullet} \\ \equiv\text{Si-OH} + \text{HO-Si}\equiv &\longrightarrow \equiv\text{Si-O-Si}\equiv + \text{H}_2\text{O} \end{aligned} \qquad \textbf{(4.17)}$$

and it is possible that both equations 4.16 and 4.17 occur if ≡Si-OH is present initially with sufficient concentration.

The presence of ≡Si-OH is possibly indicated by the strong 830 cm^{-1} peak in the spontaneous Raman spectrum in Figure 3.5(b), but other SiOH bending modes at ~760 cm^{-1}, ~880 cm^{-1} and ~980 cm^{-1} are potentially concealed by the very strong SiOSi or OSiO peaks in the HSQ Raman spectra[135-138] (see Table 3.1), and there is some controversy regarding the assignment of SiOH bending modes in Raman and IR spectra of various other samples.[134] An SiOH stretching frequency occurs at ~3750 cm^{-1},[137] but unfortunately this is just beyond the spectral range in Figure 3.5(b), where the signal drops off above ~3700 cm^{-1}. Notably, some previously reported FTIR spectra of HSQ thin films also lose signal-to-noise beyond ~3000 cm^{-1}, and the water absorption is very strong between 3200-3600 cm^{-1} in IR spectra.[37] The SiOH bending and stretching peaks are apparently highly sensitive to the local H-bonding environment,[134-136] so it is also possible that the peaks in HSQ thin film are shifted considerably from literature values obtained using other types of materials. More sensitive Raman and/or FTIR spectroscopy of HSQ thin films in the region from 3600-3900 cm^{-1} is desired to look for the SiOH stretch, and ≡Si-OH content is explored in more detail in the NEXAFS spectroscopy described in section 5.3.

At average powers "below threshold," the near IR cross-linking data suggests that 10 ± 3 photons, or 15.9 ± 5.8 eV (uncertainty accounts for full laser bandwidth), must be absorbed to initiate cross-linking, indicating a different type of mechanism. Specifically, there is a thermal bond redistribution mechanism which may dominate at low laser powers, rather than direct bond breaking by photochemical mechanisms. If this photothermal mechanism is first order, the higher amount of absorbed energy could be distributed over many different species in the reactive site rather than absorbed by just one or two bonds. However, if this mechanism is not first order in reactive site concentration, the first-order equation 4.9 would not be valid, and the slope of the linear plot in Figure 4.3(b) would not actually represent the number of photons absorbed per cross-linking event. Because of the large uncertainty in the low power measurements, an additional possibility is that the photon dependence for the two stages is actually very similar (~7 photons, or ~11 eV, if considering the bounds of the uncertainty on measurements below and above threshold).

In the thermally-induced bond redistribution in HSQ at 190 °C to 330 °C, cross-linking occurs leading to units with varied H content up to the most highly cross-linked, glass-like species $SiO_{4/2}$ and evolved silane gas, $SiH_4(g)$:[129]

$$2\ HSiO_{3/2} + \Delta E \longrightarrow SiO_{4/2} + H_2SiO_{2/2} \qquad \textbf{(4.18)}$$

where the $H_2SiO_{2/2}$ can go on to react further:

$$HSiO_{3/2} + H_2SiO_{2/2} + \Delta E \longrightarrow SiO_{4/2} + H_3SiO_{1/2} \qquad \textbf{(4.19)}$$

$$HSiO_{3/2} + H_3SiO_{1/2} + \Delta E \longrightarrow SiO_{4/2} + SiH_4(g) \qquad \textbf{(4.20)}$$

and ΔE is thermal energy. This is expected to involve a 4-centered intermediate, shown in Figure 4.5, with the subsequent cleavage and re-formation of exactly one ≡Si-O and one ≡Si-H bond per cross-linking event.[129] The fractional bond orders are used to indicate species that are not independent but chemically bound to a cage or network through their oxygen atoms. This reaction thus increases the ratio of ≡Si-O-Si≡ to ≡Si-H bonds by loss of silane (after multiple cross-linking events), without incorporating oxygen atoms from an outside source.[36, 129]

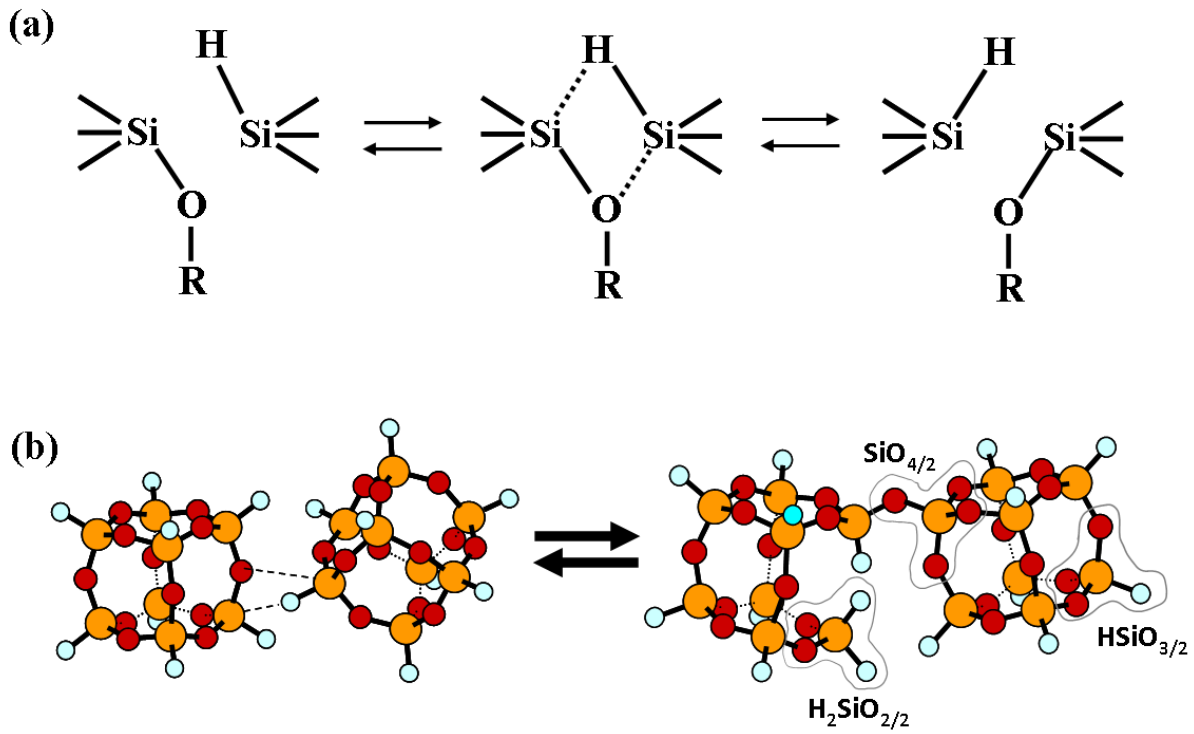

Figure 4.5 Schematic representation of the proposed 4-centered intermediate of the redistribution reaction, shown (a) in the plane of the page, where R represents any interconnected species,[129] and (b) in a slightly more realistic geometry, which shows possible interconnected species for the first cross-linking event.

All of the previously proposed reaction mechanisms are summarized schematically in Figure 4.6. One thing they have in common is that two species must come together to form a cross-link. However, to understand the reaction order for cross-linking of HSQ, as opposed to traditional chain-like organic polymers, it is challenging to define independent reactive species. For example, the $HSiO_{3/2}$ or $H_2SiO_{2/2}$ moieties are not independent but share all of their oxygen atoms with adjacent Si atoms. As stated previously, for kinetics measurements in the solid HSQ film, where the mobility of individual species or even independent monomer cages is severely restricted, it makes more sense to consider an entire reactive site, including all adjacent atoms, as a single reactant. This is equivalent to saying that in order for two species to cross-link within the solid, they must be adjacent and in approximately the proper geometry prior to exposure. For example, in the redistribution reaction shown in Figure 4.5, all of the atoms directly involved in the 4-centered intermediate and their nearest neighbors can be considered collectively as the reactive site. The cross-linking will not occur unless all of these species are present locally and oriented with the proper geometry prior to exposure in the as-spun film, and thus the reaction rate could be limited by the concentration of these specific reactive sites within the focal volume. For the above threshold cross-linking, at least, this is supported by the apparently first order kinetics, which suggest that the rate is not limited by two or more individual species coming together, but rather by the concentration of a single, reactive unit. Other photoinduced cross-linking reactions, which involve photoinitiator molecules as the absorbing species, have also been observed to follow apparent first order kinetics.[128] However, it is important to note that the order of the observed kinetics may only indicate the order of the photolytic activation step, and not necessarily reveal the overall order of the reaction.

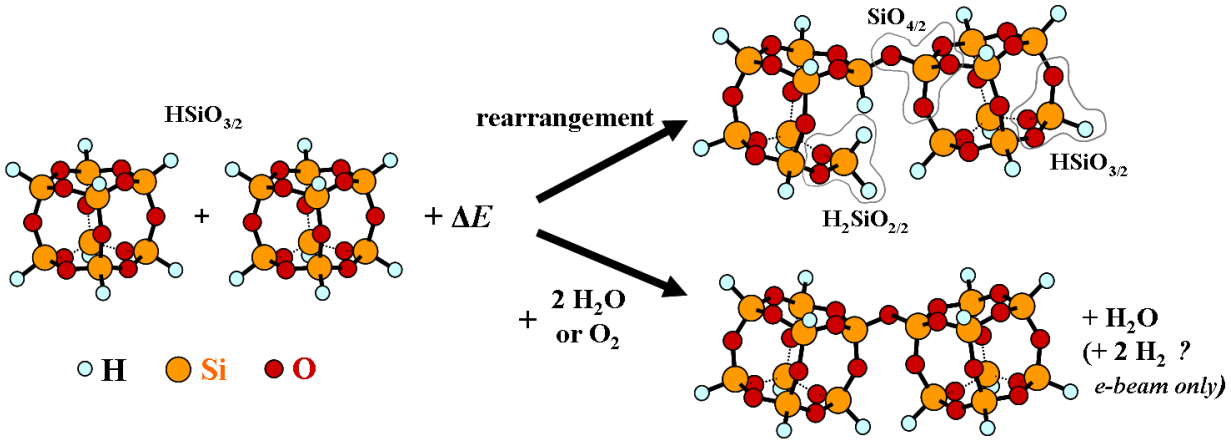

Figure 4.6 Schematic representation of silsesquioxane cage structure and comparing two possible network structures formed by a single HSQ cross-linking event. Δ*E* represents energy from either an electron beam, light (X-rays, EUV, ultrafast pulses), or heat. The upper pathway represents the primary mechanism proposed for thermally induced cross-linking from ~190-330 °C,[36, 129] while the lower is the main mechanism proposed in the literature for e-beam exposure[37] and heating above 400 °C.[36, 129] The spin-on solution of HSQ (Dow Corning FOx®) contains a mixture of cages and oligomers of HSQ.

Coming back to the below threshold cross-linking, the reaction order really cannot be assessed from the observed decay curves, as they are only linear and too short relative to the slow rate of the reaction, but several possibilities are considered here. If the rate of redistribution depends upon the concentration of properly-oriented reactive sites prior to exposure (as in the left hand side of Figure 4.5(a) or (b)), the reaction will likely be first order with respect to the concentration of reactive sites. For first order kinetics, equation 4.9 holds, and the non-linearity of 10±3 photons is an accurate representation of the energy required per cross-link. This photothermal absorption could be distributed through all the different bonds involved in the cross-link rather than absorbed by a single bond. However, if the thermal energy causes sufficient molecular motion (vibrational and rotational) to re-orient any of the multitude of ≥Si-H and ≥Si-O-Si≤ bonds and overcome the energy barrier for the formation of the 4-centered intermediate, then the reaction may be pseudo-zero-order. That is, it will be first or second order in the concentration of H-containing species (i.e. $HSiO_{3/2}$, $H_2SiO_{2/2}$ and/or $H_3SiO_{1/2}$), following equations 4.13 to 4.15, but all such species are in excess throughout the initial stage of the reaction, so the initial rate will not depend on the concentration of any given species. If this is the case, equation 4.9 does not hold, the final degree of cross-linking is unknown, and the number of photons absorbed per cross-linking is undetermined for this "below threshold" cross-linking. Again, enhanced stability for longer-time measurements (>500 seconds each) could provide information on the reaction order of the below-threshold cross-linking, as well as the τ_2 lifetimes for the above threshold measurements, to assess the non-linearity and differences between the mechanism of the first and second stage of the reaction.

4.6 Conclusions

The NIR induced HSQ cross-linking rate is highly non-linear with laser power, with an average of 6±1 photons required to initiate each cross-linking event above an average power threshold of ~45 mW for the pulse durations used here (~38 fs). The energy required per cross-

link is consistent with previously proposed reaction mechanisms involving direct ≥Si-H bond cleavage by e-beam or heat, but additional possibilities are presented involving existing ≥Si-OH (silanol) groups in the as-spun thin films or ≥Si-O bond scission. Further studies are required to assess the initial concentration of ≥Si-OH in the films, as the spontaneous Raman spectra (Chapter 3) are inconclusive, but X-ray spectra presented in Chapter 5 do indicate the presence of ≥Si-OH. First-order kinetics for photochemical conversion are suggested by the shape of the decay curves, and based on literature reports of UV curing in traditional polymers.[128] The two-stage nature of the reaction with exposure time is possibly due to the loss of ≥Si-OH groups with cross-linking, the increasing rigidity of the cross-linked network, and/or the consumption of easily cross-linked reactive sites.

Below the observed threshold of ~45 mW, slower cross-linking is observed with a slightly different power dependence, possibly by a photothermal bond redistribution mechanism. Assuming first order kinetics below the threshold, this suggests an average absorption of 10±3 photons per cross-link. However, while the rate-limiting step in the photolytic conversion above the threshold appears to be first order, the results of the present study cannot confirm that the kinetics are also first order below the threshold.

The cross-linking rate is highly dependent on the peak power of the laser pulses, and thus the degree of chirp (spectral phase). Compression of the higher order chirp with the SLM (3^{rd} and 4^{th} order spectral phase) results in a >100 fold increase in the HSQ cross-linking rate for the same average laser power, but just a two-fold increase in DQSI-CARS signal intensity. Thus, by utilizing chirped pulses and fast scan rates, DQSI-CARS should be capable of imaging HSQ and other sensitive polymer photoresists without inducing significant damage by using damage-mitigation techniques such as fast scan rates, similar to the STXM techniques detailed in Chapter 5. On the other hand, higher average and/or peak laser power can provide rapid cross-linking for direct-write NIR MAP lithography. With the high order non-linearity of the cross-linking process, this multiphoton lithography may provide an important new tool for microfabrication in HSQ and related materials.

5 Probing HSQ cross-linking chemistry on the nanoscale

This chapter is based on the following publication:
Caster, A.G.; Kowarik, S.; Schwartzberg, A.M.; Tivanski, A.; Gilles, M.K.; Leone, S.R. Quantifying Reaction Spread and Sensitivity in Hydrogen Silsesquioxane Latent Patterns with Direct-Write X-ray Lithography and X-ray Microspectroscopy, *J. Vac. Sci. Technol. B,* in preparation.

Direct-write soft X-ray lithography with an approximately 50 nm diameter beam is used to pattern narrow features in hydrogen silsesquioxane (HSQ) thin films, and scanning transmission X-ray microscopy (STXM) of the undeveloped patterns (latent patterns) with 30 nm resolution at the oxygen K-edge reveals a two-stage cross-linking mechanism. A dose and thickness dependent spatial spread of the cross-linking reaction beyond the exposure boundaries is observed. Oxygen and silicon near edge X-ray absorption fine structure (NEXAFS) spectra of latent patterns show an increase in overall oxygen content and no change in silicon content within exposed regions. For line exposures with 580 eV X-rays (λ=2.14 nm), a lateral spread in the cross-linking reaction of at least 70 nm on either side of the exposure boundary at FWHM is observed in 330 ± 50 nm thick HSQ films at low dose (0.6 ± 0.3 MGy, 27 ± 12 mJ/cm^2) and up to 150 nm spread at higher dose (111 ± 29 MGy, 5143 ± 1027 mJ/cm^2) (1 MGy = 10^6 J/kg absorbed energy). The results depend on the age and storage characteristics of the HSQ stock solution. Sharper lines are observed after room temperature development of the patterned negative tone HSQ in NaOH/NaCl solution (onset dose of 3.9 ± 1.0 MGy, 181 ± 36 mJ/cm^2), due to removal of material below a critical degree of cross-linking. Strong area-dependent exposure sensitivity is observed when imaging undeveloped patterns of various dimensions, which is attributed to the spread of cross-linking beyond the exposure boundary. Given the short range spread (< 10 nm) of low energy secondary electrons (≤ 580 eV) in condensed media, the observed spread is likely due to the propagation of reactive ions or radicals beyond the exposed region.

5.1 Introduction: STXM and X-ray Lithography of HSQ

To answer questions pertaining to the chemical changes induced by exposure alone, it is now possible to image undeveloped patterns in photoresists at high resolution (~30 nm) with scanning transmission X-ray microscopy (STXM).[50] Based on differences in bonding structure around the Si and O atoms in HSQ after cross-linking, changes are observed in the near edge X-ray absorption fine structure (NEXAFS) spectra, and these changes are used to monitor the relative degree of cross-linking in the exposed and unexposed regions of the HSQ film before it is developed (latent pattern). In earlier work on STXM imaging of undeveloped HSQ patterns, it was reported that at high e-beam doses (approx. 50 mC/cm^2 in a 250 nm thick film), a small but measureable degree of chemical change reached as far as 12 μm beyond the exposure boundaries.[50]

This chapter details NEXAFS spectroscopy and STXM imaging of X-ray exposed but undeveloped HSQ films to measure the cross-linking rate and X-ray exposure sensitivity of HSQ and to quantify the range of the reaction spread in the absence of development effects. A two-stage, first order X-ray induced cross-linking process is observed, similar to that observed for the

near IR multiphoton cross-linking, resulting in the incorporation of additional oxygen atoms into the cross-linked regions. A FWHM spread of the cross-linking reaction is observed to be greater than 70 nm, depending on the film thickness and X-ray dose, and the reaction spread is shown to cause proximity effects leading to significant area-dependent sensitivity. Comparing the same patterns before and after development in solution, the NaOH/NaCl developer washes away the partially cross-linked material evident in the undeveloped HSQ images, as anticipated, including cross-linking caused by reaction spread.

5.2 Sample Preparation and experimental setup

HSQ thin films from 100-500 nm thick are prepared on 100 nm thick silicon nitride substrates. For patterning, spectroscopy, and imaging, the sample patterns are written and analyzed in the 5.3.2 STXM described in section 2.4.[120] For X-ray lithography, X-rays at either 536 eV or 580 eV are tightly focused on the film surface to an approximately 50 nm diameter spot (FWHM), and the sample is raster scanned through the stationary X-ray beam in a pre-defined pattern. NEXAFS spectra of the films are measured across the oxygen atom K-edge (520 eV to 700 eV) to measure changes in the chemical structure around the oxygen atoms before and after X-ray exposure. Within 5 minutes after patterning, images of exposed patterns are obtained with ~30 nm spatial resolution without significant further sample damage by reducing the photon flux and scanning the sample more rapidly through the X-ray beam at a fixed energy (536 eV, oxygen K-edge). Images are analyzed to measure the relative degree of chemical change for each exposure dose and the lateral spread of the X-ray induced chemistry. Additionally, NEXAFS spectra at the silicon atom K-edge (1825 eV to 1880 eV) are measured before and after exposure at the STXM on beamline 11.0.2 of the ALS.[145]

To prepare HSQ films, 5 μL of Dow Corning XR-1541 (6% HSQ in methyl isobutyl ketone, for 100 nm thick films), Dow Corning FOx-15® (15-40% HSQ in methyl isobutyl ketone, for 300-400 nm thick films), or Dow Corning FOx-25® (15-40% HSQ in toluene, octamethyltrisiloxane and hexamethyldisiloxane, for 500 nm thick films) are spin-cast at 2000-6000 RPM for 30 s onto a 100 nm thick silicon nitride (Si_3N_4) membrane substrate (Silson Limited, shown in Figure 2.17). This thin silicon nitride has a high transmission in the X-ray energy regions of interest. The transmitted spectrum and photon flux through a blank substrate are measured periodically to record the background for all analyses. The reported results were obtained using HSQ stock solutions stored continuously at -15 °C for up to 2.5 years prior to film preparation. The results may vary if freshly synthesized HSQ material is utilized immediately. Only those films noted as "pre-baked" are baked on a hot plate in air for 5 min at 150 °C to drive off excess solvent prior to exposure. As the HSQ films are smooth and featureless, 100 nm gold nanoparticles are added on top of the film to enable sharp focusing of the X-ray beam on the surface, a requirement for producing the sharpest lithographic features and highest imaging resolution with the microscope. After placing a 1.5 μL droplet of very dilute nanoparticles on the surface, the films are dried and stored in air for 15 hours before being placed under vacuum in the X-ray microscope sample chamber. The sample chamber is evacuated to 0.2 Torr (~26.7 Pa) (sufficient to remove excess solvent in unbaked samples) then backfilled with 300 Torr of He.

As detailed in section 2.4, the STXM at beamline 5.3.2 uses a 25 nm outer-diameter Fresnel zone plate lens to focus synchrotron-generated soft X-rays on the HSQ thin films. The

monochromator is used to select the photon energy, and three sets of monochromator slits control the photon flux and spatial resolution of the microscope (as shown in Table 2.2). In this experiment, wider settings for the three slits (80 μm, 40 μm, and 40 μm) are used for lithography, giving a photon flux on the order of 10^6 photons/s and ~50 nm beam diameter (FWHM), while narrower slits (40 μm, 20 μm, and 20 μm) are used for imaging, reducing the photon flux by a factor of ~4 and improving the spatial resolution to ~30 nm (Rayleigh limit, based on zone plate outer diameter[4]). The depth of focus for these experiments (equation 2.39)[4] is ~1.0-1.2 μm, so 100 nm diameter gold particles are used to bring the beam focus to within ± 500 nm of the film surface prior to all patterning and imaging, and thus the beam is tightly focused through the entire film thickness (≤ 500 nm).

To obtain images, the X-ray transmission through the sample is measured at a fixed photon energy as the sample is scanned through the beam. For NEXAFS spectra, the photon energy is scanned across a range of values for each sample position of interest. For both imaging and spectroscopy, the measured transmission is compared to transmission through a blank silicon nitride membrane substrate and converted to optical density (OD) according to the natural log form of Beer's law (analogous to equation 2.34):

$$OD = -\ln\left(\frac{I}{I_0}\right) = \mu(E)\rho l \qquad \textbf{(5.1)}$$

where I is the X-ray flux through the sample plus substrate and I_0 is the incident photon flux through the blank substrate. The OD is sensitive to the film thickness, *l,* density, *ρ,* and energy-dependent mass absorption coefficient, *μ(E)*. A minimum film thickness of ~300 nm is used to achieve a high signal-to-noise ratio in STXM imaging of unexposed and exposed HSQ regions at the oxygen K-edge. The contrast within each image, which will be related to the degree of cross linking, is quantified by calculating the relative OD between the exposed and unexposed regions:

$$\Delta OD = \left|OD_{exposed} - OD_{unexposed}\right| = \left|-\ln\left(\frac{I_{exposed}}{I_0}\right) + \ln\left(\frac{I_{unexposed}}{I_0}\right)\right| = \left|-\ln\left(\frac{I_{exposed}}{I_{unexposed}}\right)\right| \qquad \textbf{(5.2)}$$

For patterning, we assume the beam profile as shown in Figure 5.1(a), with an ~50 nm FWHM, based on the imaging resolution, new and previously reported knife-edge measurements.[4, 146-148] Single-pass lines are produced by stepping the sample through the beam with a fixed step size of 50 nm or 200 nm, as shown in Figure 5.1(b) and Figure 5.1(c), with a per point exposure time (dwell time) ranging from 2 ms to 7.7 seconds. Longer dwell times or smaller step sizes result in a higher deposited dose and thus a greater degree of cross-linking. Wide features are patterned by exposing *n* adjacent single-pass lines, with the space between lines equivalent to the step size (50 nm or 200 nm), as shown in Figure 5.1(d). The 50 nm step size results in slight overlap between the exposed points, but the extensive reaction spread in these films causes a high degree of cross-linking between exposed points even with 200 nm point spacing, which is elucidated in later sections.

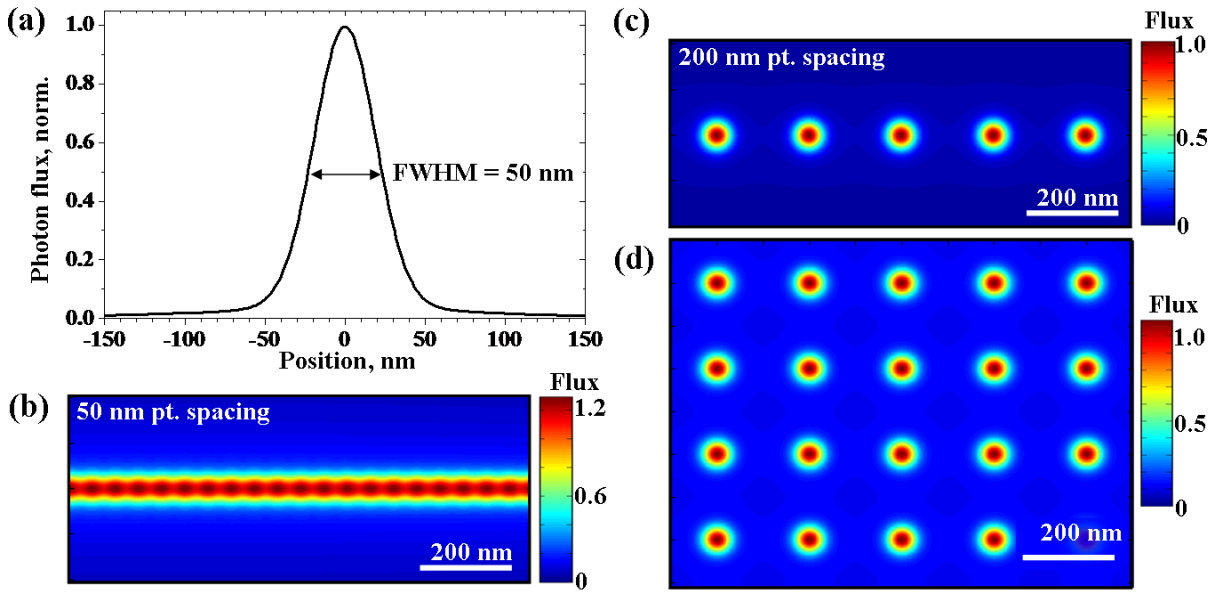

Figure 5.1 (a) Approximate X-ray beam profile. (b) Simulated direct-write X-ray lithography pattern for single-pass line with 50 nm point spacing and normalized beam profile. (c) Simulated single-pass line pattern with 200 nm point spacing and (d) adjacent, single-pass lines spaced by 200 nm.

X-ray patterning of HSQ near the oxygen K-edge involves a resonant or near-resonant absorption, so the absorbed dose is calculated by:

$$a = FEt / m\varepsilon \qquad \textbf{(5.3)}$$

where a is the absorbed radiation in units of megagrays (MGy) (1 MGy = 10^6 J kg^{-1}), F is the flux absorbed (photons per second) at energy E in exposure time t of a specific irradiated volume of the HSQ with mass m, and ε is the photon counting efficiency of the detector at energy E (57 ± 5% at 536 eV). The mass is calculated from the irradiated area, sample density and thickness. The sample density for non-cross-linked HSQ is assumed to be within the range 1.3-1.5 g/cm^3.[149] The film thickness is estimated for each patterned region by fitting the oxygen K-edge NEXAFS spectrum to the calculated spectrum per nm thickness of HSQ,[82, 118, 150] referred to as the "OD 1 nm" spectrum, shown in Figure 5.2(a). In this way, the local film thickness is determined to within better than ±15 % (e.g. ±50 nm for 300-400 nm thick films), with the error bars due to uncertainties in film density and noise in the measured spectra. Spin-coating on silicon nitride membranes does not result in uniform thin films (visible in Figure 2.17(a) as a slight variation in film color), so the membrane-supported films in this study always have a small gradient in thickness of ~10 nm per 20 μm lateral distance across the film. The NEXAFS spectrum is measured less than 10 μm away (laterally) from each region of the film to be studied, which is repeated both above and below the region (often on both left and right hand sides, as well) to get an accurate estimate of the film thickness of each region. For comparison, Figure 5.2(a) also shows the OD 1 nm spectrum for silicon nitride (Si_3N_4) (density of 3.44 g/cm^3), and the calculated Si K-edge spectra for 100 nm thick HSQ and silicon nitride are shown in Figure 5.2(b). The uncertainty in each quantity in equation 5.3 is propagated through and reported for all dose values.

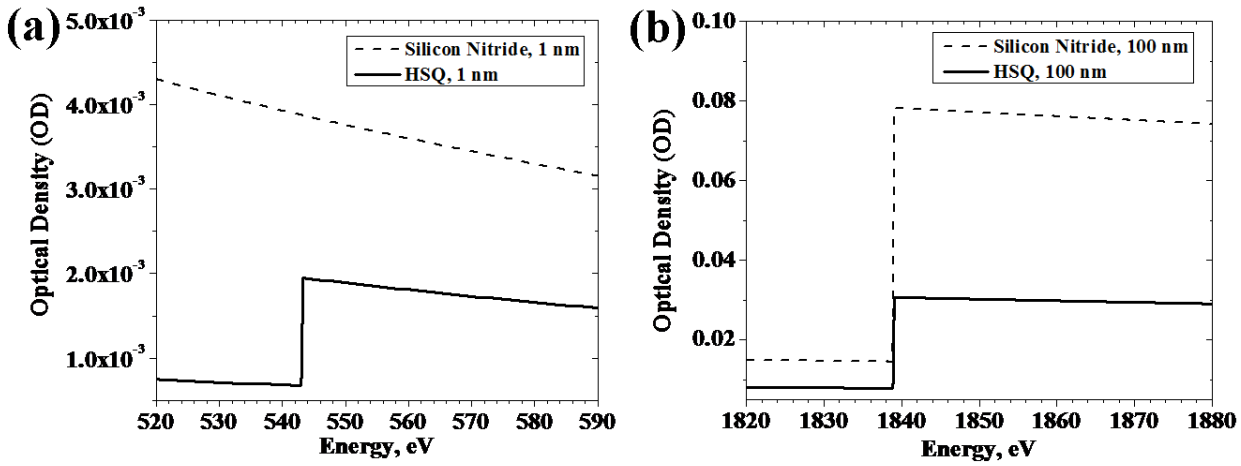

Figure 5.2 Calculated optical density of HSQ and silicon nitride for (a) 1 nm thickness at the oxygen K-edge and (b) 100 nm thickness at the silicon K-edge.

For exposure at 580 eV, the optical density changes very little with exposure time, so the absorbed flux, F, is taken as the difference between the flux through the blank substrate (I_0) and the flux through the unexposed sample (I),

$$F = I_0 - I\,. \tag{5.4}$$

However, for 536 eV exposure, the OD changes with exposure time, necessitating that the absorbed flux be calculated according to:

$$F = I_0\left[1 - \exp(-OD(t))\right] \tag{5.5}$$

where empirical data are used to fit the OD versus exposure time. For ease of comparison to dose values in the literature for EUV lithography, the areal dose is also calculated by:

$$D = FEt / A\varepsilon \tag{5.6}$$

where D is the absorbed radiation dose in units of mJ/cm^2, and A is the irradiated area, which does not account for differences in sample thickness.

Within 5 minutes of X-ray exposure, the patterned regions are imaged at 536 eV with enhanced resolution (~30 nm) at reduced X-ray flux by decreasing the monochromator slit widths and dwell times. The X-ray beam exposure can cause the HSQ to cross-link, but images can be obtained without significant additional cross-linking by minimizing the radiation absorbed during imaging. For patterning, the slit width, dwell time and step size results in a total absorbed dose of 0.4 to 300 MGy, while images are obtained with a 15 nm step size in one direction (to achieve high resolution) and 100 nm step size in the other direction (to minimize the absorbed dose), with narrower slits (40 μm, 20 μm, and 20 μm) and dwell times of less than 1 ms, for a total dose of less than 0.1 MGy. For regions with less than 0.1 MGy absorbed dose, no increase in contrast could be measured with the STXM, confirming that little or no cross-linking occurs during imaging. For the oxygen and silicon edge NEXAFS spectra of exposed and unexposed regions [Figure 5.3(b) and Figure 5.3(d)], a sequence of images, called an "image stack," is measured across an X-ray exposed feature at several wavelengths, where the same image is repeated at successively higher energies (shorter wavelengths) to construct a spectrum for each area of the image.[120] For these spectra, the additional exposed dose is on the order of 3 MGy, which induces a small but measureable amount of additional cross-linking across the entire region imaged.

After X-ray exposure and imaging, patterned films are developed for 4 minutes at room temperature in a high contrast developer solution of 1 wt% NaOH and 4 wt% NaCl in Millipore water to wash away the unexposed material.[151] The developed patterns are subsequently imaged with a field emission scanning electron microscope (SEM, JEOL JSM 6340F) and again with the STXM.

5.3 Oxygen and Silicon K-edge NEXAFS spectra of X-ray exposed HSQ

The oxygen K-edge NEXAFS spectrum of a pre-baked, 525 ± 50 nm thick unexposed HSQ film, shown in Figure 5.3(a), is obtained by defocusing the X-ray beam to a spot size of 20 μm (total dose $\sim 0.02 \pm 0.01$ MGy). A small peak is observed at 536.1 ± 0.1 eV, on the shoulder of a broader peak centered at approximately 538.8 eV. The X-ray beam is then focused on the film and the spectrum is repeated, resulting in a total of 808 ± 213 MGy absorbed dose during the spectral acquisition (from 520 to 600 eV); this results in a pronounced decrease in OD at 535.9 ± 0.1 eV, along with an increase in the broader peak and post-edge OD (for example, at 590 eV), as shown in the difference spectrum in Figure 5.3(a). However, the absorbed dose is not the same for each energy point in the "exposed" spectrum, as the absorption accumulates throughout the spectral scan. Therefore, additional oxygen edge spectra are presented in Figure 5.3(b) for a uniform exposure at a consant X-ray energy. For these spectra, a small region ($0.5\ \mu m^2$) of an unbaked 300 ± 50 nm film is exposed to an X-ray dose of 47 ± 15 MGy at 580 eV. An image stack is subsequently acquired of the exposed region and the surrounding film, during which both regions absorb 3 ± 1 MGy of additional dose. The NEXAFS peak positions in Figure 5.3(b) agree within error to those in Figure 5.3(a), and variations in the line shape are attributed to differences between the two samples, including sample type, sample age, pre-bake conditions and exposure parameters.

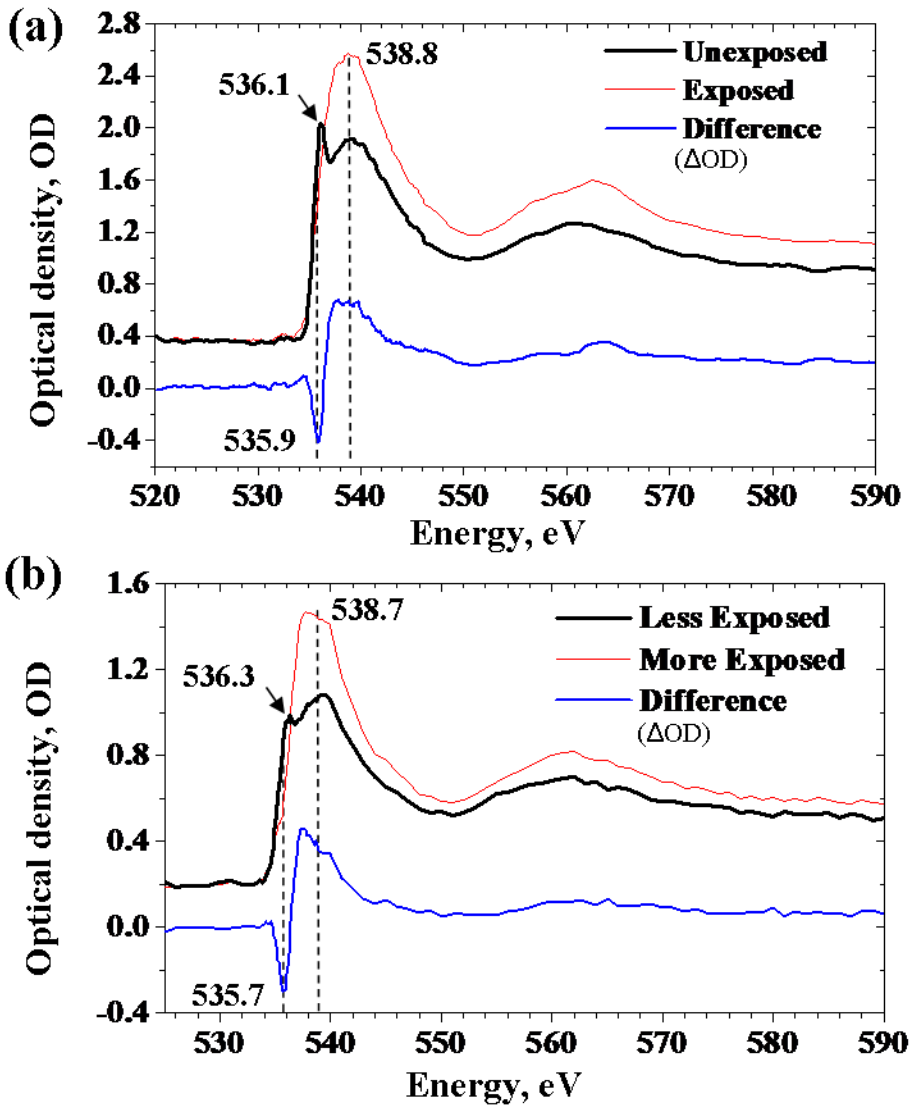

Figure 5.3 HSQ thin film NEXAFS spectra. (a) Oxygen K-edge NEXAFS spectra of a 525 nm thick HSQ film before (unexposed) and during (exposed) a 808 ± 213 MGy dose X-ray exposure near the oxygen edge. The large decrease in OD at 535.9 eV and increase at 538.8 eV are attributed to X-ray induced cross-linking, as well as an ~30% increase in total oxygen content, for example by comparing the OD at 520 eV (pre-edge) vs 590 eV (post-edge). (b) Similar peak shifts and a smaller increase in oxygen content observed between regions with 3 ± 1 MGy and 50 ± 15 MGy of exposure, respectively, near the oxygen edge (580 eV) in an ~300 nm thick HSQ film.

Very similar oxygen K-edge NEXAFS spectra were previously reported for unexposed versus e-beam cross-linked HSQ films,[50] and we attribute the spectral modifications to a change in bonding character around the oxygen atoms in HSQ due to X-ray induced polymer network formation (cross-linking). The broad absorption band at ~539 eV grows in as the HSQ cross-links to a more SiO_2-like structure, due in part to an increase in the $1s \rightarrow \sigma^*(O-Si)$ absorption previously assigned at this energy for SiO_2.[152-153] The broad band at ~562 eV present before and after cross-linking is due to a "shape resonance" of this same transition.[116, 152-154] However, the broad 539 eV peak has also been previously assigned to adsorbed water multilayers on various surfaces.[155-156] Additionally, the NEXAFS spectra in Figure 5.3(a) show that the total oxygen

content within the exposed regions increases by ~30% after an 808 MGy exposure, as evidenced by the increase in the X-ray absorption at energies beyond the oxygen edge, from 550 eV-590 eV. Comparing two regions with a smaller difference in dose (3 MGy versus 50 MGy), a smaller increase in oxygen content is observed [Figure 5.3 (b)], so the amount of additional oxygen is dose dependent; this was confirmed all the way out to 650 eV (not shown). This added oxygen could be incorporated into the network during cross-linking, according to the mechanism at the top of Figure 4.6, but could also be additional adsorbed water on the surface and within the pores of the HSQ in cross-linked regions, due to the decreased hydrophobicity and pore size of the network structure. The minimum vacuum pressure of 0.2 Torr used in the STXM chamber is sufficient to maintain many monolayers of water on the film surface and within the chamber itself, and water is also mobile within the porous HSQ network (in cross-linked HSQ, diffusion coefficient of $H_2O \approx 3.61 \times 10^{-10}$ cm^2/s).[157] Much lower vacuum pressure is required to remove the water to below one monolayer; comparison to NEXAFS spectra at lower pressure would potentially elucidate the role of water in the cross-linking mechanism.

Assigning the side peak at ~536 eV is less straightforward, as it is nearly buried under the much broader 539 eV absorption, and a precise peak assignment in this region is unknown. However, absorption peaks at 534.4 eV-535.5 eV have been reported for O-H species in different environments, including the $1s \rightarrow 4\sigma^*(O-Si)$ transition in ≡Si-OH on the surface of silicon oxide nanowires[158] and for the same transition in OH^- chemisorbed on NaCl.[159] Therefore the 536 eV peak is tentatively assigned to ≡Si-OH, where the symbol, ≡, represents all the other cage or network bonds to the Si atom. To test this peak assignment, NEXAFS spectra are obtained for compounds similar to HSQ with different substituent groups, shown in Figure 5.4. The oxygen K-edge spectrum was measured for methyl silsesquioxane (MSQ) in its pure, powdered form (PSS-octamethyl substituted, Sigma Aldrich), which is identical to pure HSQ except with all the ≡Si-H groups on the corners of the HSQ cage replaced by ≡Si-CH_3, and compared to the spectrum of solubilized MSQ (polymethylsiloxane in ethanol, Techneglas, Inc.), where a small percentage of the ≡Si-CH_3 groups are replaced by ≡Si-OH. In MSQ samples with ≡Si-OH, the observed line shape is very similar to the unexposed HSQ spectrum [Figure 5.3(a)], with a sharp peak at 536.7 ± 0.1 eV followed by a broader peak at 538.7 ± 0.1 eV. However, for the pure MSQ samples without ≡Si-OH, the broad band is the same, but the sharper 536.7 eV peak is not observed. This suggests that the 536.7 eV absorption peak in the solubilized MSQ results from the oxygen in the ≡Si-OH bonds, and that the ~536 eV peak in the unexposed HSQ is likewise due to ≡Si-OH present in the HSQ film prior to cross-linking. While there is some uncertainty in this peak assignment due to the possibility of other slight structural differences in the commercially prepared samples, this assignment is consistent with the fact that HSQ without any ≡Si-OH has poor solubility in most solvents, and thus a small amount of ≡Si-OH must be incorporated to increase its solubility for spin-on applications.[132, 143-144] The decrease of this ≡Si-OH associated peak during cross-linking shows that the existing ≡Si-OH groups play an important role in the X-ray induced cross-linking mechanism under these conditions, consistent with the proposed e-beam mechanism illustrated in Figure 4.6.[37]

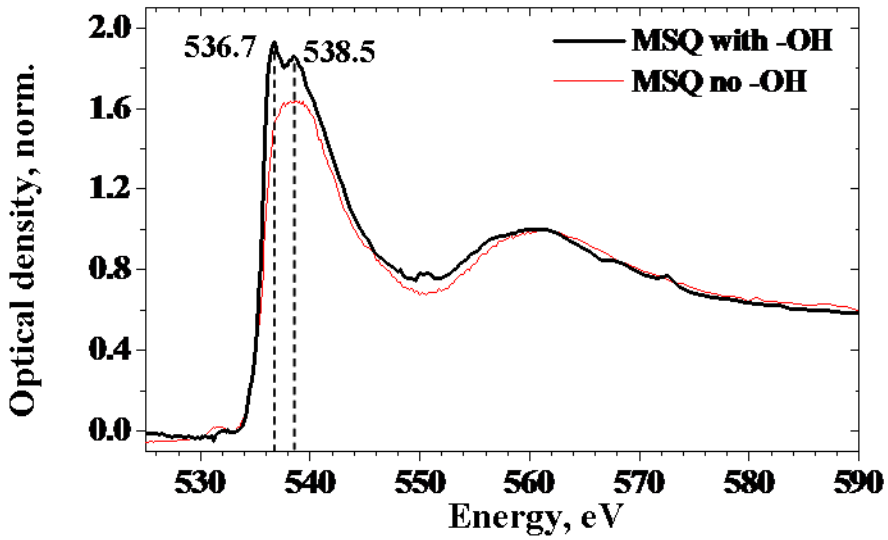

Figure 5.4 Spectra for pure MSQ with no ≥Si-OH, compared to MSQ with incorporated ≥Si-OH. The similarity in peak structure to the spectra in Figure 5.3(a) and (b) suggests that the ~536 eV peak in the unexposed HSQ is due to ≥Si-OH incorporated in the HSQ stock solution.

In addition to oxygen edge spectral measurements, the silicon K-edge spectrum of HSQ is obtained for a similar sized region exposed to >0.5 MGy (>17 mJ/cm^2) at 540 eV (precise dose not determined), shown in Figure 5.5. The image stack method used to acquire these silicon K-edge spectra results in an additional dose across both the unexposed and exposed regions. The NEXAFS spectra reveal no measureable change in the total silicon content of the exposed region for the dose used, evidenced by no change in the post-edge absorption intensity. (However, it is estimated that the X-ray dose used for this spectrum is lower than in Figure 5.3(a) and (b), possibly too low for changes in Si content to be apparent in the NEXAFS spectrum.) A distinct decrease in the optical density at 1845.4 ± 0.3 eV and an increase at 1847.6 ± 0.3 eV are observed in the areas that have absorbed >0.5 MGy of X-rays, which are attributed to changes in the silicon bonding character after cross-linking. The increasing peak at 1847.6 is due to an increase in SiO_2-like bonds, likely the $1s \rightarrow \sigma^*(Si-O)$ absorption previously assigned in various SiO_2 samples at ~1847 eV.[152, 160-161] The decreasing absorption at 1845.4 eV is likely due to a decrease in ≥Si-OH bonds after exposure, based on previous studies of porous silicon, SiO_2,[160, 162] and siloxene.[161] Notably, we do not see any feature at 1838-1840 eV before or after cross-linking, which would indicate Si-Si bonds,[160] suggesting that significant Si-Si bond formation does not occur at this X-ray dose. Although these spectra are acquired with a slightly different exposure wavelength and lower dose than for the oxygen spectra in Figure 5.3, they demonstrate that the X-ray induced chemical change affects both the silicon and oxygen bonding structure, as expected for polymer network formation. The spectral peak positions and intensities before and after X-ray exposure look very similar to reported NEXAFS spectra for powdered HSQ solids before and after heating at 500 °C,[163] indicating a similar network structure for the heated and X-ray exposed HSQ.

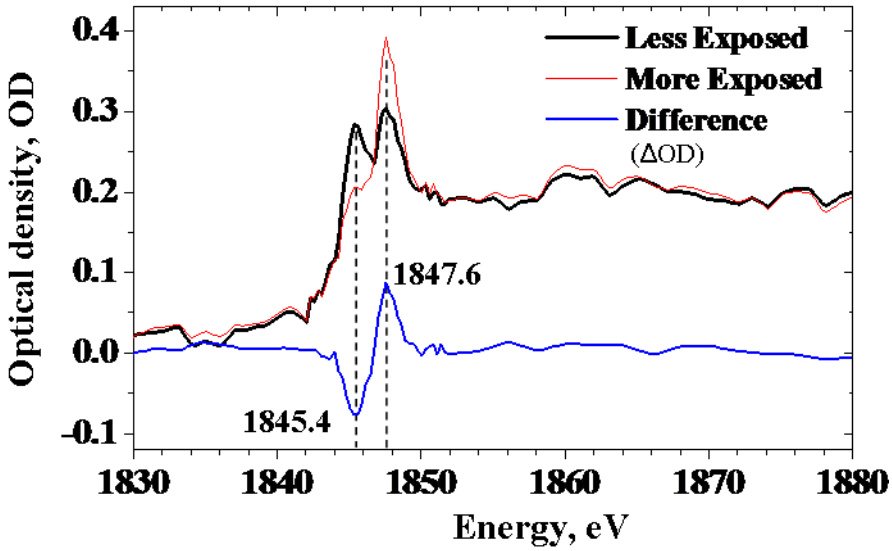

Figure 5.5 Silicon K-edge NEXAFS spectra HSQ film (~250 nm thick), showing a decrease in OD at 1845.4 eV and an increase at 1847.6 eV after >0.5 MGy X-ray exposure at the oxygen edge (540 eV), indicating an increase in SiO_2-like structure but no change in total silicon content.

5.4 X-ray induced cross-linking reaction rate

The change in the NEXAFS spectra between exposed and unexposed HSQ is a measure of the structural transformation due to the chemical reaction. After patterning HSQ thin films with the X-ray beam, the patterned area is imaged at 536 eV. There is no further sample modification prior to this imaging, such as development in solution; the contrast at each spatial location in the image is calculated in ΔOD (Eq. 5.2), which quantifies the relative degree of cross-linking in the exposed vs. unexposed areas. The sensitivity is defined here as the increase in contrast per unit of absorbed X-ray dose. These definitions of contrast and sensitivity are based solely on the photochemical characteristics of the HSQ thin films, but are analogous to those typically used for lithography, which are based on developer effects.[2] The relation of the unexposed contrast and sensitivity to the development effects are discussed in section 5.6.

To examine the X-ray exposure sensitivity of HSQ and relate contrast (ΔOD) to the degree of cross-linking, the HSQ films are patterned at increasing dose and then imaged, shown in Figure 5.6(a). Equal-sized 1 μm × 5 μm features are exposed in a pre-baked, 500 ± 50 nm thick HSQ film by direct-write X-ray patterning, in this case at an energy of 536 eV, at doses from 2.0 ± 0.4 to 276 ± 57 MGy. The spacing between exposure points within each feature is 200 nm, features are separated by 1 μm, and the dwell time is increased exponentially for each subsequent feature. The patterned area is subsequently imaged at 536 eV, and the X-ray transmission through each feature is shown in Figure 5.6(a), where the line profile indicates the average contrast through the shaded region highlighted by the bold arrows, and the black spots are clusters of 100 nm gold nanoparticles on the film surface (used for focusing). Though the point spacing is 200 nm, the individual exposed points are not observed within each feature due to significant spreading of the cross-linking reaction beyond the 50 nm exposure beam width, which is explained in detail in the subsequent section. The contrast between the exposed and unexposed regions, which is a measure of the relative degree of cross linking, is plotted versus

dose and dwell time in Figure 5.6(b), showing a sub-linear increase in cross-linking with dose. The contrast values plotted in Figure 5.6(b) are obtained by averaging the contrast across the central 80% of each feature, excluding any nanoparticles.

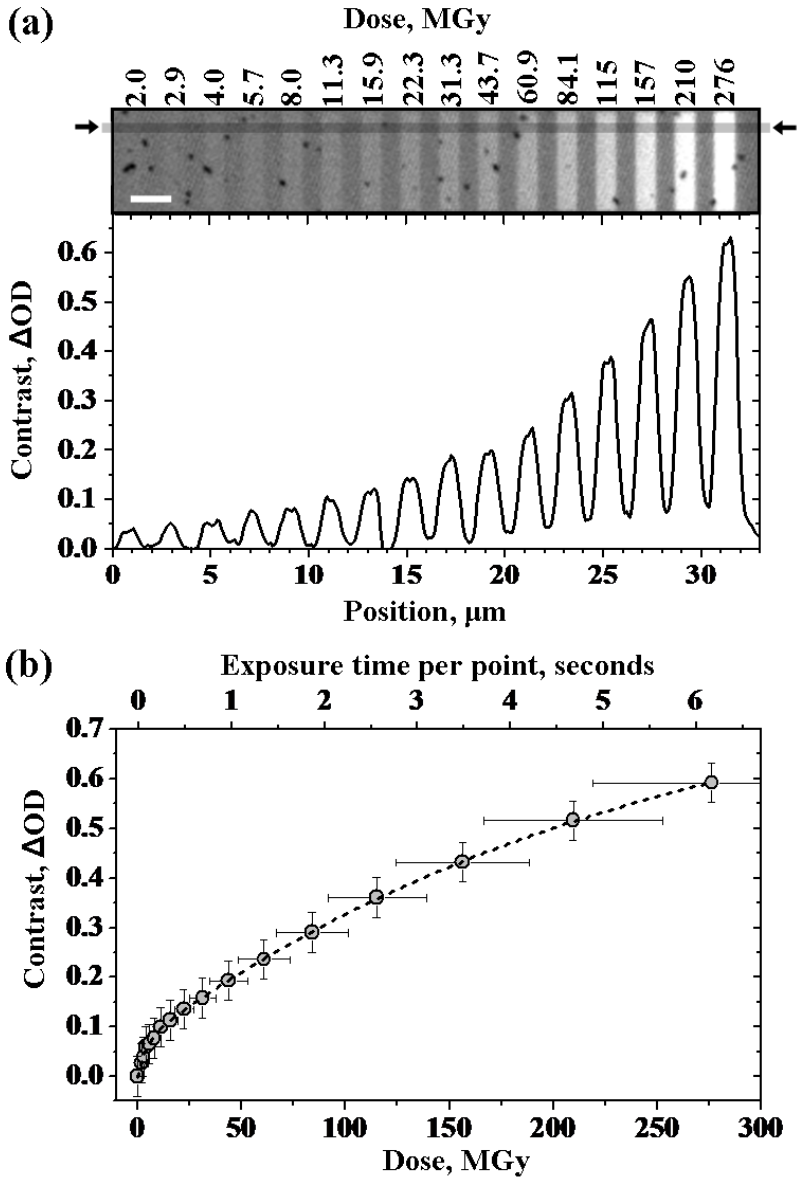

Figure 5.6 X-ray sensitivity of undeveloped HSQ thin film (500 ± 50 nm thick). (a) STXM image (transmission) and line profile (ΔOD) at oxygen K-edge (536 eV) of equal sized features exposed with increasing X-ray dose at 536 eV, using 200 nm exposure point spacing. The line profile plot is the average contrast through the narrow region of the image indicated by the grey bar. Lighter regions indicate more transmission due to higher degree of cross-linking, and dark points are clusters of 100 nm gold nanoparticles, used to focus the X-ray beam. Scale bar = 2 μm. (b) Plot of average ΔOD of each entire feature (excluding nanoparticles) versus X-ray dose, showing onset of cross-linking at very low dose and sub-linear dose dependence of cross-linking degree. Horizontal error bars are for the MGy axis only. Dashed line fit is $\Delta OD = 0.85 - 0.067\exp(-a/4.2) - 0.782\exp(-a/247)$, where *a* is dose in MGy, which can be recast to $\Delta OD = 0.85 - 0.067\exp(-t/0.09) - 0.782\exp(-t/5.5)$, where *t* is exposure time per point in seconds, indicating two stages of cross-linking and a maximum contrast of ΔOD ≈ 0.85.

The double exponential curve fit in Figure 5.6(b) indicates a two-stage cross-linking process, with a fast initial step with $\tau_1 = 0.09 \pm 0.01$ s and a much slower second stage with $\tau_2 = 5.5 \pm 0.3$ s. Just as reaction rates typically depend on temperature or laser power, these time constants vary based on the rate of energy absorption, or absorbed dose rate; here the incident flux is ~1.6 x 10^6 photons/s, corresponding to an absorbed dose rate of approximately 42 MGy/s. The fit shows that the cross-linking can continue well beyond the maximum dose used here of 276 ± 57 MGy (19,339 ± 3203 mJ/cm^2), up to a maximum contrast of $\Delta OD \approx 0.85$ for the fully cross-linked material. Assuming that $\Delta OD = 0 - 0.85$ corresponds to 0 - 100% relative degree of cross-linking, an increase in contrast of $\Delta OD = 0.1$, for example, equates to an increase in the degree of cross-linking of 11.8 ± 4.2 % out of the possible cross-linkable sites. A linear fit of the lowest-dose points in Figure 5.6(b) gives an initial sensitivity of 1.1 ± 0.4 % cross-linking increase per MGy X-ray dose, while the highest-dose points give a final sensitivity of 0.19 ± 0.07 % per MGy. Thus the initial, fast cross-linking corresponds to higher sensitivity, and the slower cross-linking is equivalent to lower sensitivity.

This double exponential decay in the cage-like species is analogous to the NIR MAP mechanism of HSQ, where the slower cross-linking reaction rates ($\tau_1 = 30 \pm 10$ s and $\tau_2 = 3 \pm 1$ min, section 3.3)[79] are presumably due to a lower dose rate and possibly a different mechanism. As mentioned previously, one explanation for the two time stages is that as reactive sites are generated photolytically in the solid film, nearby sites react quite readily, but the rigidity of the network increases with cross linking. This slows the rate of additional cross-linking due to the restricted mobility of the remaining reactive sites, which are locked into the polymer network configuration. Another way of saying this is if there are some bonds with more favorable kinetics for cross linking due to juxtaposition or angular geometry, these may cross-link first, giving the initial faster cross-linking rate, which slows as these sites are used up.

5.5 Area dependent sensitivity

For the increasing dose features in Figure 5.6(a), no significant increase in cross-linking is observed in between features at low dose, but an increasing background level of cross-linking is measured in between the adjacent features starting at a dose of 22.3 MGy (1563 mJ/cm^2, position ~16 μm), indicating that increased cross-linking occurs well outside the exposed region. To the right of the highest dose feature, an increase in cross-linking giving $\Delta OD \approx 0.03$ is observed more than 1 μm beyond the exposure boundary, which is nearly the amount of cross-linking observed at the center of the 2.0 MGy exposed feature. This extensive diffusion of the polymer cross-linking is consistent with previous STXM and FTIR imaging of undeveloped e-beam exposed HSQ films, where a small but measurable increase in cross-linking was observed at distances greater than 12 μm away from the e-beam exposed regions at very high doses.[50, 68]

Based on previous reports with HSQ, some area dependent contrast is expected,[8, 51] defined here as an increase in peak contrast as the feature size increases, despite a constant absorbed dose. This can be interpreted as a higher sensitivity for the larger features, because to obtain features with an equivalent peak degree of cross-linking (a requirement for some lithography applications[2, 8]) would require decreasing the dose significantly for larger features. The amount of peak contrast is highly dependent on the overlap between exposed points,[51] but likewise should depend on the overlap of regions cross-linked by reaction spread beyond the

exposure boundary. To examine how the lateral reaction spread contributes to the area dependent sensitivity, a set of features with different sizes are patterned at constant dose of 8.6 ± 1.4 MGy (484 ± 44 mJ/cm^2) in an unbaked, 400 ± 50 nm thick HSQ film, then imaged at 536 eV, shown in Figure 5.7(a). The first feature on the left in Figure 5.7(a) is a single-pass line exposure of the X-ray beam at 580 eV with 50 nm point spacing, and the exposed width of the features is increased going to the right, up to 1.5 μm wide for the right-most feature, made by 30 adjacent single-pass lines separated by 50 nm. Figure 5.7(b) is a plot of the increase in the peak contrast versus exposed feature width [from Figure 5.7(a)]. There is only a slight overlap between adjacent point exposures within each feature, so only a small increase in peak cross-linking is expected with feature width, shown as the bottom dashed line (black) in Figure 5.7(b); however, the data clearly shows a much stronger area dependence. Furthermore, the measured FWHM of the single line exposure in Figure 5.7(a) is 360 ± 50 nm, showing a spread of cross-linking of at least 150 nm laterally from the edges of the exposure beam. The upper dashed curve (gray) in Figure 5.7(b) simulates the peak degree of cross linking expected with a 360 nm beam width, which more closely resembles the observed measurements. The simulated curves are for isolated features with 50 nm point spacing at ~8.6 MGy, using the exposure beam profile in Figure 5.1(a) (50 nm or 360 nm FWHM) and the HSQ sensitivity from Figure 5.6(b). The observed increase in peak cross-linking is even higher than the wider-beam simulation because of the long tail of the cross-linking spread, which causes increased overlap between features that are too closely spaced (evidenced by the increasing background in between features in Figure 5.7(a)). Note that the integrated intensity of the line profiles for the data and simulations here show that the total degree of cross-linking is approximately linear with increasing feature width.

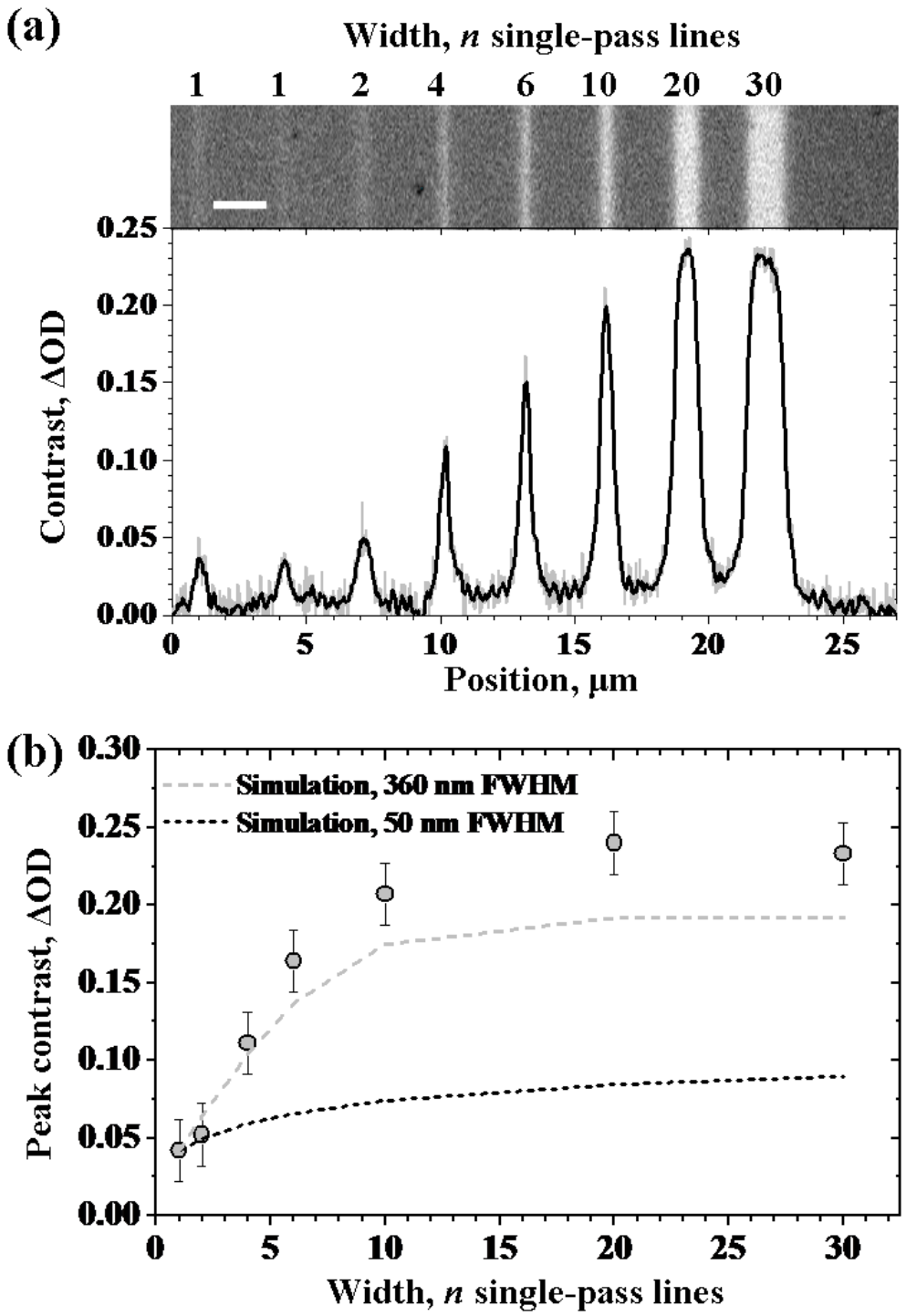

Figure 5.7 Area dependent sensitivity observed for X-ray cross-linking of HSQ. (a) STXM image (transmission) and line profile (ΔOD) at oxygen K-edge (536 eV) of increasing size features patterned at constant X-ray dose (8.6 ± 1.4 MGy). Features range from a single-pass line up to a 1.5 μm wide bar, with 50 nm point and line spacing within each feature. The average FWHM of the single-pass lines is 360 ± 50 nm. Scale bar = 2 μm. (b) Plot of peak contrast in image above, showing area-dependent sensitivity. The lower dashed line (black) is the expected peak contrast based on the actual exposed area, showing that the observed increase in peak cross-linking far exceeds that expected based on the exposure profile (Figure 5.1(a)), due to spreading effects. The upper curve (gray) is simulated using a single-pass line width of 360 nm, as measured.

The strong area-dependence of the peak contrast is attributed to the spread in the cross-linking beyond the exposure boundaries. As the pixel spacing is significantly less than the distance of the reaction spread, each adjacent line within a feature will overlap previously cross-linked material, and the peak of the cross-linking will accumulate to a higher degree than anticipated based on the absorbed dose alone. The peak contrast levels off at a width of approximately 10 single-pass lines, because once the feature is significantly wider than the reaction spread, the overlap between partially exposed regions becomes primarily an edge effect. Interestingly, for cases up to 10 adjacent single-pass lines, the area dependence of the peak contrast is also approximately linear, as previously reported for area dependence measurements in ultra-thin, e-beam patterned and developed HSQ.[51] Preliminary results suggest that the area dependence and linewidth vary somewhat with the delay time between film preparation (spin-coating) and exposure, as do the film contrast and sensitivity, consistent with previously published studies of e-beam patterning in HSQ.[2, 48-49, 164]

This proximity effect is also extremely important for small features that are closely spaced. To demonstrate this, adjacent pairs of single-pass lines are written at various distances apart (125 nm to 2 μm) at three different doses from 7.2 to 28 MGy (405 to 1590 mJ/cm^2). As shown in Figure 5.8, even at the lowest dose of 7.2 ± 1.5 MGy, the overlap between adjacent lines is so significant that the two separate lines can not be discerned until they are separated by at least 500 nm. At all doses, adjacent lines must be spaced by >1 μm in order to prevent some overlap and measurable latent contrast in between adjacent features. The simulated data in Figure 5.8(b) shows that well separated lines are expected if the reaction does not spread beyond the exposure boundaries, based on the X-ray exposure beam profile and HSQ sensitivity. For comparison, the simulated data in Figure 5.8(c) shows that a reaction spread of 390 nm for a single-pass line (FWHM) approximately matches the measured feature profiles, but with slightly higher peak contrast, possibly due to uncertainty in the exact shape of the reaction spread profile.

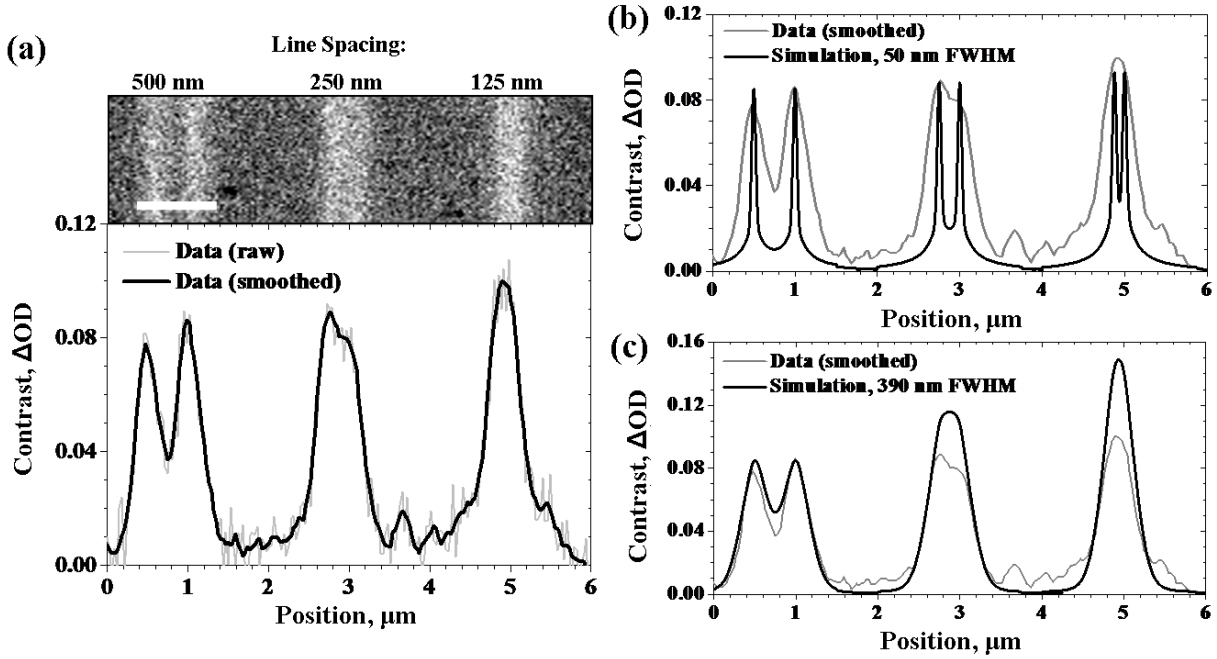

Figure 5.8 Proximity effects measured for pairs of single-pass lines separated by different distances at constant dose, 7.2 ± 1.5 MGy (point spacing = 50 nm), shown in STXM image (top) and line profile (bottom) at the oxygen K-edge (536 eV). Gray profile is raw data, black is smoothed. The more closely spaced lines cannot be discerned due to the reaction spread. Scale bar = 1 μm. Profiles at right show simulated lines (black) overlaid on smoothed data (gray) for (b) 50 nm exposure beam profile (FWHM) and (c) 390 nm beam profile, indicating that reaction diffuses outside of the 50 nm wide exposed region to a FWHM of ~390 nm. Peak contrast and linewidth cannot be fit simultaneously, possibly due to uncertainty in the reaction spread profile.

5.6 Quantifying reaction spread

Based on the results in Figure 5.6, Figure 5.7, and Figure 5.8 and previous studies of undeveloped e-beam patterns in HSQ,[50, 68] it is apparent that the spatial extent of the reaction spread depends upon the exposure dose. Since the proximity effects in Figure 5.7 and Figure 5.8 are determined by how far the reaction spreads from each exposed point, the dose dependence of this spread needs to be well defined for useful lithography in order to achieve the desired degree of cross-linking for a given feature size, as it relates to the final height of the developed features. To measure the extent and shape of this spread with good signal-to-noise, many sets of single-pass line exposures with doses from 0.4 to 111 MGy are produced (50 nm point spacing, 580 eV exposure), and these sets of lines are repeated many times in different films which are 100-400 nm thick. Figure 5.9(a) shows the raw X-ray transmission image for a set of undeveloped, X-ray exposed lines in a 330 ± 50 nm thick HSQ film after patterning, and line profiles, vertically averaged along the full length of each line in ΔOD, which are used to obtain the FWHM. The FWHM of all the undeveloped single-pass lines are shown in Figure 5.9(b), where each point is the mean line width of 2-5 independent lines patterned at that dose. These lines are, of course, substantially wider than in recent state-of-the-art HSQ lithography (4.5 to 20 nm line width),[1-2, 55] due to the film thickness and 50 nm FWHM exposure beam, as well as the delay between baking and exposure,[2, 48-49, 164] and possibly due to the ~2 year storage of the HSQ stock solutions.[48] The

area, dose and thickness dependent trends observed here agree with trends reported for thin HSQ e-beam and photo-lithography.[2]

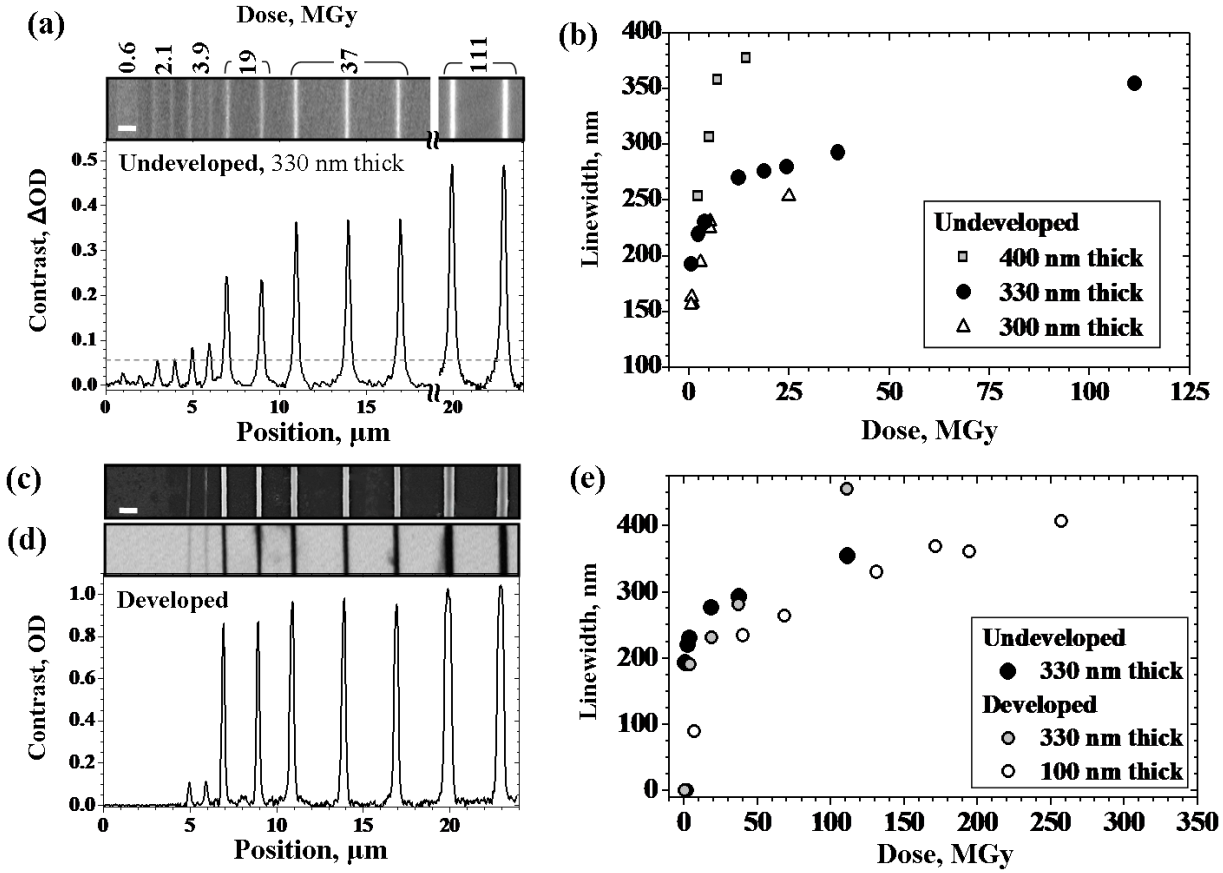

Figure 5.9 Single-pass lines used to quantify the diffusion of the cross-linking reaction. (a) STXM image (transmission) and line profile (ΔOD) at oxygen K-edge (536 eV) for undeveloped lines exposed at doses from 0.6 ± 0.3 to 111 ± 29 MGy with 50 nm point spacing. Small gap in image and plot is where no data was taken. All cross-linked material below the dashed line was washed away by subsequent development. (b) Plot of undeveloped line widths, FWHM, showing a strong dependence of the width on both dose and sample thickness. Narrowest lines are in ~300 nm thick films (open triangles). An increase in line width is observed in ~330 nm thick films (filled circles) and 400 nm thick films (gray squares). (c) SEM image and (d) STXM image (transmission) with line profile (OD) at 536 eV of the same lines after development, showing the onset of developer at an exposure dose of 3.9 ± 1.0 MGy. Note that the absolute contrast in this plot cannot be compared with the contrast in (a), as the unexposed film has been washed away by the developer. (e) Plot comparing developed (gray circles) and undeveloped (black circles) line widths, FWHM from STXM data in ~330 nm thick film, showing similar but slightly sharper line widths after development at low doses, due to removal of the partially cross-linked material at the line edges. Surprisingly, the highest dose lines (111 MGy) have a greater FWHM after development, even though they are narrower at the base. SEM measurements of developed lines in 100 nm thick films (open circles) are considerably narrower, continuing the trend of narrower lines in thinner films. Scale bars = 1 μm.

Figure 5.9(b) shows that there is a substantial spread in the HSQ cross-linking beyond the exposed region in the undeveloped films, which increases with exposure dose and with film thickness. For the ~300 nm thick films, the minimum possible line width is 157 ± 5 nm, compared to 190 ± 7 nm for the ~330 nm thick films, and 223 ± 27 nm for the ~400 nm thick films, determined by fitting a line through the low dose points only and extrapolating to zero

dose. This increase in line width with film thickness is consistent with recently published results for very thin, developed HSQ.[51, 165] Taking into account the three-dimensional spread of the reaction upon exposure, one possible explanation for the greater reaction spread with thicker films is that the process responsible for the reaction spread is inhibited by the surface of the film. In addition to this thickness dependence, the spread in the reaction increases with dose, as expected.[51] For example, in the 330 nm thick film, the linewidth averages 193 ± 40 nm FWHM at the low dose of 0.6 ± 0.5 MGy, up to 355 ± 7 nm at a dose of 111 ± 29 MGy, corresponding to a spread of 70-150 nm on either side of the exposure beam profile at the FWHM. Note the two-stage shape of the increase in linewidth with dose, as the linewidth initially increases very sharply with dose, then the rate of linewidth increase slows considerably with additional dose, even up to very high doses. This indicates two different possibilities, which are not mutually exclusive; it could indicate a maximum range for the diffusing species or chain reaction, or it is also consistent with the double exponential decay mechanism mentioned above (Figure 5.6), where the initial cross-linking sensitivity of the HSQ to diffusing species is very high, but the cross-linking effectiveness decreases once a certain degree of cross-linking has been reached.

For comparison, Figure 5.9(c) shows an SEM image of the same set of lines [from Figure 5.9(a)] after room temperature development in 1% NaOH + 4% NaCl. Figure 5.9(d) shows the STXM transmission at 536 eV of these developed lines and the line profile of this image converted to OD. The single-pass lines exposed at low doses, 0.6 ± 0.3 and 2.1 ± 0.6 MGy, are removed by the developer, while the features at 3.9 ± 1.0 MGy (181 ± 37 mJ/cm^2) dose are just visible. Following the typical definition of onset dose (D_i, the minimum dose for which the cross-linked resist is insoluble in the developer), this corresponds to an onset dose of ~3.9 MGy (~181 mJ/cm^2), which agrees very well with the onset dose for previously reported X-ray lithography in 300 nm thick HSQ films of $D_i \approx 200$ mJ/cm^2 (in TMAOH developer).[41]

Figure 5.9(e) is a plot of the FWHM of these undeveloped and developed lines, which shows that the developed lines are just slightly narrower at low doses. However, at a high dose of 111 MGy, the FWHM of the developed lines are actually ~30% wider, even though these lines are still narrower at their base after development. In addition, the 90 ± 14 nm wide lines at 7.1 ± 2.4 MGy (100 ± 32 mJ/cm^2) in the developed 100 ± 20 nm thick HSQ film are plotted in Figure 5.9(e), continuing the observed trend of narrower lines in thinner samples beyond the minimum thickness accessible by latent STXM imaging. The dashed line in Figure 5.9(a) corresponds to the cutoff in latent contrast below which the developer removes all material, which is at a ΔOD value of 0.06 ± 0.02. The developed lines have a slightly different line shape because the material below this critical cross-linking degree (ΔOD ≈ 0.06), at the edges of the lines near the base, is removed by the developer. This narrowing of the lines is expected based on studies of the developer activity,[166] but detailed line profiles of the undeveloped material were not accessible in that work. By assuming that ΔOD = 0 - 0.85 corresponds to 0 - 100% relative degree of cross-linking [Figure 5.6(b)], the critical cross-linking degree for development contrast (ΔOD=0.06) corresponds to an increase in the degree of cross-linking of just 7.1 ± 2.5 % out of the possible cross-linkable sites. Previous FTIR studies of HSQ thin films approximate the minimum and maximum possible conversion degree to be 19.4% - 70%,[68] where conversion degree is defined as the ratio of ≥Si-O-Si≤ cage bonds to ≥Si-O-Si≤ network bonds. Some HSQ cross-linking occurs during film preparation, even for room-temperature preparation under vacuum,[35, 47] and the initial degree of cross-linking also depends on whether the sample is pre-baked, for how long and at what temperature,[47, 57] the delay after spin-coating, and storage atmosphere.[48-49] Importantly here, it also depends upon the age of the stock solution subsequent

to manufacture.[48] If we assume a starting cross-linking degree for the entire film of 19.4% and a maximum of 70%, based on previous FTIR work,[68] the developer onset of ΔOD=0.06 would correspond to an absolute cross-linking degree of approximately 24%. However, due to the aging and delay effects, and other variations between samples, the starting degree of cross-linking in these particular films is uncertain, likely higher than 19.4%. It is important to note that although only the relative degree of cross-linking (latent contrast) can be measured here, the onset dose of the developer also depends upon the absolute degree of cross-linking.

The line widths in Figure 5.9 were compared to the single-pass lines in Figure 5.7, and it was observed that the longer delay between film preparation and exposure used for the data in Figure 5.7 (70 hours, due to beam time constraints) resulted in significantly wider lines and lower contrast for comparable doses. Previous reports show that a delay between baking and exposure can lead to such line width broadening,[49] and that the magnitude of the contrast changes with post-bake delay can exceed the sample aging effects,[48] but the preliminary data comparison in this study suggests that the delay effect may be an issue even in these films which are unbaked. Thus, in future work the delay between spin-coating and exposure should be minimized and much more carefully controlled.

By comparing the undeveloped STXM image contrast in Figure 5.6(a) and Figure 5.9(a) with previously reported STXM images of e-beam exposed HSQ, it is possible to approximate the relationship between X-ray dose and e-beam dose. From this, we estimate that the developer onset X-ray dose of ~3.9 MGy (~181 mJ/cm^2) in this film corresponds to a 100 keV e-beam dose of approximately 8 ± 4 mC/cm^2 in a 250 nm thick HSQ film (pre-baked at 170 °C for 5 min).[50] This comparison is only an approximate frame of reference for the doses used in the current study, as there were significant differences between the sample used in the e-beam study and the present work, including the precise film thickness, exposure point spacing, sample age, delay and pre-bake conditions. Nonetheless, our onset dose of 3.9 MGy ≈ 8 ± 4 mC/cm^2 agrees within error to the previously reported onset dose of 6.5 mC/cm^2 under the same developer conditions in 115 nm thick HSQ.[151]

5.7 Potential mechanisms for cross-linking reaction spread

The main result of this work is to quantify the X-ray exposure sensitivity and reaction spread in undeveloped HSQ patterns. Since the X-ray beam position is interferometer controlled to better than 10 nm and tightly focused, and we have carefully measured and accounted for the initial (low-dose) sensitivity of HSQ, exposure effects leading to line broadening can be ruled out. One possible cause for the >70 nm lateral spread of the reaction could be reactive species diffusing through the film to the unexposed regions. Reaction spread beyond the exposure boundaries within this range has recently been reported in other X-ray patterned, thin (~40 nm), organic positive-tone photoresist materials (PMMA and PAN). The results are tentatively attributed to the propagation of radicals and/or ions through the film, but the mechanism has yet to be determined.[82] In that report, it was estimated that, given the conditions of 300 Torr of He in the X-ray exposure, heating of the films is negligible (on the order of 5 x 10^{-4} K), and that thermal damage is therefore an unlikely mechanism for the reaction spread.

As explained in section 2.3, when the soft X-ray photon at 536 eV to 580 eV is absorbed by the HSQ thin film, it excites a core electron in the sample, which decays to produce a high energy Auger electron (~500 eV) and a singly or doubly ionized valence excited state, which can

lead to the breaking of nearby bonds at a range of a few nm. This likely results in energetic and reactive radical and/or ion fragments, and secondary electrons, which can further propagate the initiation of the reaction.[82] The mean free path of scattered 0-580 eV electrons in HSQ should be similar to amorphous glass and polymers of similar density, which is less than 10 nm.[167-168] The effect of low energy secondary electrons (10-50 eV) in e-beam lithography of HSQ was shown to be limited to a range of ~2 nm.[169] Therefore we suspect that small radicals or ions are responsible for the >70 nm reaction spread through the film. The ≥Si-H single bond is significantly weaker than typical ≥Si-O-Si≤ single bonds (~4.08 eV versus ~8.95 eV each, respectively).[43] It is possible that protons or H radicals are liberated by the cleavage of the ≥Si-H bonds during the X-ray absorption, and these may be able to propagate some distance before reacting and causing cross-linking, possibly leading to a cross-linking chain reaction.

A variety of mechanisms could explain the reaction spread, and here we discuss two possibilities in more detail. Electron spin resonance (ESR) studies indicate that H radicals produced upon gamma irradiation of crystalline HSQ can travel through the solid to neighboring cages;[170-171] this species may also propagate through a silicon-based polymer (reported for poly-dimethylsiloxane, PDMS) before abstracting an additional H atom to form H_2 and a molecular radical that cross-links.[172-173] Therefore, one possibility is that H radicals produced by the X-ray induced ≥Si-H bond breaking in HSQ travel through the film to abstract H from another ≥Si-H bond 70 nm or more away, creating an additional silicon radical:

$$H^{\bullet} + \text{H-Si}\lessgtr \longrightarrow H_2 + {}^{\bullet}\text{Si}\lessgtr \qquad \textbf{(5.7)}$$

where the ≥ symbol again represents all the additional cage or network bonds on the Si atom. This silicon radical could then cross-link with a neighboring HSQ cage in a variety of ways, possibly involving the uptake of water to form a reactive silanol,[37] or cage bond redistribution,[35-36, 173] as shown in Figure 4.6. However, since the silicon radical is bound to the network, unlike the H radical, and because free radicals in solid polymers must be separated by less than ~4 Å in order to react,[174] continued spread of cross-linking by a silicon-radical induced chain reaction is less likely within the solid HSQ film. Without such a chain reaction, each H radical would initiate only one cross-linking event, and substantial cross-linking at a distance would depend upon H atoms diffusing through the film from the exposed region.

An alternative, acid-catalyzed reaction could be initiated by protons according to the following mechanism:

$$\begin{aligned} \text{≥Si-O-Si}\lessgtr + H^{\oplus} &\longrightarrow \text{≥Si-O-Si}\lessgtr \overset{H^{\oplus}}{} \longrightarrow \text{≥Si-OH} + {}^{\oplus}\text{Si}\lessgtr \\ \text{≥Si-OH} + \text{≥Si-OH} &\longrightarrow \text{≥Si-O-Si}\lessgtr + H_2O \end{aligned} \qquad \textbf{(5.8)}$$

Subsequently, the proton is regenerated by reaction of the silicon cation with moisture, which subsequently gives an additional source of reactive silanol bonds:

$$\text{≥Si}^{\oplus} + H_2O \longrightarrow \text{≥Si-OH}_2^{\oplus} \longrightarrow \text{≥Si-OH} + H^{\oplus} \qquad \textbf{(5.9)}$$

This proton-initiated mechanism could lead to significant line width spread from a small number of protons, as the catalytic reaction propagates to form many additional cross-links. Recent work shows that HSQ is extremely sensitive to proton beam exposure, but suggests that there are almost no proximity effects when using high energy protons (2 MeV),[39] suggesting that this proton-initiated chain reaction does not occur under those conditions. On the other hand,

preliminary STXM results on e-beam exposed HSQ patterns show that some reaction spread continues for more than a day after e-beam exposure, which would indicate that a very slow chain reaction is in fact occuring.[175] One possible explanation is that the H radical mechanism of the previous paragraph does occur initially, but the silicon radicals left over continue to react much more slowly over time, due to the rigidity of the network HSQ structure. In either case (protons or radicals), interactions at the film surface are expected to inhibit the reaction spread, resulting in narrower lines in thinner films, as observed.

H atoms and protons have similar diffusion coefficients through glasses at room temperature, on the order of ~10^{-7} cm^2/s for protons in porous sol-gel glasses (highly dependent on pore size)[176] and 10^{-6}-10^{-7} cm^2/s for H atoms in amorphous silica,[177] both of which have structures similar to cross-linked HSQ. This can result in one-dimensional diffusion of ~100 nm in just 5 to 16 ms, so the spread of these species from one single-pass line would be complete before an adjacent line is patterned, as each single-pass line in the present study requires >200 ms writing time. If hydrogen radicals or protons are responsible for the spread in the cross-linking, then the incorporation of molecules designed to trap such species should lead to a reduction in the line width spread, and experiments to test this hypothesis are desirable. Preliminary patterning results in films with added inhibitors are discussed in Chapter 6.

Both of these mechanisms can explain the decrease in ≥Si-OH (silanol) content and the increase in oxygen content with cross-linking observed in the NEXAFS spectra in this study [Figure 5.3(a)]. The increase in oxygen may be partially due to creation of new, transient ≥Si-OH groups via reaction with protons and/or moisture, which then react with each other to form cross-links (Eq. 4.14 and 5.6). These new ≥Si-OH groups can also react with existing ≥Si-OH groups, thereby decreasing the total ≥Si-OH content (Eq. 4.17). As the initial ≥Si-OH content is expected to be quite small and would enhance the film sensitivity, the fast initial cross-linking stage also fits with this hypothesis. As noted earlier with respect to the oxygen edge NEXAFS spectra, the amount of adsorbed water may increase during cross-linking due to changes in hydrophobicity and porosity, which would also lead to the observed increase in the total oxygen content of the cross-linked regions. Morphological and hydration changes will also alter the diffusion constant during cross-linking, and indeed a quantitative analysis by us with a simple Fickian diffusion model does not explain the rather abrupt rise and saturation of the linewidth increase versus dose (Figure 5.9(b)) and cross-linking rate (Figure 5.6 (b)). Therefore, to fit all of the experimental data and retrieve diffusion coefficients for the propagating reactive species would require more detailed theoretical modeling, taking into account changes in the diffusion constant over time, the changing rate constant as evidenced by the two-stage, apparently first-order kinetics, and surface effects that explain the thickness dependence.

5.8 Conclusions

Direct-write X-ray lithography and subsequent X-ray imaging of the latent resist patterns is a powerful way to follow the chemistry of X-ray induced processes in the absence of developer effects. Oxygen and silicon edge NEXAFS spectra of the HSQ film before and after X-ray exposure show that the total oxygen content in X-ray exposed regions increases substantially, by ~30% at 808 MGy and less at lower doses, while the ≥Si-OH content decreases, and no change in the silicon content is observed. This indicates that existing ≥Si-OH is consumed by incorporation into the network and that there is an uptake of water and/or

additional incorporated oxygen in the X-ray cross-linked regions. The sensitivity of HSQ to direct X-ray exposure reveals that the cross-linking proceeds by a very fast initial step ($\tau_1 = 0.09 \pm 0.01$ s) followed by a slower second stage ($\tau_2 = 5.5 \pm 0.3$ s), which suggests that there are initially some number of easily cross-linked sites, and that the reaction rate slows considerably after these sites are consumed.

Direct-write X-ray lithography and subsequent X-ray imaging of the latent patterns with 30 nm resolution reveals a dose and thickness dependent reaction front spread in excess of 70 nm in HSQ films independent of developer conditions, which is crucial to understanding the resolution-limiting characteristics of HSQ and correcting for proximity effects. The long range of this dose and thickness dependent reaction spread is likely due to the diffusion of some small ions or radicals through the HSQ film, and we provide two possible mechanisms based on diffusing H atoms or protons. The full extent of this spread is not apparent after high-contrast, room-temperature development, as the developer solution removes material below a critical, relative cross-linking degree of 7.1 ± 2.5% (relative to the maximum number of cross-linkable sites within the film), whether it is cross-linked by direct exposure or reaction spread. While the STXM imaging requires thick HSQ films (>250 nm) for good signal-to-noise ratios, the chemical information and line width versus thickness trends appear to be applicable for thinner films, as well.

Future X-ray work on HSQ can address the role of water and ≥Si-OH in the X-ray induced cross-linking mechanism and test if H radical or proton diffusion is responsible for the reaction spread outside the exposed region. Preliminary results with various reaction-spread inhibitors are discussed in Chapter 6. The next generation of Fresnel zone plates for X-ray microscopy, with 12-15 nm outer diameters,[10-12] will significantly improve the resolution possible with both direct-write X-ray lithography and STXM imaging. As HSQ is the resist used for fabrication of these gold zone plates, higher resolution X-ray microscopes are made possible in part by a better understanding of HSQ chemistry. Furthermore, with a better understanding of the cross-linking mechanism, delay effects and the cause of the reaction spread, new and better photoresists based on HSQ can be designed to fabricate the next generation of smaller, faster, more reliable electronic devices, and other new nanoscale device components.

6 Conclusions

6.1 Preliminary results: Incorporating additives to reduce reaction spread

The line width tests shown in Figure 5.9 were repeated with films containing different additives in an attempt to limit the range of the cross-linking reaction spread by capturing free radicals or protons. The free radical scavengers iodine (I_2), benzophenone (BP), mequinol (4-methoxyphenol or O-methylhydroquinone, MEHQ), and butylated hydroxytoluene (BHT) were tested, as well as "proton sponge" (1,8-bis(dimethylamino)napthalene), shown in Figure 6.1. These additives were chosen for their relatively low volatility, such that they would remain in the film after spin-coating. The effect of the inhibitors on HSQ is unknown, so the initial test concentrations were chosen for an average of at least 1 inhibitor molecule to every 8 HSQ monomer cages. The mol% of additive in the final solution is determined relative to the (approximate) number of moles of HSQ solids in the stock solution (~0.47 M HSQ in MIBK for the FOx-15® solution):

$$\text{mol\%} = (\#\text{ moles additive}) / (\#\text{ moles HSQ solids}) \times 100\% \quad \textbf{(6.1)}$$

To prepare thin films with MEHQ (~24 mol%) and BHT (~13 and 74 mol%), a small amount of the solid additives are directly mixed with 1 mL of the HSQ stock solution (FOx-15®); I_2 and BP (12.5 mol%) and proton sponge (0.2 mol%) are pre-mixed in solution with MIBK (methyl isobutyl ketone), then very small, precisely measured aliquots (59 μL) of these additive solutions are added to the HSQ solution (1 mL) to achieve the desired final additive concentration. Each solution is then spin-cast into a thin film on 100 nm silicon nitride following the same procedure given in section 5.2. (Additional films with 12.5 mol% MEHQ and BHT were also prepared, but not tested within the limited STXM beam time available.) For direct comparison, HSQ films with no additive were prepared from a stock solution diluted to the same degree with plain MIBK, to ensure the same viscosity and spin-coating characteristics.

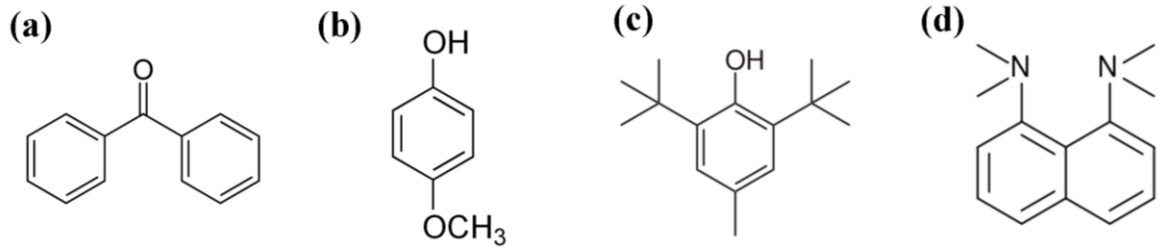

Figure 6.1 Additives tested for limiting reaction spread in HSQ thin films: (a) benzophenone (BP), (b) mequionol (MEHQ), (c) butylated hydroxytoluene (BHT) and (d) proton sponge (1,8-bis(dimethylamino) naphthalene). I_2 was also tested (not shown).

Single-pass lines at various doses were patterned with the 580 eV X-ray beam in the HSQ films with and without additives, as in section 5.6, and subsequently imaged with the 5.3.2 STXM. The line widths versus dose are plotted in Figure 6.2, with estimated film thicknesses listed in parentheses, which shows that the line widths are actually wider in all of the films with inhibitors. Unfortunately the data are mostly inconclusive because differences and uncertainty in

the film thicknesses and delay effects mask potential differences due to the additives. First of all, line widths can only be directly compared between films with the same thickness, but variations in film thickness from region to region make it extremely difficult and prohibitively time consuming to find regions that are comparable from film to film. In the previous chapter, this was solved only by taking many, many measurements on identical films, and only comparing regions with equivalent thickness; each measurement is still quite time consuming, and so far, not enough data have been collected on inhibitor-added films to achieve this. Second, variations in film composition and density due to the additives increase the uncertainty in the thickness measurements, which are based on the OD 1 nm spectrum of HSQ with a fixed density (1.4 g/cm^3) (see Figure 5.2(a)). To circumvent these film thickness issues, it is desirable to have films of uniform thickness and then measure the thickness by an alternative method, such as ellipsometry or AFM. Two alternative methods for producing uniform thickness films were explored and tested, but neither was feasible within the parameters of these studies.

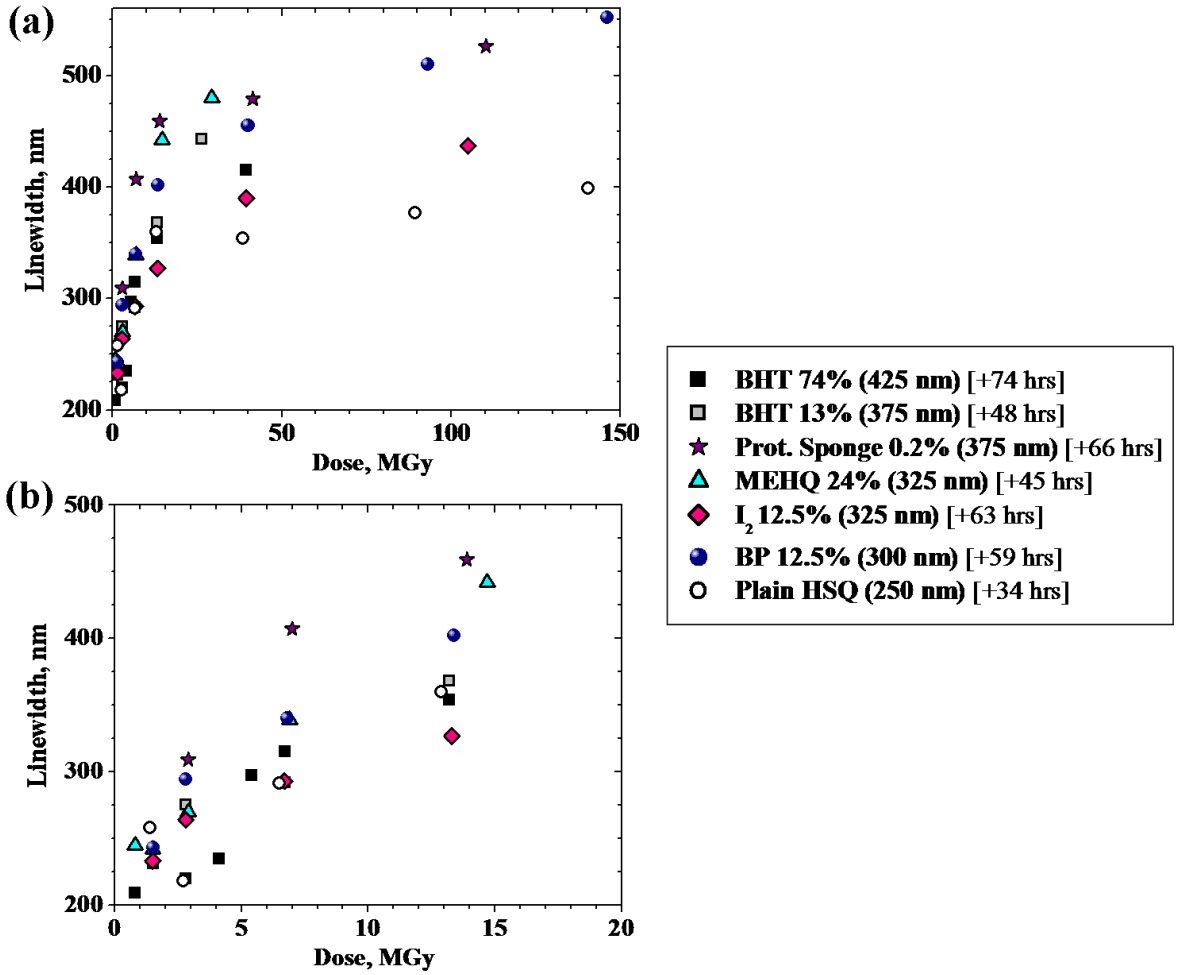

Figure 6.2 Average FWHM line widths for single-pass lines in HSQ films varying from 250 nm to 425 nm thick with various radical and proton scavenger molecules added (a) Full range of doses tested and (b) zoomed in to low dose. Legend at right, with estimated film thicknesses shown in parentheses, and time delay between spin-coating and exposure listed in brackets.

A third complication may be delay effects, as line widths have been shown to increase significantly (greater than 100% in 8 hours) with delay between film pre-bake and exposure, measured after development.[49] Preliminary results with the STXM reveal similar line width broadening when there is a delay between spin-coating and exposure, even in unbaked samples. In the inhibitor-added films, there is a different time delay between film spin-coating and exposure for several of the measurements, due to STXM beam-time constraints, sample loading and positioning times, and trial and error in finding suitable areas of each sample for patterning and measurement. That is, different samples were measured between 34 to 74 hours after spin-coating, with the delay time listed in brackets in the legend on Figure 6.2. The line widths appear to be larger in films subjected to a greater delay between spin-coating and exposure, even though the films were not pre-baked, again indicating that the precise delay between spin-coating and exposure should be more carefully controlled in future STXM work. However, based on the estimated film thicknesses listed, the 12.5 mol% I_2 and 74 mol% BHT may reduce the linewidth compared to the other inhibitor-added films.

Aside from the linewidth measurements, a very interesting reaction occurred between the HSQ (FOx-15®) and the proton sponge in solution. The proton sponge acts as a very strong base and yet a very poor nucleophile, as it is highly favorable to trap just one proton between the amine groups shown in Figure 6.1(d). By adding just 0.2 mol % of proton sponge, the entire 1.06 mL solution proceeds to cross-link and solidify within the vial in just ~15 s, progressing with the evolution of gas bubbles and heat. Slightly higher concentrations of proton sponge (0.04 mol% and above) result in a nearly "instantaneous" reaction of the entire 1 mL HSQ solution, and thus films could not be made with proton sponge concentrations above 0.2 mol%. This reaction can potentially reveal important HSQ chemistry. First, the proton sponge is only expected to interact with the hydrogen atoms, so it shows that the cross-linking can certainly be initiated by the abstraction of H atoms from either the ≡Si-H or ≡SiO-H bonds.[56] Second, the high degree of solidification versus the extremely low concentration of proton sponge indicates that the proton sponge initiates a rapid cross-linking chain reaction throughout the entire solution, and/or that a very low degree of overall cross-linking is sufficient for solidification. The substantial amount of gas evolved indicates that volatile products are formed by the breaking of these HSQ bonds, with the possibilities being H_2, H_2O (following equations 4.14 or 4.16) or possibly SiH_4 (Eq. 4.20). This proton sponge reaction is likely similar to the reaction of HSQ thin films with other bases used for development (KOH, NaOH, etc), which also abstract the H atoms and result in H_2 release.[48] Proton sponge does not react with the methyl isobutyl ketone (MIBK) solvent.

A thin film of the HSQ with proton sponge was prepared by spin-coating an aliquot of the solution within ~5 seconds of mixing, before solidification of the solution occurred. Interestingly, the NEXAFS spectrum of this thin film, shown in Figure 6.3, looks very much non-cross-linked when compared to the "unexposed" HSQ spectra in Figure 5.3, which indicates that the spin-coating stopped the reaction. This is likely due to the severely restricted mobility of reactive species in the thin film, which may prohibit the proton sponge from interacting with the HSQ by locking it into an unfavorable geometry, and/or stop a chain reaction from propagating through the film by restricting the motion of some secondary reactive species. Furthermore, the fact that the proton sponge reacts very rapidly with HSQ in solution, yet reacts very little in the solid thin film may also indicate that the other inhibitors will have limited effectiveness at preventing reaction spread in the solid thin film due to restricted mobility.

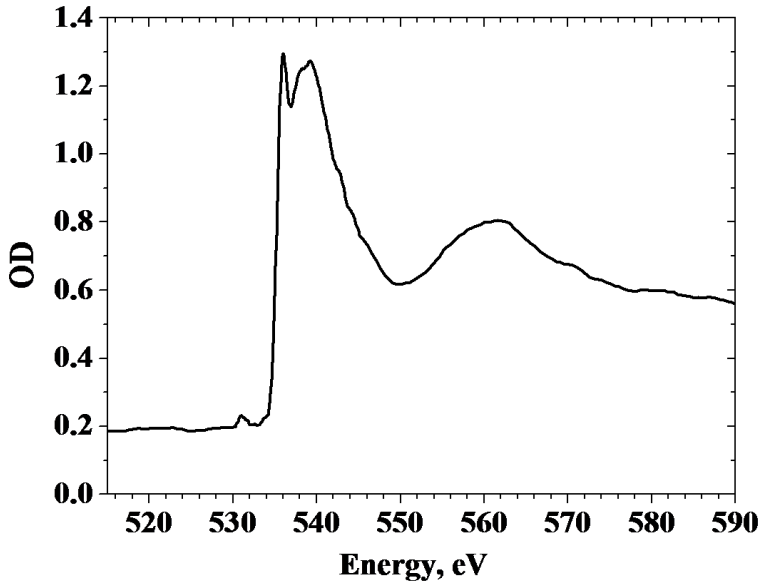

Figure 6.3 Oxygen K-edge NEXAFS spectrum of HSQ thin film containing ~0.2 mol % proton sponge. The entire solution used to prepare this film was completely solidified (cross-linked) in the bottle within ~15 seconds of mixing in the proton sponge, yet this spectrum is comparable to the un-cross-linked HSQ thin film spectra in Figure 5.3.

More research on the reaction rate of proton sponge and other acids and bases with HSQ in solution is desirable to understand what types of bond cleavage lead to the most rapid HSQ cross-linking in solution, which may also provide insight on the types of bond breaking that occur in the solid thin film. Also, to understand how the inhibitors affect the photo-induced cross-linking rate, and what type of bond-breaking limits the reaction rate, it is desirable to monitor the cross-linking in films with inhibitors at various concentrations with both CARS and STXM, both in real time (as in Chapters 3 and 4) and by imaging of varied-dose exposure patterns (as in Figure 5.6). Furthermore, it would be useful to analyze the nitrogen and carbon K-edge NEXAFS spectra and STXM images of all the inhibitor-added films to ensure that the inhibitors are in fact present throughout the film, and not segregated into domains or crystals.

6.2 Summary and outlook: HSQ photolithography

Two direct-write photolithography methods are demonstrated in HSQ thin films and studied in detail for the first time. It is shown that with both near IR, multiphoton-induced cross-linking (NIR MAP) and direct-write X-ray lithography of HSQ thin films, the change in concentration of cage-like species fits to a double exponential decay, suggesting two stages with first order kinetics. This indicates that in both cases the initial reaction rate is limited by the concentration of reactive sites within the film, followed by a slower second stage due to the consumption of the easily cross-linked sites and/or the increasing rigidity of the cross-linked network. This also indicates that the sensitivity of the HSQ film to exposure decreases as the absolute degree of cross-linking increases. As expected, in both X-ray and NIR induced cross-linking, the absorbed dose rate (number of photons absorbed per unit time) is the most important factor in controlling the rate of the cross-linking reaction, and the total number of photons absorbed determines the final degree of cross-linking.

Some parallels can be drawn between the STXM and NIR MAP reaction mechanisms. The oxygen K-edge NEXAFS spectra of the HSQ films show a clear increase in oxygen content within the X-ray cross-linked regions, caused by the absorption of additional water and/or incorporation of additional oxygen atoms into the network structure with cross-linking. The first stage of the multiphoton cross-linking is initiated by 6±1 near IR photons above a particular power threshold of ~45 mW for ~38 fs pulses (before microscope), which equates to 9.4±2.2 eV absorbed per cross-link. While not conclusive, both of these results are consistent with previously proposed (but not confirmed) e-beam or high temperature reaction mechanisms initiated by direct cleavage of two adjacent ≡Si-H bonds, followed by the linking of two intact HSQ monomer cages by an added oxygen (from atmospheric water or O_2, equations 4.14 and 4.15). Several other possible mechanisms are also explored for the first stage of the multiphoton-induced cross-linking, involving bond redistribution, ≡Si-O and ≡SiO-H bond scission, and it is possible that the X-ray and NIR mechanisms are different. The presence and potential role of a small initial concentration of ≡Si-OH on the cross-linking mechanism is also considered for the first time in this work. Longer measurement times in NIR power dependence studies are desired to assess the non-linearity of the second stage of the cross-linking mechanism, and this comparison may also provide insight about the type of bond-breaking that initiates cross-linking in each stage of the reaction

The NIR results suggest a different, possibly photothermal, mechanism for the very slow cross-linking at low laser powers (less than ~45 mW for ~38 fs pulses), a regime not accessible with previous methods used to study multiphoton ablation processes in positive tone resists.[59] Assuming first order kinetics, a 10±3 photon process is indicated below threshold, with energy deposition throughout the reactive site as opposed to direct photolytic bond breaking. However, much longer measurement times are required to accurately assess the reaction order and power dependence of this below-threshold cross-linking mechanism. Other studies of gaseous reaction products (possibly via mass spectrometry) and cross-linking rates in different environments (e.g. under very high vacuum to eliminate O_2 and H_2O) may also be helpful to narrow the possibilities and pinpoint the precise X-ray and NIR induced conversion mechanisms, both above and below the threshold.

After direct-write X-ray lithography of HSQ, the high spatial resolution of the STXM enables imaging of the spatial extent of the reaction with 30 nm resolution. In relatively thick films (300-500 nm), reaction spread in excess of 70 nm on either side of the exposed region (at the FWHM) is observed, which increases with dose and film thickness. The possibilities of hydrogen radical migration or a proton initiated chain reaction causing the spread are explored in detail, considering the observations in this study and several previous works. This spread is not fully evident after development, as the developer washes away material below a relative degree of cross-linking of approximately 7.5±2.5%. It is clear that this reaction spread can cause significant proximity effects, including area dependent exposure sensitivity. The role of reaction spread has been previously speculated in e-beam lithography of thinner HSQ films,[8, 50] but the STXM results shown here reveal the precise dose and thickness dependent extent of the spreading effect in photolithography of these thicker films, prior to development. In future studies, to achieve the minimum possible line widths, it is desirable to more precisely control the film thickness, sample age, and delay between film preparation and exposure .

In this work, attempts to produce thin films of HSQ or MSQ from the pure, powdered solids were not successful, as the solids will not dissolve appreciably in any commonly used solvents (including those used for the commercial FOx HSQ solution), so some synthetic

modification of the starting materials is apparently necessary for thin film preparation. This hypothesis was verified through discussions with several other photoresist experts, who stated that ≥Si-OH must be incorporated into the HSQ (and MSQ) cage structure to improve solubility for spin-on thin film application.[132, 143-144, 178] To fully understand the cross-linking mechanism of HSQ, and how to design similar resist materials, the concentration and role of ≥Si-OH in the cross-linking mechanism should be determined. While NEXAFS and Raman spectra show features that may be attributed to ≥Si-OH, there is a lack of concrete peak assignments specifically for HSQ thin films. To enable more precise NEXAFS peak assignments for HSQ thin films and related materials, more oxygen and silicon NEXAFS spectra of well-characterized, substituted POSS molecules are desired, including samples with varied, known concentrations of ≥Si-OH incorporated. In the Raman spectra, several potential ≥Si-OH bending modes overlap other strong HSQ bands, but if a significant concentration of ≥Si-OH is present, more sensitive Raman and/or FTIR spectroscopy of the ~3600-3900 cm^{-1} region should reveal a peak corresponding to the ≥Si-OH stretching mode. Comparing the ≥Si-OH peak intensity to the ≥Si-H mode at ~2300 cm^{-1} for samples cross-linked by different methods may reveal the relative role of the two types of bonds in the cross-linking reaction. Desired Raman spectra are, for example, required for films cured at various temperatures, regions patterned with X-ray or NIR beam at various doses, films made from fresh versus aged sample solution, and films in which there was a varied delay between spin-coating or baking and exposure. Spectroscopy of the stock solution may be useful, as well, but more likely will be complicated by the presence of the solvents MIBK and toluene.

Another approach to assess the role of ≥Si-OH would be to synthesize the HSQ (and substituted POSS) solutions from scratch, in order to have better control over the chemical content of the starting materials, since the proprietary nature of the FOx® formulation of HSQ prevents full disclosure by the manufacturer of the synthetic process and precise structure of products in solution. Other standard characterization techniques, such as mass spectrometry, NMR, or chromatography, may also be useful in assessing the ≥Si-OH concentration in commercially available or custom made HSQ solutions and thin films. With current knowledge and processing parameters, HSQ is not (yet) an ideal resist for commercial photolithography applications, especially for integrated circuit manufacturing, due to its low sensitivity and delay effects.[2] However, understanding how ≥Si-OH and the overall HSQ cross-linking mechanism affect the resist sensitivity, resolution and delay effects may be useful in designing modified lithographic methods or new silicon-based photoresist materials for high-throughput photolithography.

To date, the only other method demonstrated for following thin film polymerization processes with relevant time resolution (< 1 second) is real-time FTIR spectroscopy (RTIR), and this study expands the possibilities for solid thin films to include real-time monitoring of Raman active modes. Compared to IR microscopy, broadband CARS microscopy also provides the distinct advantage of imaging undeveloped, patterned resist thin films with sub-micron resolution, demonstrated in other polymer films (PMMA and polystyrene, Figure 2.6), but not yet in HSQ. For HSQ, a small degree of chirp on the laser pulse or sufficiently low laser power effectively the halts cross-linking while maintaining a strong CARS signal, which should make it possible to obtain images of patterned resists with little or no sample damage. This is also expected to be true for any photoresist material that requires simultaneous absorption of >3 NIR photons per cross-linking (or bond-breaking) event. This is analogous to STXM imaging, in

which fast scan rates and low photon flux are optimized to allow low-damage imaging even of samples which are readily damaged by X-ray exposure.

High resolution (sub-diffraction limited) multiphoton lithography using pulsed near IR lasers has been applied to a variety of other photoresists, and this study opens the potential for such patterning in HSQ and related POSS materials, as well. Features down to 120 nm wide were patterned in 100 nm thick PMMA films with 170 fs pulses of 870 nm light at ~25 mW average power, tightly focused with 1.3 NA, 100x objective, and it was determined that the PMMA multiphoton bond-breaking and ablation were initiated by the absorption of 7±3 photons.[59] The 6±1 photon non-linearity of the NIR MAP of HSQ observed in the present work under comparable conditions indicates that a similar resolution enhancement may be expected in HSQ, but development and AFM imaging of NIR patterns in HSQ are needed to verify the lithographic resolution. The minimum line widths in HSQ are, of course, further limited by reaction spread based on the HSQ film thickness, dose and delay effects, but the development process can also be optimized to further enhance the feature resolution, as is the case for all HSQ lithography.

In the future, this may enable the design and fabrication of 3D, multilevel microdevices with pulsed NIR light in HSQ, and other silicon-based photoresists, with *in situ* CARS characterization and monitoring. For reported multiphoton lithography of other materials, typical point spacing of 100 nm and per-pixel dwell times from ~10 to 100 ms are utilized, so *in situ* monitoring using CARS microscopy of these other processes may be feasible, as well. With a relatively small addition of equipment to many of these current direct-write photolithography setups, simultaneous patterning and monitoring of the degree of conversion (cross-linking or bond breaking, for example in PMMA) could be achieved. The current sensitivity requires per-pixel dwell times of at least 50 ms to achieve a useful CARS spectrum, but CARS sensitivity improvements currently being developed may lower this dwell time limitation.[115] Even the full CARS setup, including pulse shaper, SLM, microscope, piezo stages and controllers, optics, spectrometer and CCD, will likely cost less than an e-beam exposure apparatus, so it may be preferable when >100 nm resolution features and *in situ* monitoring are desired. In fact, it may be possible to even enhance multiphoton lithography rates in other polymers by using the pulse shaping apparatus to compress the laser pulses, giving higher peak powers. A further advantage of this setup is that the same microscope could be used for patterning and immediate post-pattern imaging prior to development, similar to that demonstrated with the STXM microscope in Chapter 5. In the future, there are other sensitive Raman microscopy techniques that may also be utilized (with modification) for *in situ* monitoring and imaging of thin resist films, possibly circumventing polarization issues encountered here and improving the temporal resolution of the technique, such as FTSI-CARS[131] and broadband stimulated Raman scattering (SRS).[179-180] Even narrowband CARS has been used to assess the degree of cross-linking in polymer photoresist structures after patterning,[75, 142] so it is possible that a configuration for using narrowband CARS or SRS[181-182] for *in situ* monitoring during MAP patterning could also be conceived. With the recent advances of MAP technology to sub-100 nm resolution,[60] the applications of this technique are expected to grow, and *in situ* monitoring may find an important role in characterizing and optimizing the MAP materials and exposure methods. Regardless of the techniques used, advances in HSQ and related photoresist materials are sure to play an important role in the next generation of micro and nanolithography.

Bibliography

[1] Yang, J. K. W.; Cord, B.; Duan, H. G.; Berggren, K. K.; Klingfus, J.; Nam, S. W.; Kim, K. B. and Rooks, M. J. *J. Vac. Sci. Technol., B* **2009**, *27*, 2622.

[2] Grigorescu, A. E. and Hagen, C. W. *Nanotechnology* **2009**, *20*, 292001.

[3] Reiser, A. *Photoreactive Polymers: The Science and Technology of Resists*; John Wiley & Sons: New York, NY, 1989.

[4] Attwood, D. *Soft X-Rays and Extreme Ultraviolet Radiation: Principles and Applications*; Cambridge University Press: New York, NY, 1999.

[5] *The History of the Integrated Circuit*, http://nobelprize.org/educational_games/physics/integrated_circuit/history/ (January 1, 2010), The Official Web Site of the Nobel Foundation.

[6] Attwood, D., *Errata: Soft X-rays and Extreme Ultraviolet Radiation*, http://ast.coe.berkeley.edu//sxreuv/errata.pdf (January 1, 2010).

[7] *International Technology Roadmap for Semiconductors*, http://www.itrs.net/reports.html (January 1, 2010).

[8] Liddle, J. A.; Salmassi, F.; Naulleau, P. P. and Gullikson, E. M. *J. Vac. Sci. Technol., B* **2003**, *21*, 2980.

[9] Word, M. J.; Adesida, I. and Berger, P. R. *J. Vac. Sci. Technol., B* **2003**, *21*, L12.

[10] Attwood, D.; Chao, W. L.; Anderson, E.; Liddle, J. A.; Hartneck, B.; Fischer, P.; Schneider, G.; Le Gros, M. and Larabell, C. *J. Biomed. Nanotechnol.* **2006**, *2*, 75.

[11] Chao, W.; Harteneck, B. D.; Liddle, J. A.; Anderson, E. H. and Attwood, D. T. *Nature* **2005**, *435*, 1210.

[12] Chao, W. L.; Kim, J.; Rekawa, S.; Fischer, P. and Anderson, E. *J. Vac. Sci. Technol., B* **2009**, *27*, 2606.

[13] Gil, D.; Menon, R. J. and Smith, H. I. *J. Vac. Sci. Technol., B* **2003**, *21*, 2956.

[14] Olynick, D. L.; Harteneck, B. D.; Veklerov, E.; Tendulkar, M.; Liddle, J. A.; Kilcoyne, A. L. D. and Tyliszczak, T. *J. Vac. Sci. Technol., B* **2004**, *22*, 3186.

[15] Stade, F.; Heeren, A.; Fleischer, M. and Kern, D. P. *Microelectron. Eng.* **2007**, *84*, 1589.

[16] Weng, Y. J.; Weng, Y. C.; Fang, H. S. and Yang, S. Y. *Jpn. J. Appl. Phys.* **2009**, *48*.

[17] Arpin, K. A.; Mihi, A.; Johnson, H. T.; Baca, A. J.; Rogers, J. A.; Lewis, J. A. and Braun, P. V. *Adv. Mater. (Weinheim, Ger.)* **2010**, *22*, 1084.

[18] Li, L. and Fourkas, J. T. *Materials Today* **2007**, *10*, 30.

[19] Blazej, R. G.; Kumaresan, P. and Mathies, R. A. *Proc. Natl. Acad. Sci. U. S. A.* **2006**, *103*, 7240.

[20] Jensen, E. C.; Bhat, B. P. and Mathies, R. A. *Lab Chip* **2010**, *10*, 685.

[21] Myers, F. B. and Lee, L. P. *Lab Chip* **2008**, *8*, 2015.

[22] Tsougeni, K.; Papageorgiou, D.; Tserepi, A. and Gogolides, E. *Lab Chip* **2010**, *10*, 462.

[23] Greener, J.; Li, W.; Ren, J.; Voicu, D.; Pakharenko, V.; Tang, T. and Kumacheva, E. *Lab Chip* **2010**, *10*, 522.

[24] Jariwala, S.; Tan, B. and Venkatakrishnan, K. *J. Michromech. Microeng.* **2009**, *19*.

[25] Schafer, D.; Gibson, E. A.; Amir, W.; Erikson, R.; Lawrence, J.; Vestad, T.; Squier, J.; Jimenez, R. and Marr, D. W. M. *Opt. Lett.* **2007**, *32*, 2568.

[26] Zhou, H.; Fang, G. J.; Yuan, L. Y.; Wang, C.; Yang, X. X.; Huang, H. H.; Zhou, C. H. and Zhao, X. Z. *Appl. Phys. Lett.* **2009**, *94*.

[27] Gombert, A.; Blasi, B.; Buhler, C.; Nitz, P.; Mick, J.; Hossfeld, W. and Niggemann, M. *Opt. Eng.* **2004**, *43*, 2525.
[28] Chen, C. P.; Tien, T. C.; Ko, B. T.; Chen, Y. D. and Ting, C. *ACS Appl. Mater. Interfaces* **2009**, *1*, 741.
[29] McDonough, L. A. Microscopy and Spectroscopy of Water Uptake in Polymer Photoresists. PhD Thesis, University of Colorado, Boulder, CO, 2004.
[30] Frye, C. L. and Collins, W. T. *J. Am. Chem. Soc.* **1970**, *92*, 5586.
[31] Loboda, M. J. and Toskey, G. A. *Solid State Tech.* **1998**, *41*, 99.
[32] *Spin on Dielectrics*, http://www.dowcorning.com/content/etronics/etronicsspin/etronics_spin_imov.asp (January 31, 2009), Dow Corning.
[33] Chang, T. C.; Chou, M. F.; Mei, Y. J.; Tsang, J. S.; Pan, F. M.; Wu, W. F.; Tsai, M. S.; Chang, C. Y.; Shih, F. Y. and Huang, H. D. *Thin Solid Films* **1998**, *332*, 351.
[34] Liu, P. T.; Chang, T. C.; Tsai, T. M.; Lin, Z. W.; Chen, C. W.; Chen, B. C. and Sze, S. M. *Appl. Phys. Lett.* **2003**, *83*, 4226.
[35] Loboda, M. J.; Grove, C. M. and Schneider, R. F. *J. Electrochem. Soc.* **1998**, *145*, 2861.
[36] Siew, Y. K.; Sarkar, G.; Hu, X.; Hui, J.; See, A. and Chua, C. T. *J. Electrochem. Soc.* **2000**, *147*, 335.
[37] Namatsu, H.; Takahashi, Y.; Yamazaki, K.; Yamaguchi, T.; Nagase, M. and Kurihara, K. *J. Vac. Sci. Technol., B* **1998**, *16*, 69.
[38] Namatsu, H.; Yamaguchi, T.; Nagase, M.; Yamazaki, K. and Kurihara, K. *Microelectron. Eng.* **1998**, *42*, 331.
[39] van Kan, J. A.; Zhang, F.; Zhang, C.; Bettiol, A. A. and Watt, F. *Nucl. Instrum. Methods Phys. Res., Sect. B* **2008**, *266*, 1676.
[40] Sidorkin, V.; van Veldhoven, E.; van der Drift, E.; Alkemade, P.; Salemink, H. and Maas, D. *J. Vac. Sci. Technol., B* **2009**, *27*, L18.
[41] Junarsa, I. P. and Nealey, P. F. *J. Vac. Sci. Technol., B* **2004**, *22*, 2685.
[42] Junarsa, I. P.; Stoykovich, M. P.; Nealey, P. F.; Ma, Y.; Cerrina, F. and Solak, H. H. *J. Vac. Sci. Technol., B* **2005**, *23*, 138.
[43] Peuker, M.; Lim, M. H.; Smith, H. I.; Morton, R.; van Langen-Suurling, A. K.; Romijn, J.; van der Drift, E. and van Delft, F. *Microelectron. Eng.* **2002**, *61-2*, 803.
[44] Guillorn, M.; Chang, J.; Fuller, N.; Patel, J.; Darnon, M.; Pyzyna, A.; Joseph, E.; Engelmann, S.; Ott, J.; Newbury, J.; Klaus, D.; Bucchignano, J.; Joshi, P.; Scerbo, C.; Kratschmer, E.; Graham, W.; To, B.; Parisi, J.; Zhang, Y. and Haensch, W. *J. Vac. Sci. Technol., B* **2009**, *27*, 2588.
[45] Keil, K.; Choi, K. H.; Hohle, C.; Kretz, J.; Szikszai, L. and Bartha, J. W. *J. Vac. Sci. Technol., B* **2009**, *27*, 47.
[46] Grigorescu, A. E.; Van der Krogt, M. C. and Hagen, C. W. *J. Micro/Nanolithogr. MEMS MOEMS* **2007**, *6*.
[47] Haffner, M.; Haug, A.; Heeren, A.; Fleischer, M.; Peisert, H.; Chasse, T. and Kern, D. P. *J. Vac. Sci. Technol., B* **2007**, *25*, 2045.
[48] van Delft, F. C. M. J. M. *J. Vac. Sci. Technol., B* **2002**, *20*, 2932.
[49] Clark, N.; Vanderslice, A.; Grove, R. and Krchnavek, R. R. *J. Vac. Sci. Technol., B* **2006**, *24*, 3073.
[50] Olynick, D. L.; Liddle, J. A.; Tivanski, A. V.; Gilles, M. K.; Tyliszczak, T.; Salmassi, F.; Liang, K. and Leone, S. R. *J. Vac. Sci. Technol., B* **2006**, *24*, 3048.

[51] Grigorescu, A. E.; van der Krogt, M. C.; Hagen, C. W. and Kruit, P. *J. Vac. Sci. Technol., B* **2007**, *25*, 1998.
[52] Grigorescu, A. E.; van der Krogt, M. C.; Hagen, C. W. and Kruit, P. *Microelectron. Eng.* **2007**, *84*, 822.
[53] Ekinci, Y.; Solak, H. H.; Padeste, C.; Gobrecht, J.; Stoykovich, M. P. and Nealey, P. F. *Microelectron. Eng.* **2007**, *84*, 700.
[54] Chang, T. C.; Tsai, T. M.; Liu, P. T.; Mor, Y. S.; Chen, C. W.; Sheu, J. T. and Tsengb, T. Y. *Electrochem. Solid-State Lett.* **2003**, *6*, G69.
[55] Zhu, X. L.; Xie, C. Q.; Zhang, M. H.; Liu, M.; Chen, B. Q. and Pan, F. *Chin. Phys. Lett.* **2009**, *26*, 086803.
[56] Tilley, D. University of California, Berkeley, CA. Personal communication, 2009.
[57] Liu, W. C.; Yang, C. C.; Chen, W. C.; Dai, B. T. and Tsai, M. S. *J. Non-Cryst. Solids* **2002**, *311*, 233.
[58] Yang, C. C. and Chen, W. C. *J. Mater. Chem.* **2002**, *12*, 1138.
[59] Ibrahim, S.; Higgins, D. A. and Ito, T. *Langmuir* **2007**, *23*, 12406.
[60] Li, L.; Gattass, R. R.; Gershgoren, E.; Hwang, H. and Fourkas, J. T. *Science* **2009**, *324*, 910.
[61] Kawata, S.; Sun, H.-B.; Tanaka, T. and Takada, K. *Nature* **2001**, *412*, 697.
[62] Sun, Z. B.; Dong, X. Z.; Chen, W. Q.; Nakanishi, S.; Duan, X. M. and Kawata, S. *Adv. Mater. (Weinheim, Ger.)* **2008**, *20*, 914.
[63] Hanada, Y.; Sugioka, K.; Kawano, H.; Ishikawa, I. S.; Miyawaki, A. and Midorikawa, K. *Biomedical Microdevices* **2008**, *10*, 403.
[64] Kumi, G.; Yanez, C. O.; Belfield, K. D. and Fourkas, J. T. *Lab Chip* **2010**, *10*, 1057.
[65] Baldacchini, T.; LaFratta, C. N.; Farrer, R. A.; Teich, M. C.; Saleh, B. E. A.; Naughton, M. J. and Fourkas, J. T. *J. Appl. Phys.* **2004**, *95*, 6072.
[66] Chen, Y. F.; Yang, H. F. and Cui, Z. *Microelectron. Eng.* **2006**, *83*, 1119.
[67] Choi, S.; Jin, N.; Kumar, V.; Adesida, I. and Shannon, M. *J. Vac. Sci. Technol., B* **2007**, *25*, 2085.
[68] Tivanski, A.; Olynick, D. L.; Gilles, M. K. and Leone, S. R. (in preparation).
[69] Maker, P. D. and Tehrune, R. W. *Phys. Rev.* **1965**, *137*, A801.
[70] Roy, S.; Gord, J. R. and Patnaik, A. K. *Progr. Energy Combust. Sci.* **2010**, *36*, 280.
[71] Evans, C. L.; Potma, E. O.; Puoris'haag, M.; Côté, D.; Lin, C. P. and Xie, X. S. *Proc. Natl. Acad. Sci. U. S. A.* **2005**, *102*, 16807.
[72] Henry, F. P.; Côté, D.; Randolph, M. A.; Rust, E. A. Z.; Redmond, R. W.; Kochevar, I. E.; Lin, C. P. and Winograd, J. M. *Plast. Reconstr. Surg.* **2009**, *123*, 123S.
[73] Duncan, M. D.; Rientjes, J. and Manuccia, T. J. *Opt. Lett.* **1982**, *7*, 350.
[74] Zumbusch, A.; Holtom, G. R. and Xie, X. S. *Phys. Rev. Lett.* **1999**, *82*, 4142.
[75] Potma, E. O.; Xie, S. X.; Muntean, L.; Preusser, J.; Jones, D.; Ye, J.; Leone, S. R.; Hinsberg, W. D. and Schade, W. *J. Phys. Chem. B* **2004**, *108*, 1296.
[76] Decker, C. *Macromol. Rapid Commun.* **2002**, *23*, 1067.
[77] Zhou, H.; Li, Q.; Lee, T. Y.; Guymon, A.; Jönsson, E. S. and Hoyle, C. E. *Macromolecules* **2006**, *39*, 8269.
[78] Laskarakis, A.; Kassavetis, S.; Gravalidis, C. and Logothetidis, S. *Nucl. Instrum. Methods Phys. Res., Sect. B* **2010**, *268*, 460.
[79] Caster, A. G.; Kowarik, S.; Schwartzberg, A. M.; Nicolet, O.; Lim, S. H. and Leone, S. R. *J. Raman Spectrosc.* **2009**, *40*, 770.

[80] Muntean, L.; Planque, R.; Kilcoyne, A. L. D.; Leone, S. R.; Gilles, M. K. and Hinsberg, W. D. *J. Vac. Sci. Technol., B* **2005**, *21*, 1630.
[81] Wang, J.; Stover, H. D. H. and Hitchcock, A. P. *J. Phys. Chem. C* **2009**, *111*, 16330.
[82] Wang, J.; Stover, H. D. H.; Hitchcock, A. P. and Tyliszczak, T. *J. Synchrotron Radiat.* **2007**, *14*, 181.
[83] Gilles, M. K. and Tivanski, A. Lawrence Berkeley National Laboratory, Berkeley, CA. Unpublished work, 2005.
[84] Isoyan, A.; Wuest, A.; Wallace, J.; Jiang, F. and Cerrina, F. *Opt. Express* **2008**, *16*, 9106.
[85] Wachulak, P. W.; Capeluto, M. G.; Menoni, C. S.; Rocca, J. J. and Marconi, M. C. *Opto-Electron. Rev.* **2008**, *16*, 444.
[86] Herzberg, G. *Infrared and Raman Spectra of Polyatomic Molecules*; D. Van Nostrand Company, Inc.: New York, NY, 1945.
[87] Harvey, A. B. *Anal. Chem.* **1978**, *50*, A905.
[88] Lim, S. H.; Caster, A. G. and Leone, S. R. *Phys. Rev. A* **2005**, *72*.
[89] Lim, S. H.; Caster, A. G.; Nicolet, O. and Leone, S. R. *J. Phys. Chem. B* **2006**, *110*, 5196.
[90] Boyd, R. W. *Nonlinear Optics,* Third ed.; Elsevier: London, 2008.
[91] Yueh, F. Y. and Beiting, E. J. *Comput. Phys. Commun.* **1986**, *42*, 65.
[92] Chen, J. X.; Volkmer, A.; Book, L. D. and Xie, X. S. *J. Phys. Chem. B* **2002**, *106*, 8493.
[93] Wurpel, G. W. H.; Schins, J. M. and Muller, M. *Opt. Lett.* **2002**, *27*, 1093.
[94] Rinia, H. A.; Bonn, M. and Muller, M. *J. Phys. Chem. B* **2006**, *110*, 4472.
[95] Pestov, D.; Murawski, R. K.; Ariunbold, G. O.; Wang, X.; Zhi, M. C.; Sokolov, A. V.; Sautenkov, V. A.; Rostovtsev, Y. V.; Dogariu, A.; Huang, Y. and Scully, M. O. *Science* **2007**, *316*, 265.
[96] Knutsen, K. P.; Messer, B. M.; Onorato, R. M. and Saykally, R. J. *J. Phys. Chem. B* **2006**, *110*, 5854.
[97] Andresen, E. R.; Paulsen, H. N.; Birkedal, V.; Thogersen, J. and Keiding, S. R. *J. Opt. Soc. Am. B* **2005**, *22*, 1934.
[98] Pegoraro, A. F.; Ridsdale, A.; Moffatt, D. J.; Jia, Y. W.; Pezacki, J. P. and Stolow, A. *Opt. Express* **2009**, *17*, 2984.
[99] Cheng, J. X.; Volkmer, A.; Book, L. D. and Xie, X. S. *J. Phys. Chem. B* **2002**, *106*, 8493.
[100] Evans, C. L.; Potma, E. O. and Xie, X. S. N. *Opt. Lett.* **2004**, *29*, 2923.
[101] Kee, T. W. and Cicerone, M. T. *Opt. Lett.* **2004**, *29*, 2701.
[102] Okuno, M.; Kano, H.; Leproux, P.; Couderc, V. and Hamaguchi, H. *Opt. Lett.* **2007**, *32*, 3050.
[103] Dudovich, N.; Oron, D. and Silberberg, Y. *Nature* **2002**, *418*, 512.
[104] Oron, D.; Dudovich, N. and Silberberg, Y. *Phys. Rev. Lett.* **2003**, *90*.
[105] Dudovich, N.; Oron, D. and Silberberg, Y. *J. Chem. Phys.* **2003**, *118*, 9208.
[106] Lepetit, L.; Cheriaux, G. and Joffre, M. *J. Opt. Soc. Am. B* **1995**, *12*, 2467.
[107] Caster, A. G.; Lim, S. H.; Nicolet, O. and Leone, S. R. *Spectroscopy* **2006**, *21*, 2.
[108] Lim, S. H. Lawrence Berkeley National Laboratory, Berkeley, CA. Lead researcher for measurement and analysis of data in Figures 2.5 and 2.6, 2005.
[109] Potma, E. O.; Evans, C. L. and Xie, X. S. *Opt. Lett.* **2006**, *31*, 241.
[110] Caster, A. G.; Lim, S. H.; Nicolet, O. and Leone, S. R. *Spectroscopy* **2006**, *21*, 31.
[111] Johnson, W. C.; Wang, J. and Chen, Z. *J. Phys. Chem. B* **2005**, *109*, 6280.

[112] *Wave plate*, http://en.wikipedia.org/wiki/File:Waveplate.png (January 1, 2010), Wikipedia. Figure used under terms of Creative Commons Attribution ShareAlike 3.0 License.
[113] Weiner, A. M. *Rev. Sci. Instrum.* **2000**, *71*, 1929.
[114] Lozovoy, V. V.; Pastkirk, I. and Dantus, M. *Opt. Lett.* **2004**, *29*, 1.
[115] Chen, B. C. and Lim, S. H. *J. Phys. Chem. B* **2008**, *112*, 3653.
[116] Stohr, J. *NEXAFS Spectroscopy,* Ertl, G., Gomer, R., Mills, D. L. *et al.*, Eds.; Springer Ser. Surf. Sci.; Springer-Verlag: Berlin, 1992.
[117] Brandes, J. A.; Lee, C.; Wakeham, S.; Peterson, M.; Jacobsen, C.; Wirick, S. and Cody, G. *Mar. Chem.* **2004**, *92*, 107.
[118] Henke, B. L.; Gullikson, E. M. and Davis, J. C. *At. Data Nucl. Data Tables* **1993**, *55*, 349.
[119] Thompson, A. C.; Kirz, J.; Attwood, D. T.; Gullikson, E. M.; Howells, M. R.; Kortright, J. B.; Liu, Y.; Robinson, A. R.; Underwood, J. H.; Kim, K. J.; Lindau, I.; Pianetta, P.; Winick, H.; Williams, G. P. and Scofield, J. H. *X-ray Data Booklet,* Third ed., Thompson, A. C., Ed.; Lawrence Berkeley National Laboratory: Berkeley, CA, 2009.
[120] Kilcoyne, A. L. D.; Tyliszczak, T.; Steele, W. F.; Fakra, S.; Hitchcock, P.; Franck, K.; Anderson, E.; Harteneck, B.; Rightor, E. G.; Mitchell, G. E.; Hitchcock, A. P.; Yang, L.; Warwick, T. and Ade, H. *J. Synchrotron Radiat.* **2003**, *10*, 125.
[121] Bloomstein, T. M.; Juodawlkis, P. W.; Swint, R. B.; Cann, S. G.; Deneault, S. J.; Efremow, N. N.; Hardy, D. E.; Marchant, M. F.; Napoleone, A.; Oakley, D. C. and Rothschild, M. *J. Vac. Sci. Technol., B* **2005**, *23*, 2617.
[122] Wu, E.-S.; Strickler, J. H.; Harrell, W. R. and Webb, W. W., Cuthbert, J. D., Ed. (SPIE, San Jose, CA, USA, 1992), vol. 1674, pp. 776-782.
[123] Zhou, W.; Kuebler, S. M.; Braun, K. L.; Yu, T.; Cammack, J. K.; Ober, C. K.; Perry, J. W. and Marder, S. R. *Science* **2002**, *296*, 1106.
[124] Cumpston, B. H.; Ananthavel, S. P.; Barlow, S.; Dyer, D. L.; Ehrlich, J. E.; Erskine, L. L.; Heikal, A. A.; Kuebler, S. M.; Lee, I. Y. S.; McCord-Maughon, D.; Qin, J. Q.; Rockel, H.; Rumi, M.; Wu, X. L.; Marder, S. R. and Perry, J. W. *Nature* **1999**, *398*, 51.
[125] LaFratta, C. N.; Baldacchini, T.; Farrer, R. A.; Fourkas, J. T.; Teich, M. C.; Saleh, B. E. A. and Naughton, M. J. *J. Phys. Chem. B* **2004**, *108*, 11256.
[126] Albrecht, M. G. and Blanchette, C. *J. Electrochem. Soc.* **1998**, *145*, 4019.
[127] Bornhauser, P. and Calzaferri, G. *J. Phys. Chem.* **1996**, *100*.
[128] Decker, C. Photo-induced Polymerization - Kinetic Study of Ultrafast Processes Induced by UV Radiation or Lasers. In *Photochemistry and Polymeric Systems*; Kelly, J. M., McArdle, C. B. and Maunder, M. J. d. F., Eds.; The Royal Society of Chemistry: Cambridge, UK, 1993; pp. 32-46.
[129] Belot, V.; Corriu, R.; Leclercq, D.; Mutin, P. H. and Vioux, A. *Chem. Mater.* **1991**, *3*, 127.
[130] Liou, H. C. and Pretzer, J. *Thin Solid Films* **1998**, *335*, 186.
[131] Lim, S. H.; Caster, A. G. and Leone, S. R. *Opt. Lett.* **2007**, *32*, 1332.
[132] Fleischer, M. Molecular Foundry, Lawrence Berkeley National Laboratory, Berkeley, CA. Personal communication, 2009.
[133] Bornhauser, P. and Calzaferri, G. *Spectrochim. Acta, Part A* **1990**, *46A*, 1045.
[134] Ignatyev, I. S.; Partal, F.; Gonzalez, J. J. L. and Sundius, T. *Spectrochim. Acta, Part A* **2004**, *60*, 1169.

[135] Ogasawara, T.; Nara, A.; Okabayashi, E.; Nishio, E. and O'Connor, C. J. *Colloid Polym. Sci.* **2000**, *278*, 1070.
[136] Morrow, B. A. and McFarlan, A. J. *J. Phys. Chem.* **1992**, *96*, 1395.
[137] Burneau, A. and Carteret, C. *Phys. Chem. Chem. Phys.* **2000**, *2*, 3217.
[138] Bertoluzza, A.; Fagnano, C. and Morelli, M. A. *J. Non-Cryst. Solids* **1982**, *78*, 117.
[139] Frost, R.; Cejka, J.; Weier, M. L. and Martens, W. *J. Raman Spectrosc.* **2006**, *37*, 538.
[140] LaFratta, C. N.; Fourkas, J. T.; Baldacchini, T. and Farrer, R. A. *Angew. Chem., Int. Ed.* **2007**, *46*, 6238.
[141] Higgins, D. A.; Everett, T. A.; Xie, A.; Forman, S. M. and Ito, T. *Appl. Phys. Lett.* **2006**, *88*, 184101(1.
[142] Baldacchini, T.; Zimmerley, M.; Kuo, C. H.; Potma, E. O. and Zadoyan, R. *J. Phys. Chem. B* **2009**, *113*, 12663.
[143] Dubois, G. IBM Almaden Research Center, San Jose, CA. Personal communication, 2007.
[144] Olynick, D. Molecular Foundry, Lawrence Berkeley National Laboratory, Berkeley,CA. Personal communication, 2009.
[145] Tyliszczak, T.; Warwick, T.; Kilcoyne, A. L. D.; Fakra, S.; Shuh, D. K.; Yoon, T. H.; Brown, J., G. E.; Andrews, S.; Chembrolu, V.; Strachan, J. and Acremann, Y. *Synchrotron Radiation Instrumentation 2003 AIP Conference Proceedings* **2004**, *705*, 1356.
[146] Heck, J. M.; Attwood, D.; Meyer-Ilse, W. and Anderson, E. H. *J. X-ray Sci. Technol.* **1998**, *8*, 95.
[147] Attwood, D. Lawrence Berkeley National Laboratory, Berkeley, CA. Personal communication, 2010.
[148] Morrison, G. R.; Bridgwater, S.; Browne, M. T.; Burge, R. E.; Cave, R. C.; Charalambous, P. S.; Foster, G. F.; Hare, A. R.; Michette, A. G.; Morris, D.; Taguchi, T. and Duke, P. J. *Rev. Sci. Instrum.* **1989**, *60*, 2464.
[149] Bremmer, J. N.; Liu, Y.; Gruszynski, K. G. and Dali, F. C. *Mater. Res. Soc. Symp. Proc.* **1997**, *476*, 37.
[150] Gullikson, E. M., *X-Ray Interactions With Matter*, http://www.cxro.msd.lbl.gov/ (August 26, 2009).
[151] Yang, J. K. W. and Berggren, K. K. *J. Vac. Sci. Technol., B* **2007**, *25*, 2025.
[152] Tanaka, I.; Kawai, J. and Adachi, H. *Phys. Rev. B* **1995**, *52*, 11733.
[153] Brown Jr, G. E.; Waychunas , G. A.; Stohr, J. and Sette, F. *Journal de Physique* **1986**, *47*, C8 685
[154] Bubeck, R. A.; Dvornic, P. R.; Hu, J.; Hexemer, A.; Li, X.; Keinath, S. E. and Fischer, D. A. *Macromol. Chem. Phys.* **2005**, *206*, 1146.
[155] Coulman, D.; Puschmann, A.; Hofer, U.; Steinruck, H. P.; Wurth, W.; Feulner, P. and Menzel, D. *J. Chem. Phys.* **1990**, *93*, 58.
[156] Pangher, N.; Schmalz, A. and Haase, J. *Chem. Phys. Lett.* **1994**, *221*, 189.
[157] Zhao, J. H.; Malik, I.; Ryan, T.; Ogawa, E. T. and Ho, P. S. *Appl. Phys. Lett.* **1999**, *74*, 944.
[158] Lin, L. W.; Tang, Y. H.; Li, X. X.; Pei, L. Z.; Zhange, Y. and Guo, C. *J. Appl. Phys.* **2007**, *101*, 014314 1.
[159] Malaske, U.; Pfnur, H.; Bassler, M.; Weiss, M. and Umbach, E. *Phys. Rev. B* **1996**, *53*, 13115.

[160] Bayliss, S. C.; Zhang, Q. and Hutt, D. A. *Physics and Statistics of Solids* **1995**, *190*, 85.
[161] Friedman, S. L.; Marcus, M. A.; Adler, D. L.; Xie, Y.-H.; Harris, T. D. and Citrin, P. H. *Mater. Res. Soc. Symp. Proc.* **1993**, *298*, 295.
[162] Bayliss, S. C.; Anstee, P.; Hutt, D. A.; Zhang, Q.; Danson, N.; Bates, J. and Waddilove, A. *J. Appl. Phys.* **1994**, *76*, 5171.
[163] Hessel, C. M.; Henderson, E. J.; Kelly, J. A.; Cavell, R. G.; Sham, T. K. and Veinot, J. G. C. *J. Phys. Chem. C* **2008**, *112*, 14247.
[164] Henschel, W.; Georgiev, Y. M. and Kurz, H. *J. Vac. Sci. Technol., B* **2003**, *21*, 2018.
[165] Sidorkin, V.; Grigorescu, A. E.; Salemink, H. and van der Drift, E. *Microelectron. Eng.* **2009**, *86*, 749.
[166] Nam, S. W.; Rooks, M. J.; Yang, J. K. W.; Berggren, K. K.; Kim, H. M.; Lee, M. H.; Kim, K. B.; Sim, J. H. and Yoon, D. Y. *J. Vac. Sci. Technol., B* **2009**, *27*, 2635.
[167] Lee, C. W.; Ikematsu, Y. and Shindo, D. *J. Electron Microsc.* **2002**, *51*, 143.
[168] Tanuma, S.; Powell, C. J. and Penn, D. R. *Surf. Interface Anal.* **1993**, *21*, 165.
[169] Yamazaki, K. and Namatsu, H. *Jpn. J. Appl. Phys., Part 1* **2004**, *43*, 3767.
[170] Pach, M. and Stosser, R. *J. Phys. Chem. A* **1997**, *101*, 8360.
[171] Sasamori, R.; Okaue, Y.; Isobe, T. and Matsuda, Y. *Science* **1994**, *265*, 1691.
[172] Charlesby, A. and Garratt, P. G. *Proc. R. Soc. London, A* **1963**, *273*, 117.
[173] Olynick, D. L. *et al. submitted* **2010**.
[174] Charlesby, A. *Rep. Prog. Phys.* **1965**, *28*, 463.
[175] Tivanski, A. The University of Iowa, Iowa City, IA. Personal communication, 2010.
[176] Daiko, Y.; Kasuga, T. and Nogami, M. *Microporous Mesoporous Mater.* **2004**, *69*, 149.
[177] Shkrob, I. A. and Trifunac, A. D. *Phys. Rev. B* **1996**, *54*, 15073.
[178] Techneglas, Inc., Perrysburg, OH. Personal communication, 2008.
[179] McCamant, D. W.; Kukura, P.; Yoon, S. and Mathies, R. A. *Rev. Sci. Instrum.* **2004**, *75*, 4971.
[180] Ploetz, E.; Laimgruber, S.; Berner, S.; Zinth, W. and Gilch, P. *Appl. Phys. B: Lasers Opt.* **2007**, *87*, 389.
[181] Freudiger, C. W.; Min, W.; Saar, B. G.; Lu, S.; Holtom, G. R.; He, C. W.; Tsai, J. C.; Kang, J. X. and Xie, X. S. *Science* **2008**, *322*, 1857.
[182] Nandakumar, P.; Kovalev, A. and Volkmer, A. *New Journal of Physics* **2009**, *11*.